

## ABSTRACT

Title of Dissertation: Photochemistry of Exoplanet Atmospheres:  
Modelling alien chemistry accurately and self-consistently

Dillon James Teal  
Doctor of Philosophy, 2023

Dissertation Directed by: Professor Eliza M.-R. Kempton  
Department of Astronomy

Exoplanets offer unique physical and chemical laboratories experiencing entirely alien environments compared to the Solar System planets. Their atmospheres, governed by the same laws of physics, display remarkable diversity and complexity. They serve as the most complex planetary phenomena we can directly observe, coupled to the planet's interior processes, formation environment, the properties of the host star, and complex chemical ecosystems. The art of modelling these systems is a rich field of study, and in this work I study the nature of photochemical models and what understanding they can provide for us based on the quality and breadth of their inputs. By characterizing the implicit uncertainty chemical models have without a well-characterized host star, I quantify the importance of host star characterization to chemical modelling, showing their sensitivity under different reaction schemes and microphysical models. I then apply this to recent observations of known exoplanet host stars LHS 3844 and AU Microscopii. Finally, I cover work to model sub-Neptune atmospheres across a wide parameter space aimed at understanding the influence of a planet's environment and unknowns on haze formation

and observational prevalence in emission and transmission spectroscopy.

Photochemistry of Exoplanet Atmospheres:  
Modelling alien chemistry accurately and self-consistently

by

Dillon James Teal

Dissertation submitted to the Faculty of the Graduate School of the  
University of Maryland, College Park in partial fulfillment  
of the requirements for the degree of  
Doctor of Philosophy  
2023

Advisory Committee:

Professor Eliza M.-R. Kempton, Chair/Advisor

Dr. Giada Arney, Co-Advisor

Professor Thaddeus Komacek

Professor Benedikt Diemer

Professor Kayo Ide

© Copyright by  
Dillon James Teal  
2023

## Preface

Science is not well-practiced in isolation. Collaboration is integral to modern research. Unless otherwise stated, the work performed in this thesis, including all graphics and tables, were generated by the author (D. J. Teal). Here I will outline work done by others that is included as part of this work in some capacity as a centralized acknowledgement:

- The work performed as part of Chapter 2 and Chapter 5 was largely enabled by significant model updates to our photochemistry model made by Sandra Bastelberger, who is also a co-author on most of the papers published as part of my dissertation research. Her assistance and guidance was invaluable, and she was a critical part of all work done with Atmos. Syntheses of Atmos' methodology, Sections 2.2.1, 5.2.2.1, and 5.2.2.2 were written directly in collaboration with her.
- Chapter 3 covers papers primarily authored by Diamond-Lowe et al. [32] and Feinstein et al. [36]. Summaries of their work required to understand the exoplanet modelling performed as a part of those studies were written by the author, and unless otherwise noted only text contributed by the author is included in any capacity in this paper.
- Chapter 4 describes work performed in Bergin et al. [13]. Similar to the previous point, a summary written by the author of work done in that study is included with a specific focus on the atmospheric modelling performed by the author as part of this study. This

work included significant collaboration with Sandra Bastelberger, who updated the `Atmos` model to include 3 haze formation pathways appropriate for the kind of environments we were modelling.

- Chapter 5 is work currently in-prep. Sections 5.2.2.1 and 5.2.2.2 were both originally authored by Sandra Bastelberger, though significant updates to the original text have been made for this dissertation and for the paper draft.

Other instances where text directly appears in a work not primarily authored by the author of the dissertation are noted, such as captions and figures preserved from their original work. While cited as from their respective works, they were authored primarily by the author of this work, and figures were generated primarily by the author of this work, with any adjustments also noted.

## Dedication

Dedicated to my friends, teachers, peers, and anyone who helped inspire me to strive for decent and good things.

## Acknowledgments

I would like to acknowledge the help of my committee, family, and friends in helping me reach this point and guiding me in my research and life to the best of my ability. None of this would have been possible without incredible support that I'm incapable of repaying in half.

I would like to especially thank Erica Hammerstein and Benjamin Hord for proofreading an initial version of this draft, and for being rad friends and officemates without whom I wouldn't have made it very far past admission.

# Table of Contents

<b>Preface</b>	<b>ii</b>
<b>Dedication</b>	<b>iv</b>
<b>Acknowledgements</b>	<b>v</b>
<b>Table of Contents</b>	<b>vi</b>
<b>List of Tables</b>	<b>ix</b>
<b>List of Figures</b>	<b>x</b>
<b>List of Abbreviations</b>	<b>xii</b>
<b>Chapter 1: Introduction</b>	<b>1</b>
1.1 Discovering Exoplanets . . . . .	1
1.2 The Diversity of Exoplanets and Stars . . . . .	2
1.3 The Fundamental Physics of Exoplanet Atmospheres . . . . .	4
1.3.1 The Atmosphere as a Unified System . . . . .	5
1.3.2 Observing Atmospheres and Their Characteristics . . . . .	8
1.3.3 The Atmosphere as a Stratified, Coupled System . . . . .	12
1.3.4 Aerosols . . . . .	15
1.4 This Work . . . . .	21
<b>Chapter 2: Effects of UV uncertainty when modelling exoplanet atmospheres</b>	<b>22</b>
2.1 Introduction . . . . .	22
2.1.1 Photochemical Modeling of Exoplanet Atmospheres . . . . .	22
2.1.2 Considering the Host Star’s UV Spectrum . . . . .	25
2.2 Methods . . . . .	28
2.2.1 Photochemistry and climate model . . . . .	28
2.2.2 UV input spectra for photochemical modeling . . . . .	35
2.2.3 Exo-Transmit transmission spectra . . . . .	40
2.3 Photochemical modeling results . . . . .	41
2.3.1 Modern Earth . . . . .	41
2.3.2 Archean Earth . . . . .	43
2.4 Transmission spectra results . . . . .	45
2.4.1 Modern Earth . . . . .	45

2.4.2	Archean Earth . . . . .	46
2.5	UV Continuum treatment results . . . . .	48
2.5.1	Continuum models . . . . .	48
2.5.2	Using a neighboring stellar type . . . . .	49
2.5.3	Which UV continuum treatment is correct? . . . . .	51
2.6	Conclusions . . . . .	52
<b>Chapter 3: Modeling atmospheres around newly characterized stars — LHS 3844 and AU Microscopii</b>		<b>70</b>
3.1	Characterizing the high-energy spectrum of LHS 3844 . . . . .	71
3.1.1	Panchromatic spectra of LHS 3844: Flaring and Quiescent . . . . .	71
3.1.2	Atmospheric Models . . . . .	73
3.2	Quiescent and Flaring observations of AU Microscopii in the FUV . . . . .	76
3.2.1	The Far-UV spectrum of AU Mic . . . . .	77
3.2.2	Modelling AU Mic b & c . . . . .	78
3.3	Summary . . . . .	82
<b>Chapter 4: The origins of haze via the protoplanetary disk</b>		<b>84</b>
4.1	Volatile carbon content as a pathway to haze formation . . . . .	84
4.1.1	The planetary nebula . . . . .	84
4.1.2	Implementation of Haze Model . . . . .	86
4.2	Modeling the Observable Atmosphere . . . . .	89
4.3	Discussion & Summary . . . . .	93
<b>Chapter 5: Photochemical Haze Production in sub-Neptune Atmospheres</b>		<b>95</b>
5.1	Introduction . . . . .	95
5.1.1	Aerosols and Exoplanet Atmospheres . . . . .	96
5.1.2	Sub-Neptune Atmospheres . . . . .	98
5.2	Methods . . . . .	99
5.2.1	Grid definitions and parameter space . . . . .	99
5.2.2	Photochemical modeling . . . . .	102
5.2.3	Radiative Transfer . . . . .	108
5.2.4	Coupling HELIOS and Atmos . . . . .	109
5.2.5	Transmission Spectra . . . . .	110
5.3	Results . . . . .	111
5.3.1	Thermal structure and compositional variations for species of interest . . . . .	111
5.3.2	Sensitivity of hazes to planetary parameters . . . . .	112
5.3.3	Radical production and haze formation rates . . . . .	115
5.3.4	Trends in transmission and emission spectroscopy . . . . .	116
5.3.5	Numerically unstable regions of parameter space . . . . .	117
5.4	Conclusions . . . . .	117
5.4.1	Future Work . . . . .	118
<b>Chapter 6: Conclusion</b>		<b>130</b>
6.1	Future Work . . . . .	130

6.2	Upcoming studies and missions . . . . .	132
6.3	Summary . . . . .	133
<b>Chapter A: Facilities and Software used in this Thesis</b>		<b>135</b>

## List of Tables

2.1	Boundary conditions for Modern and Archean Earth modelling . . . . .	30
2.2	MUSCLES catalogue . . . . .	36
3.1	LHS 3844 and LHS 3844 b parameters . . . . .	72
3.2	<i>HST</i> Cosmic Origins Spectrograph wavelength coverage . . . . .	72
3.3	Boundary conditions for a hypothetical Earth around LHS 3844 . . . . .	74
3.4	Parameters for AU Mic and AU Mic b & c . . . . .	77
3.5	Model boundary conditions for AU Mic b & c . . . . .	80
4.1	Atmospheric compositions for different soot accretion rates . . . . .	86
4.2	Model boundary conditions for carbon-enriched sub-Neptunes . . . . .	93
5.1	sub-Neptune grid parameter space . . . . .	100
5.2	GJ 176 physical parameters . . . . .	102
5.3	Average millibar haze column densities . . . . .	120

## List of Figures

1.1	NASA Exoplanet Archive Mass-Radius diagram . . . . .	4
1.2	Mass-radius visualization . . . . .	6
1.3	Atmospheric boundaries diagram . . . . .	7
1.4	Radiation diagram . . . . .	9
1.5	Example transmission and emission spectra . . . . .	11
1.6	Aerosol formation diagram . . . . .	18
2.1	Haze optical properties . . . . .	35
2.2	MUSCLES Survey spectra & the Solar Spectrum . . . . .	57
2.3	Line reconstructions compared to MUSCLES survey data . . . . .	58
2.4	GJ 176 spectrum reconstructions with different continua . . . . .	59
2.5	Modern Earthlike atmospheric profiles . . . . .	59
2.6	Archean Earthlike atmospheric profiles . . . . .	60
2.7	Haze particle radius distributions . . . . .	60
2.8	Modern Earth transmission spectra comparison . . . . .	61
2.9	Archean Earth transmission spectrum comparison . . . . .	62
2.10	Modern Earth GJ 176 continuum treatment profiles . . . . .	63
2.11	Archean Earth GJ 176 continuum treatment profiles . . . . .	63
2.12	Modern Earth GJ 176 continuum treatment transmission spectra . . . . .	64
2.13	Archean Earth GJ 176 continuum treatment transmission spectra . . . . .	65
2.14	Archean Earth GJ 176 continuum treatment particle radius distributions . . . . .	66
2.15	Neighboring spectral types Archean Earth profiles . . . . .	67
2.16	Neighboring spectral types Archean Earth transmission spectra . . . . .	68
2.17	Neighboring spectral types Archean Earth particle radius distributions . . . . .	69
3.1	LHS 3844 flaring and quiescent spectra . . . . .	73
3.2	LHS 3844 photochemical models and transmission spectrum . . . . .	76
3.3	AU Mic flaring and quiescent spectra . . . . .	78
3.4	Photochemical models and transmission spectra for AU Mic b & c . . . . .	79
4.1	Example soot-forming exoplanet . . . . .	87
4.2	Transmission spectra assuming different oxygen enhancement factors . . . . .	88
5.1	<i>TESS</i> objects for <i>JWST</i> follow-up characterization . . . . .	101
5.2	GJ 176 Spectrum (no reconstruction) . . . . .	102
5.3	$T_{\text{eq}}$ temperature and chemical profiles . . . . .	113
5.4	$Z$ temperature and chemical profiles . . . . .	114
5.5	Radical column density vs. haze production rate – $T_{\text{eq}}$ . . . . .	121

5.6	Radical column density vs. haze profuction rate – $Z$	122
5.7	Radical production rate vs. haze production rate – C/O ratio	123
5.8	1 mbar column densities, radicals vs. hazes	124
5.9	1 mbar column densities, radicals vs. hazes	125
5.10	Emission spectra – $T_{\text{eq}}$	126
5.11	Emission spectra – $Z$	127
5.12	Transmission spectra – High $Z$	128
5.13	Transmission spectra – Low $Z$	129

## List of Abbreviations

ACWG	Atmospheric Characterization Working Group
AU	Astronomical Unit (other than AU Mic.)
AU Mic.	AU Microscopii
COS	Cosmic Origins Spectrograph
C/O	Carbon to Oxygen ratio
ELT	Extremely Large Telescope
FUV	Far-UltraViolet
GJ	Gliese Jahrei (catalog of stars)
HAZMAT	Habitable Zones and M dwarf Activity across Time
HD	Henry Draper (catalog of stars)
HST	Hubble Space Telescope
JWST	James Webb Space Telescope
LHS	Luyten Half-Second (catalog of stars)
MUSCLES	Measurements of the UltraViolet Characteristics of Low-mass Exoplanetary Systems
NASA	National Aeronautics and Space Administrations
RV	Radial Velocity
TESS	Transiting Exoplanet Survey Satellite
UV	Ultraviolet
VLT	Very Large Telescope

## Chapter 1: Introduction

The concept of a planet is both familiar and alien. The Earth itself—its soil, ocean, rock, and sky—is an integral part of every creature on it. In extreme contrast to our temperate home, the environments of Jupiter, Neptune, and even Earth’s closest relative, Venus, present inhospitable conditions vastly different from Earth’s interconnected physical and biological systems. Within the last 30 years, this already-diverse population of Solar System planets has been put into a galactic context. Thousands of confirmed planets have unveiled populations of planets unlike those found in the Solar System.

Exoplanetary science, the study of planets beyond the reaches of the Solar System, is a relatively new field of study. While alien worlds have captivated public imagination throughout our collective history, it was only in 1992 that Arecibo confirmed the first exoplanet orbiting a distant pulsar [210]. Three years later, the first planet observed orbiting a main sequence star—a star fusing hydrogen in its core, like our Sun—was discovered by [128]. Since then, thousands of exoplanets have been found orbiting nearby and distant stars [25].

### 1.1 Discovering Exoplanets

There are several techniques used in discovering and characterizing exoplanets. By far, the most productive of these has been the transit method. This method relies on a planet pass-

ing between the observer and the host star, blocking some of the light from reaching the telescope. Although this specific orbital configuration requires some amount of luck, the unexpected population of large planets orbiting their host stars coupled with many wide-field surveys and instruments led to the large number of discoveries of exoplanets around other stars. These planets, which transit often—sometimes with periods on the order of tens of hours—have a high probability to transit their host due to favorable geometry for close-in planets. Several incredibly successful programs, such as the *Kepler* and *TESS* missions, have spotted thousands of exoplanets using this method [e.g., 16, 166]. Other methods such as radial velocities (RV), which measure the motion of the host star due to a planet’s gravity, and microlensing, which utilizes the gravitational lensing effect between a host star, a planet, and a background object, have also provided exceptional insight into the population of exoplanets. In this dissertation, I will focus on planets discovered via the transit method, as these are particularly favorable to in-depth characterization. As they transit their host star or are occulted as they pass behind the host star, information about the components of their atmospheres is detectable by observing differences in the amount of light we see at the telescope. This light, representing the combined flux from the planet and star, as well as light passing through tenuous outer regions of the atmosphere, contain information about the composition and structure of the planet’s atmosphere (further discussed in Section 1.3.2).

## 1.2 The Diversity of Exoplanets and Stars

As of publication, over 5,419 exoplanets have been observed and confirmed outside of our solar system ([NASA Exoplanet Archive](#)). These planets comprise a wide range of masses and radii (see Figure 1.1), including those not represented within our solar system. Notably, a distinct

population of highly irradiated, short-period planets, “Hot Jupiters”, are Jupiter-mass planets orbiting their host stars on the order of days and hours. Current observational evidence and formation theory suggest these planets did not form at their current orbits, instead forming distant from their host star—as with Jupiter in the Solar System—and migrating closer to the host star until tidal locking is achieved [42]. The mechanisms behind this process are not well understood, and several competing mechanisms exist that may play varying roles in Hot Jupiter formation and migration at different phases of its evolution [165]. More broadly speaking, however, this realization upended our understanding of dynamical evolution of planetary systems and introduced a new class of planets with no Solar System equivalent.

Planets are diverse in a variety of ways, the most accessible to observational techniques being their orbital properties (e.g., semi-major axis  $a$ , eccentricity  $e$ , and orbital period  $P$ ), mass  $M$  (if radial velocity measurements are available) and radius  $R$  (if the planet transits its host star). Figure 1.1 represents all confirmed exoplanets on scales of mass vs. radius and density vs. radius, contextualized with the Solar System planets.

Although we can apply many attributes of the solar system planets to interpret observations of new planets, for planets with no solar system equivalent we must inevitably return to the fundamentals of atmospheric science and astrophysics to best interpret observations. Using these principles, we can gradually work up to more complex models capable of coupling the myriad processes simultaneously occurring within any planet, which then inform our models’ interpretation of the observational reality.

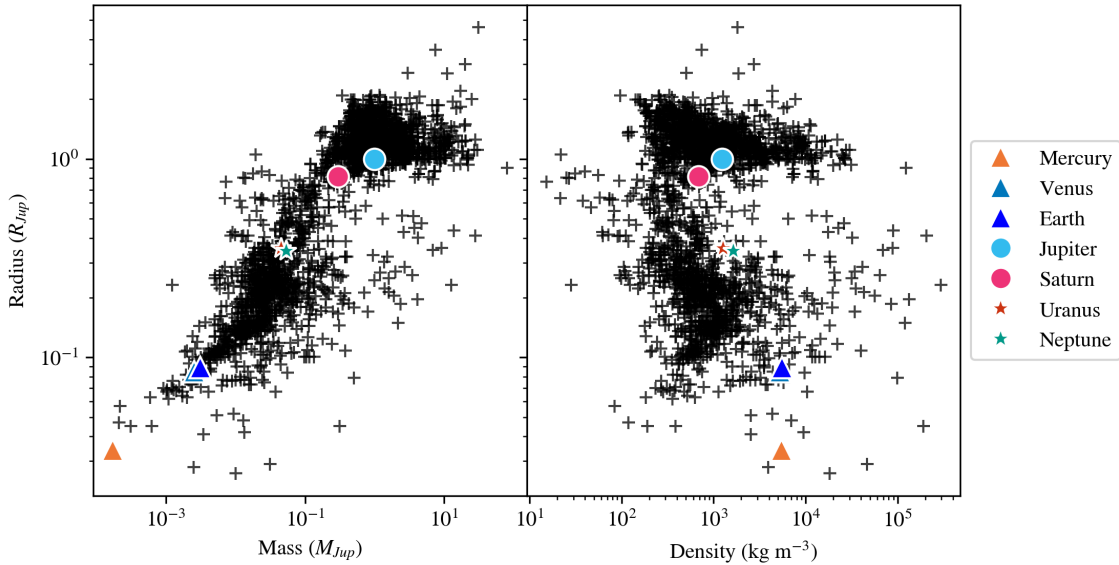


Figure 1.1: Mass-radius diagram for known exoplanets as of 5/28/2023 on the [NASA Exoplanet Archive](#), all plotted as plus (+) symbols. The solar system planets are included for comparison purposes. Although this plot contains a large number of planets, these are heavily biased towards planets most readily observed through transits of their host star (accounting for 93% of the exoplanets plotted), which are, on average, larger, close-in, and hot. Note that visually apparent scatter does not correlate to real scatter, as I do not plot uncertainty of individual measurements to preserve figure readability.

### 1.3 The Fundamental Physics of Exoplanet Atmospheres

Atmospheres comprise a layer of gas surrounding a planetary body of considerable mass. Within the solar system, objects with atmospheres range from highly seasonal, tenuous atmospheres of comets and dwarf planets to the massive and imposing atmospheres of Jupiter and Saturn. Fundamentally, these atmospheres can be sorted into regimes based on their structure and compositions. Figure 1.2 breaks down common (though not exhaustive) definitions of different atmospheric types. This simple definition does not make distinctions between the compositions of atmospheres directly; for example, the atmospheric content (or lack thereof) of the four terrestrial planets of the Solar system have vastly different molecular compositions. Venus' atmosphere

becomes sufficiently dense near the surface that CO<sub>2</sub> is in a supercritical fluid state [108], while Mars's atmosphere is far more tenuous and dry than Venus' or Earth's.

This issue is compounded for exoplanets, as characterizing their atmospheres is difficult and provides far less information than in-situ measurements or imaging of the Solar System planets. Within the scope of exoplanetary systems, atmospheres favorable to spectroscopy and characterization fall into a narrow parameter space limited by the signal-to-noise (SNR) ratio for a given system. Transmission spectroscopy is easiest for nearby, large, hot planets orbiting close to their host star. With modern observatories and techniques, smaller planets have become accessible to characterization and have revealed a large population of planets with masses and radii in between Earth and Neptune. These planets, having no Solar System analogs, fill in the transitions between rocky, terrestrial planets and gas giants, though a sparsely-populated “hot-Neptune desert” also exists in this region [52, 81, 129].

While their bulk compositions differ significantly, the basic physics dictating the properties of an atmosphere apply to all exoplanets. In order to understand and model exoplanet atmospheres, it is important to understand the nature of an atmosphere as a single, unified system of physical processes.

### 1.3.1 The Atmosphere as a Unified System

As a basic model, consider an atmosphere as an semi-infinite slab of gas, with some defined “interior” (a layer in the planet we consider a lower boundary of an atmosphere) and “outer space” above (some altitude where we define the atmosphere as non-existent). Figure 1.3 shows examples of an atmosphere interacting with these two surfaces. Depending on the mass of the

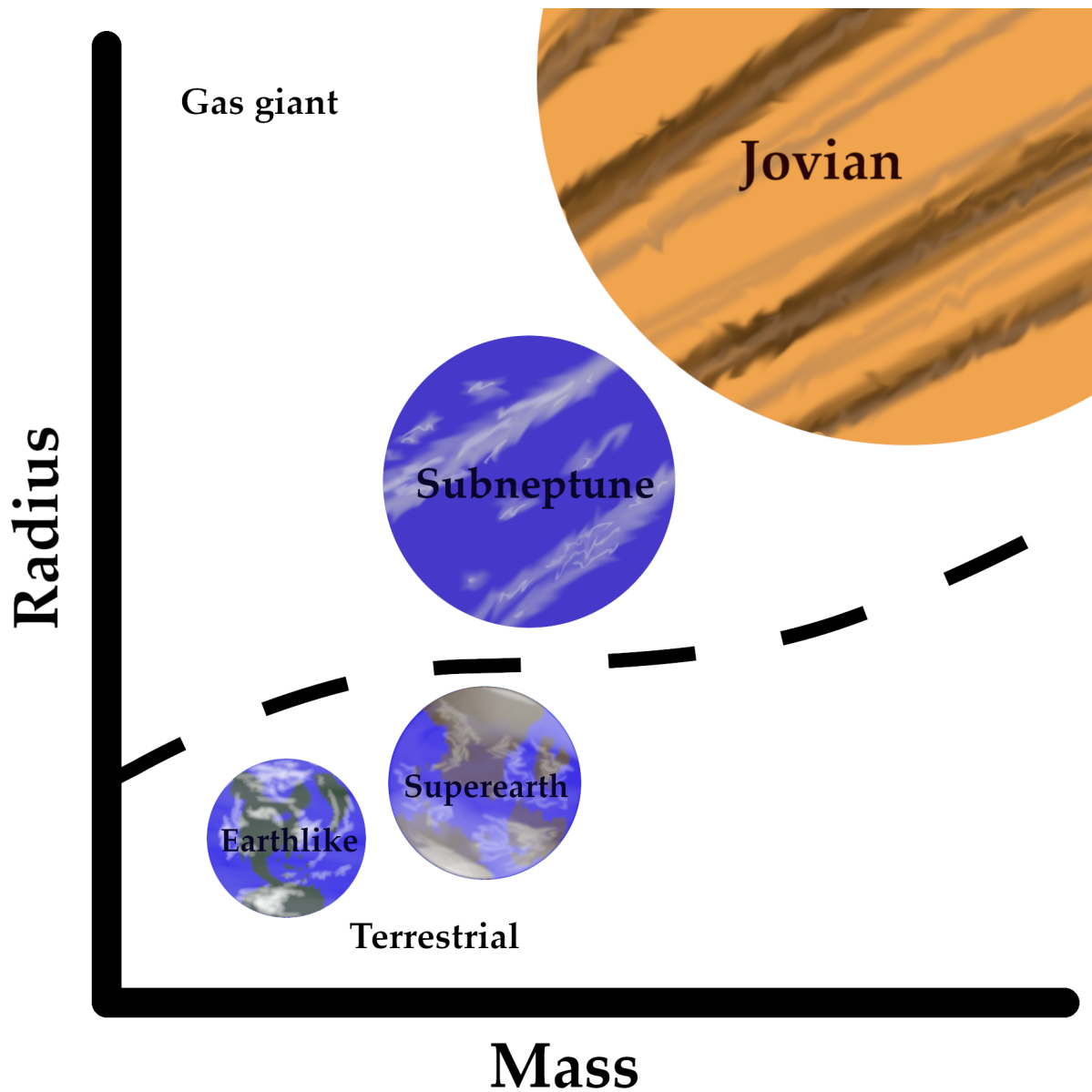


Figure 1.2: Qualitative classification of different planetary types, from largest in mass/radius (top right) to smallest (bottom left). “Terrestrial” planets are those bearing a solid or liquid surface, with a distinct phase transition between gas and fluid/solid at some surface boundary. “Gas Giant” planets have a less well-defined surface, having a large gaseous envelope. “super-Earth” and “sub-Neptune” are common terms used to describe planets with masses and radii larger than Earth’s and smaller than Neptune’s. The primary distinction between the two terms is whether the planet’s atmosphere is large and composed of  $H_2/He$ , or more tenuous and composed of heavier molecules. The current population of planets within this mass/radius regime have significant outliers (see Figure 1.1) that make straightforward, universal classification out of reach.

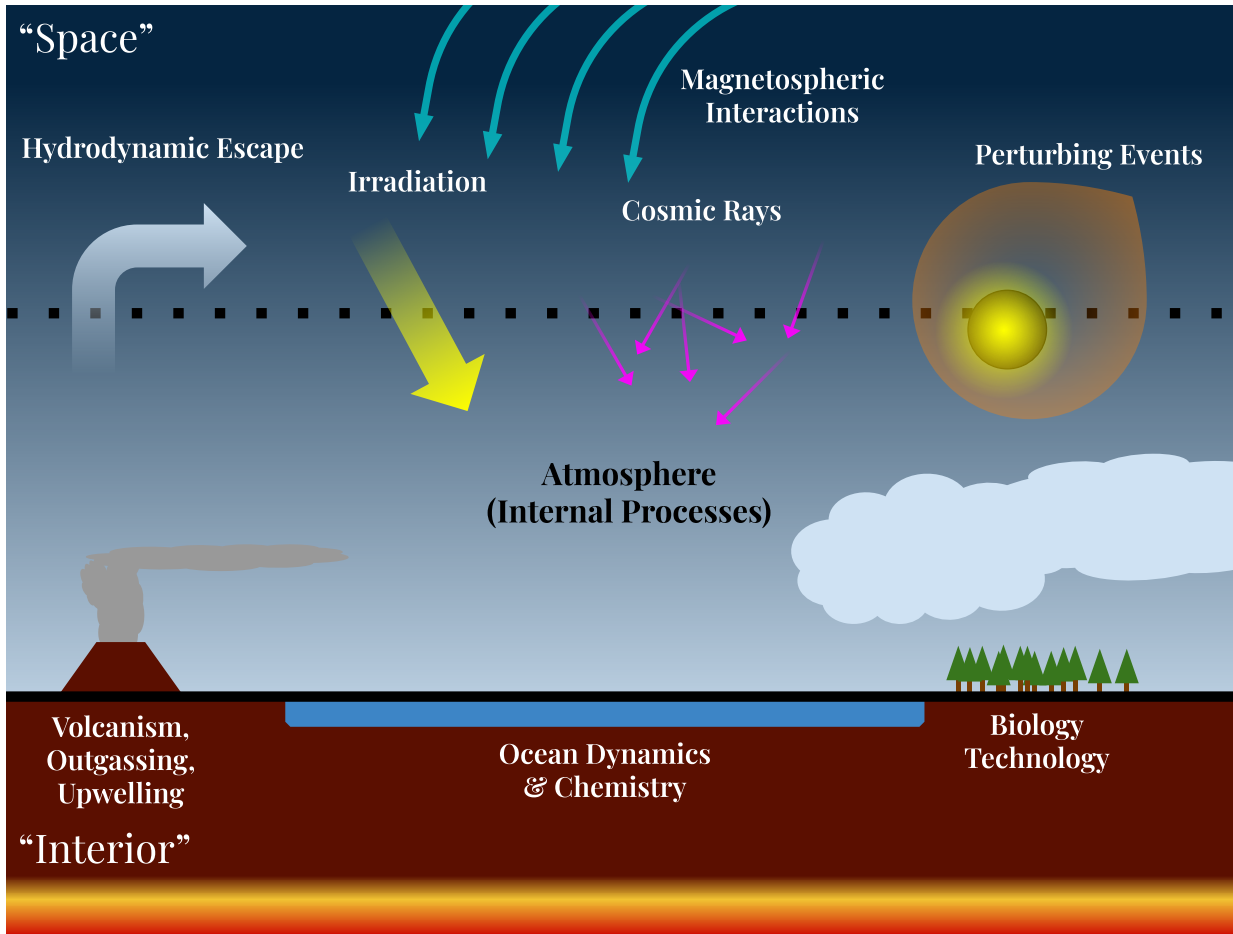


Figure 1.3: A simple model of an atmosphere, with some defined “interior”, such as a solid surface or a specified pressure, and “exterior”, which is typically set to some altitude or low pressure. These external forces on the atmosphere define the long-term composition, structure, and evolution of a planetary atmosphere. While this example contains phenomena specific to terrestrial planets like Earth, we can replace these processes with more appropriate physics for a gaseous/liquid interior and retain the same basic model—a volume of gas being acted upon by external environmental forces.

planet and the nature of its composition, different interactions may occur more, less, or not at all. E.g., “Volcanism” is ill-defined for Jupiter’s atmosphere, since volcanism implies a solid, tectonically-active surface beneath the atmosphere. Some planets do not have magnetic fields, which affect the chemical composition of the upper atmosphere and can produce various aerosols through charged particle rain-out interacting with high-altitude hydrocarbons [60, 159].

These effects, originating from forces beyond the atmosphere, can be modeled as boundary conditions without the need for intensive physical calculations. Ideally, these boundary conditions are informed by laboratory experiments, measurements, and physical models, but often can be reasonably approximated as a constant or simply varying functional form. Throughout this thesis, “external” effects like hydrodynamic escape, outgassing, and most surface interactions are parameterized based on the choice of planet, and unless otherwise specified are typically derived from an equivalent process on a well-studied Solar System planet.

### 1.3.2 Observing Atmospheres and Their Characteristics

Atmospheres are observed by analyzing the interaction of light being emitted from, scattered by, or transmitted through the planet’s tenuous outermost envelope. Figure 1.4 outlines different forms of radiation considered in an exoplanet observation for a transiting exoplanet. The atmosphere of the object itself, in this configuration, is observed by comparing the amount of light detected when the planet is nearby the star, compared to the light observed when the planet is in front of or behind its star. With long enough observing times and modern detectors, there are a number of planets mapped in their reflected/emitted light [e.g., 96].

When light interacts with an atmosphere, a number of processes simultaneously occur that scatter, absorb, and emit radiation that may or may not reach the observer. If we consider a single, linear beam of radiation at wavelength  $\lambda$ ,  $I_\lambda$  which originates at the surface of the host star with intensity  $I_{\lambda,star}$ , and travels through the planets’ atmosphere, then the intensity of the beam at the observer,  $I_{\lambda,obs}$ , is:

$$I_{\lambda,obs} = I_{\lambda,star}e^{-\tau_\lambda} + \int_0^{\tau_\lambda} e^{-(\tau_\lambda - \tau'_\lambda)} S_\lambda(\tau'_\lambda) d\tau'_\lambda \quad (1.1)$$

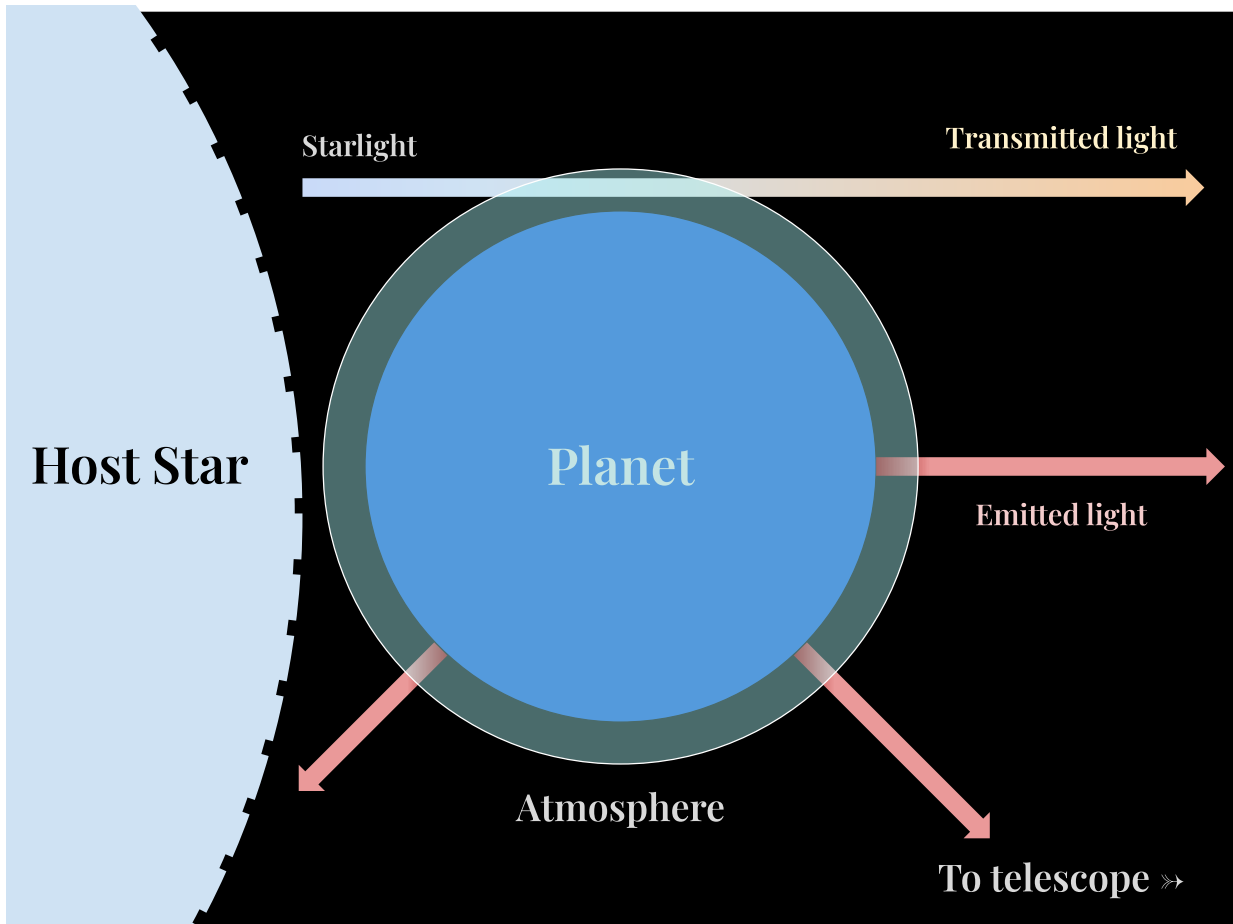


Figure 1.4: Diagram of different types of radiation observed by telescopes. Planets emit primarily in the infrared regime of light, and this radiation interacts with the atmosphere before exiting into space. Transmitted light is starlight which is attenuated by the atmosphere before reaching the observer. These two forms of radiation, along with scattered starlight in the optical, are used to observe and characterize exoplanet atmospheres through transmission and emission spectroscopy.

where  $\tau_\lambda$  is the “optical depth” of the atmosphere, and  $S_\lambda$  is the source function,<sup>1</sup> describing contributions to the beam by emission and scattering.  $\tau_\lambda$  and  $S_\lambda$  each depend on the molecular composition of the atmosphere being passed through, and in general transmitted light only probes pressures of 1 millibar or less. Higher pressures are typically opaque to transmission spectroscopy.

<sup>1</sup>Other texts use “Source Function” to refer to pure emission; here, more simply, it also includes radiation entering the beam through any mechanism (e.g., scattering). For a more thorough treatment of geometry as it is applied throughout this paper, see [92].

Observatories do not capture a single beam of light passing through the atmosphere, however, and the above does not account for pure emission or reflected light. Instead, light at the telescope constitutes the global average of emission, transmission, and reflection across the entire visible disk of the planet. As a planet orbits the host star, the relative fractions of each origin's contribution to the observed light changes,<sup>2</sup> and different information is more accessible at different points in a planet's orbit.

Transiting exoplanets are uniquely favorable to characterization through transmission and emission spectroscopy. These are obtained through observations of the planet when it transits in front of and behind its host star and comparing them to light from the host star alone. The differences between those observations are called the transit depth and the planet/star flux ratio<sup>3</sup> for transmission and emission, respectively. These contain information about the chemical composition of the atmosphere encoded in what specific wavelengths of light are absorbed or emitted most efficiently. By taking observations across many wavelengths, a transit spectrum is produced, with features that can be numerically fit to determine atmospheric composition. The details of this fitting calculation is a rich topic, and outside the scope of this thesis [e.g., 220].

Figure 1.5 shows a pair of example spectra, one transmission and one emission. The emission spectrum isolates the amount of radiation being emitted by the planet alone, while the transmission spectrum represents light passing through the planet's atmosphere at different wavelengths. These probe different regions of a planet's atmosphere; emission spectra include information about the internal temperature of the planet and deeper layers of the atmosphere, while transmission spectroscopy only probes the outermost layers of a planet's atmosphere that

---

<sup>2</sup>Strictly speaking, this is not the case for face-on orbital geometries, in which the plane of the planet's orbit is perpendicular to the observer; for such a configuration, the emitted and reflected light are constant.

<sup>3</sup>Other metrics are regularly used to represent eclipse spectra, such as brightness temperature.

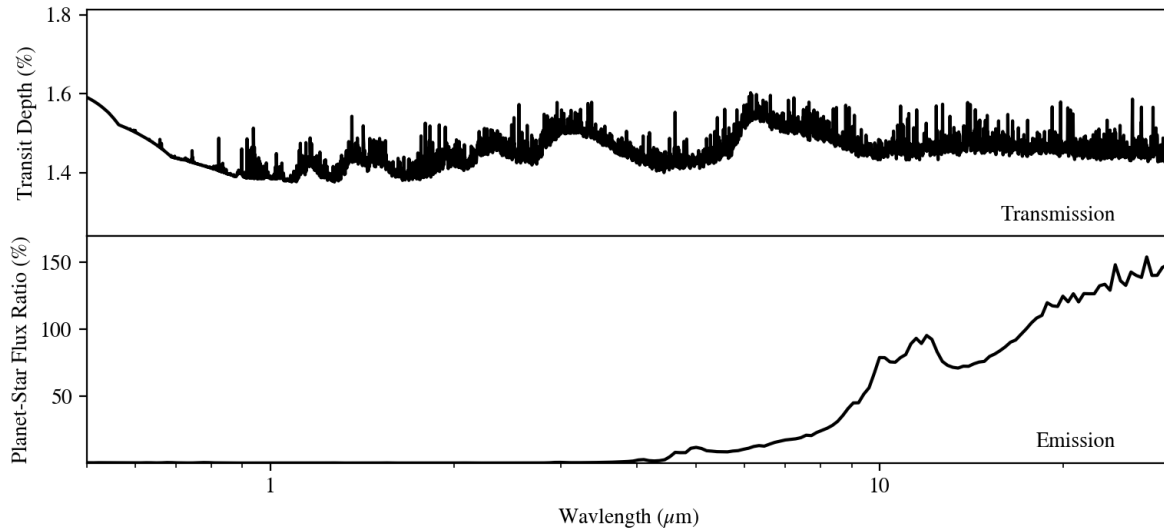


Figure 1.5: Two model spectra for a warm sub-Neptune exoplanet orbiting an M-dwarf star.

**Top panel:** A transmission spectrum as function of transit depth—the amount of light attenuated by the planet passing in front of its star. The larger this value, the more light has been attenuated by the atmosphere due to absorption.

**Bottom panel:** An emission spectrum, shown here as a planet/star flux ratio in ppm. At wavelengths less than  $3 \mu\text{m}$ , little flux is emitted by the planet. At longer wavelengths, the thermal emission of the planet becomes significant, and the emission spectrum is observable.

are tenuous enough to allow the transmission of some light.

While theoretically straightforward, the capability to characterize atmospheres through spectroscopy is a relatively new field. The first detection of a heavy element in an exoplanet’s atmosphere was made by Charbonneau et al. [22], who observed the 583.9 nm sodium doublet in the atmosphere of HD 209458 b. Since that discovery, many more atmospheres have been characterized [e.g., 102, 157, 179, 184], and the recent deployment of *JWST* offers a new, powerful set of instruments to characterize atmospheres during its mission lifetime.

To predict favorable targets for characterization, and interpret the results of observations, computational modelling can probe different physics and chemistry to narrow down the bulk properties of planetary atmospheres. Forward modelling takes known physical parameters such

as orbital distance, coupled with academically inspired guesswork, to predict and interpret observations. However, the simple “slab” model described in Section 1.3.1 is insufficient for more nuanced prediction required for modern observational capabilities.

### 1.3.3 The Atmosphere as a Stratified, Coupled System

External forces such as instellation and quantities like metallicity, mass, and orbital distance will provide insight to the bulk qualities of an atmosphere, but local processes at different altitudes within an atmosphere can drive an atmosphere away from equilibrium and produce potentially observable effects. Modelling these requires slicing our slab model into layers across pressures/altitudes and simulating parcels of interacting and evolving gas. Transport considerations—especially heat redistribution and horizontal transport in the atmosphere—further complicate the problem, as inefficient redistribution and transport can fundamentally change the global composition of a planet’s atmosphere. Different abundances at the approaching and receding terminators can influence the transmission spectrum of a planet, and may require special considerations when using 1-D models as predictors of transmission spectra [203]. Throughout this work, I assume efficient redistribution for all of our models, which is typically considered sufficient for the purposes of many exoplanets and for studies focused on phenomenological trends.

We make other common assumptions throughout our models; first, that the atmosphere is in hydrostatic equilibrium, meaning pressure  $P$  varies with altitude  $z$  as a function of (mass) density  $\rho$ , and gravity  $g$ :

$$dP = -\rho(z)g(z) dz. \tag{1.2}$$

For the purposes of exoplanet atmospheres, we can also assume the atmosphere’s equation of

state follows the Ideal Gas Law

$$P(z) = n(z)k_B T(z) \tag{1.3}$$

where  $n$  is the number density of the atmosphere and  $k_B$  is a physical constant commonly known as the Boltzmann constant. Combining equations 1.3 and 1.2, we can determine the physical structure of an atmosphere as a function of altitude and temperature.<sup>4</sup>

The thermal structure of an atmosphere depends on its composition—the chemical species, clouds, and other refractory compounds in the atmosphere, as well as the radiative environment of the planet imposed by its host star, all contribute to the emergence of a varying thermal and chemical state. For example, the atmospheres of tidally locked Hot Jupiters are believed to experience extreme thermal and chemical variations between the sub-stellar point, which experiences direct irradiation from the host star, and the night side of the planet [e.g., 96]. Different chemical species unable to form on the day side can form on the night side, and vice-versa, with uniformity dictated by the efficiency of transport between the night and day side. To calculate temperatures for a 1-D model, a typical approach is to enforce radiative-convective equilibrium throughout an atmosphere and use this requirement, coupled with solving the radiative transfer equation given some chemical state, to retrieve temperature as a function of pressure, irradiation, and composition.

This thesis uses two different models, CLIMA and HELIOS,<sup>5</sup> to determine the thermal structure of atmospheres given some molecular composition, stellar radiation, and internal temperature. The composition and thermal properties of an atmosphere can vary substantially at

---

<sup>4</sup>Another common assumption is that  $dg(z)/dz = 0$ , or that variations in the gravitational field as a function of altitude are negligible. This is useful in many cases, but we do not assume this in the work described in this dissertation.

<sup>5</sup>CLIMA and HELIOS are described in Sections 2.2.1 and 5.2.3, respectively.

various altitudes, as well as across longitudes and latitudes. This manifests as variations in the clouds and weather on Earth, but details at that scale are unified into a single, globally-averaged detection of the exoplanets’ atmosphere by the telescope.

Molecular composition of the atmosphere requires separate treatment. One approximation is to assume thermochemical equilibrium throughout an atmosphere. This determines the chemical composition of the atmosphere by minimizing the chemical (Gibbs) free energy of the system [e.g., 206]. This treatment is appropriate for hot, dense gases, but breaks down for more tenuous regions of an atmospheres and does not account for disequilibrium processes such as vertical transport and photochemical interactions.

To accurately model the chemistry of an atmosphere, a chemical kinetics treatment is required. This solves a system of differential equations for changes in molecular abundances, summarized as

$$\frac{df_i(z)}{dt} = P_i(z) - L_i(z) + \frac{d\phi(z)}{dt} \quad (1.4)$$

$f_i$  is the fractional abundance of some species  $i$ .  $P_i$  and  $L_i$  are the net production and loss rates of a species due to all sources and sinks, respectively. These include ongoing chemical reactions, photolysis reactions, and at atmospheric boundaries include the “external” sources and sinks described in Section 1.3.1.  $\phi_i$  is a variable capturing vertical transport from adjacent layers in the atmosphere. This is a much more computationally intensive calculation compared to assuming thermochemical equilibrium, but it captures important processes that are of direct concern to modelling observed exoplanets. The details of how we solve this problem in this work specifically is described in Section 2.2.1.

Although this coupled model captures the production and thermal effects of gas-phase con-

stituents, the formation of particulates and clouds in an atmosphere requires further nuance and specific treatments to model. Their formation, from condensation to agglomeration of hydrocarbon monomers, in a complicated microphysical process distinct from typical gas-phase considerations.

### 1.3.4 Aerosols

Although atmospheres are primarily composed of molecules in the gas phase, condensation and solidification of gaseous species into droplets and particulates is ubiquitous throughout the solar system. The nature of these aerosols is as diverse as their compositions, and recent laboratory work has shed invaluable insight onto how these hazes might form in planetary atmospheres, as well as their optical properties. These fundamental components of planetary atmospheres are of increasing importance to study. Previous studies have found signs of high-altitude aerosols in exoplanet atmospheres having first-order impacts on transmission spectroscopy [54, 55, 102]. Aerosols also have implications for atmospheric modelling, as they drastically change the thermal balance at altitudes where they form, and impact surface temperatures significantly [7, 8, 55, also see Sections 2.3.2 and 5.3].

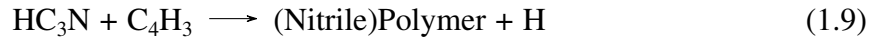
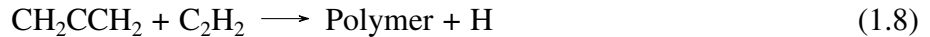
Several generic types of aerosols are defined, though there is some disagreement on how best to apply terminology. In general, clouds are liquid-phase particles that form via the condensation of gas-phase molecules into suspended droplets which, upon reaching a critical mass, are removed from the atmosphere entirely as rain. On Earth, H<sub>2</sub>O is the dominant cloud species, but a variety of species are capable of forming appreciable cloud decks in other planetary atmospheres depending on the atmospheric environment.

For example,  $\text{NH}_3$  clouds are common in the upper atmospheres of Jupiter and Neptune, and  $\text{CH}_4$  clouds have been observed in the atmospheres of Jupiter, Saturn, Titan, and Pluto [62]. At pressures of 1-5 bar, species such as  $\text{H}_2\text{S}$  and condensate compounds like  $[\text{NH}_4]\text{HS}$  are thought to form cloud decks in Jupiter and Saturn, though these are not observationally resolved. In the atmospheres of hot gas giants, highly refractory Na- and Ti-bearing clouds, such as  $\text{TiO}$  and  $\text{Na}_2\text{S}$ , are likely common [54], but our understanding of cloud formation in exoplanet atmospheres is still evolving.

Aerosols can also form via chemical pathways.  $\text{H}_2\text{S}$  and  $\text{CH}_4$  are readily photolyzed by UV irradiation, in turn forming compounds like  $\text{HCN}$ ,  $\text{S}_8$ , and  $\text{C}_2\text{H}_2$ . These then form “hazes”—the common terminology for chemically-produced aerosols—through complex, poorly-understood chemical reaction networks. These processes are thought to produce haze in the atmospheres of Jupiter, Saturn, Titan, and Venus [95, 139, 220]. Figure 1.6 outlines some haze formation processes. Throughout this dissertation, we model a variety of photochemical hazes including pure hydrocarbon, nitrile, and soot-based hazes. Different types of hazes are modelled using similar optical properties, as reliable optical data for nitrile and soot haze species is not available. At small radii ( $< 50$  nm), these particles are modeled using a spherical Mie particle approximation, which assumes that individual particles are well-described by uniformly conducting spheres. These particles grow through agglomeration of individual particles into jagged composite particles containing multiple hydrocarbon monomers, and above 50 nm are more reasonably modelled as fractal particles based on our understanding of hydrocarbon hazes in the atmosphere of Saturn’s moon Titan [17, 163].

All of our hazes are modelled using a “haze precursor” model, in which we assume that one or more governing reactions result in a “haze precursor”, after which its chemical compo-

sition is no longer tracked and it is treated as a single haze particle able to grow and sediment. For example, our pure hydrocarbon hazes form through the polymerization of polyynes, and are governed by one or more of the following reactions, which we describe in more detail when used throughout this work:



Choice in which reactions are used in a given study are specific to the nature of the atmosphere being modelled—for example, we used the “polymer” reactions above in Chapter 4 as these aerosol pathways, while relying on more complex precursor reaction networks, are more appropriate for the carbon-enriched atmospheres we were modelling in that study.

Recent laboratory studies have shown that  $\text{CH}_4$  is not a necessary component in an atmosphere to form hydrocarbon hazes [e.g., 39]. As evidence for the ubiquity of photochemical and thermochemical hazes in a variety of exoplanet atmospheres increases, laboratory efforts have significantly increased the body of knowledge concerning specific optical properties of various hazes produced by observationally-informed gas mixtures [e.g., 39, 58, 59, 80]. However, given the diversity of exoplanet atmospheres and the inherent uncertainty in critical parameters such as

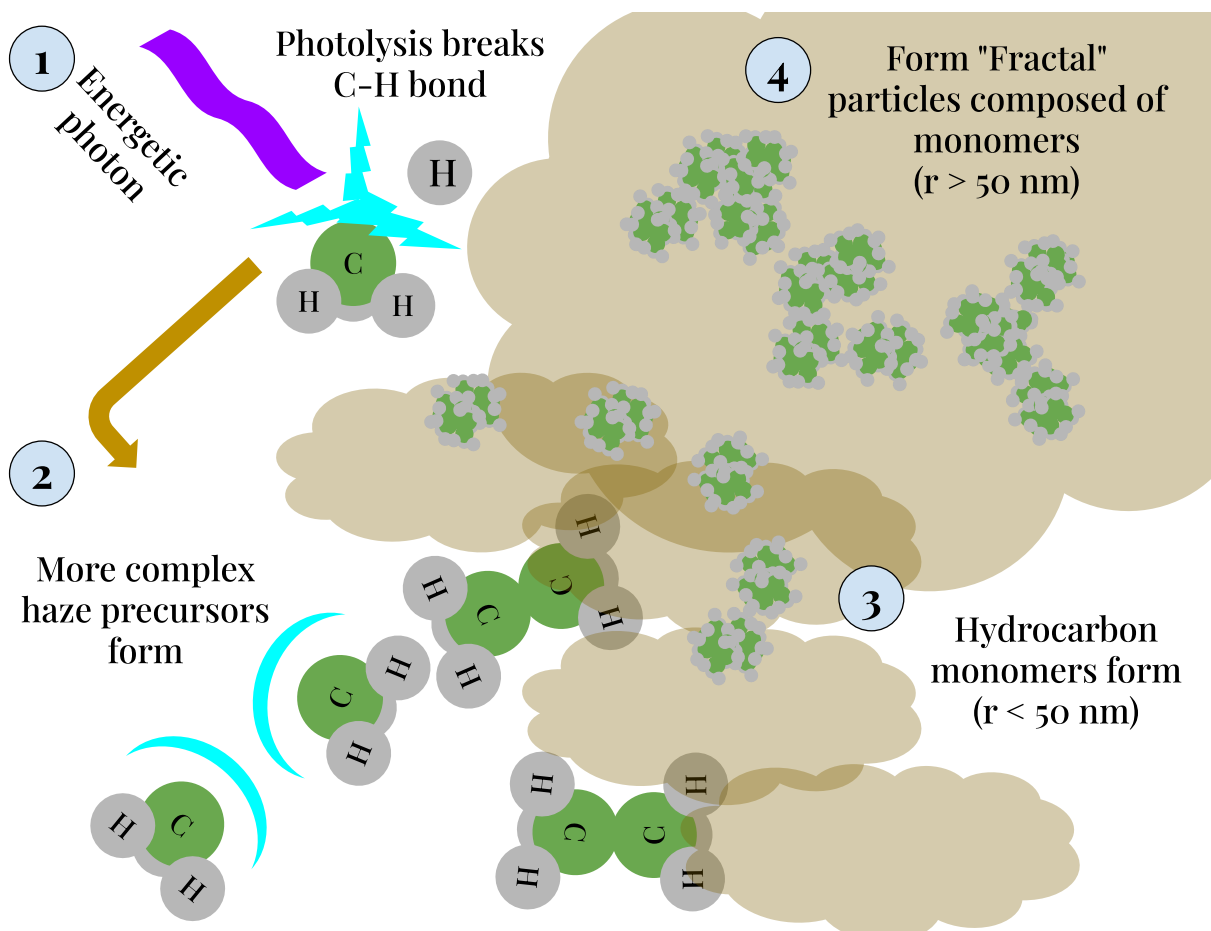


Figure 1.6: Visualization of photolysis leading to more complex hydrocarbon formation. Initially, haze precursors are formed through photons breaking molecular bonds in CH<sub>4</sub>, and then the products go on to form hydrocarbon monomers and finally more complex fractal haze particles.

metallicity and C/O ratio, prescribing any specific formation pathway or haze would be physically unreasonable. We assume 100% efficiency for hazes formed by a haze precursor reaction (e.g., Equation 1.9).

Photochemically produced hazes are especially sensitive to the host star's UV spectrum [186, detailed in Chapter 2]. Characterizing the UV spectrum of a host star is, in turn, a critical component to predicting the nature of aerosols in an exoplanet atmosphere as well as the production efficiency of different haze species. Prior to the work outlined in this dissertation, the importance of host star characterization for chemical modelling was not well-quantified. Chapter

2 details quantifying the effects and understanding the usefulness of proxy spectra—via stellar models or observations of similar stars—in chemical modeling of terrestrial atmospheres with and without hazes.

Once formed, hazes evolve and sediment based on microphysical considerations in our model. An in-depth discussion of this is provided in Sections 5.2.2.1 and 5.2.2.2, though a brief outline of these physics is provided here.

Upon formation, particles immediately attain their terminal fall velocity,  $v_{\text{fall}}$  [158]:

$$v_{\text{fall}} = \frac{2\beta(\rho_p - \rho)gr^2}{9\eta}, \quad (1.11)$$

where  $r$  and  $\rho_p$  are radius and density of the particle, respectively,  $\rho$  is the mass density of the gas,  $g$  is acceleration due to gravity at the altitude the particle is at, and  $\eta$  is the dynamic viscosity of the surrounding gas. The Cunningham slip correction factor  $\beta$  for drag on small particles is calculated using the equation

$$\beta = 1 + \text{Kn} (A + B \exp(-C/\text{Kn})) \quad (1.12)$$

which we take from Pruppacher & Klett [158]. Our model uses values of  $A = 1.257$ ,  $B = 0.4$  and  $C = 1.1$  as suggested by Davies [29]. The Knudsen number,  $\text{Kn}$ , is given by:

$$\text{Kn} = \frac{\lambda}{r}, \quad (1.13)$$

where  $\lambda$  is the mean free path.

$$\lambda = \frac{k_{\text{B}}T}{\sqrt{2}\pi d^2 p} \quad (1.14)$$

$k_{\text{B}}$  is the Boltzmann constant,  $d$  is the diameter of the molecules the gas is composed of,  $p$  is the atmospheric pressure and  $T$  is the temperature. In the continuum regime, when  $\text{Kn} \ll 1$ , the Cunningham slip correction factor  $\approx 1$  and Equation 1.11 reduces to the Stokes settling velocity.

We follow Parmentier et al. [146] and the parameterization from Rosner & [169] in calculating the atmospheric dynamic viscosity  $\eta$  for hydrogen gas is given by

$$\eta = \frac{5}{16} \frac{\sqrt{\pi m k_{\text{B}} T}}{\pi d^2} \frac{(k_{\text{B}} T / \epsilon)^{0.16}}{1.22} \quad (1.15)$$

where  $m$  is the molecular mass,  $d$  is the diameter of the particle, and  $\epsilon$  is the Lennard-Jones potential well equal to  $59.7 k_{\text{B}}$  K.

This model schema, allowing for haze feedback and physical transport, has been updated for the work described in Chapters 4 and 5. Detailed discussion of those updates are left to their respective chapters, though they are broadly meant to modify the nature of these aerosols—which are based on the “tholins” in the atmosphere of Saturn’s moon Titan—to be suited for  $\text{H}_2$  atmospheres, especially considerations of the reaction networks and including appropriate reactions leading from initial photolysis of smaller hydrocarbons like  $\text{CH}_4$  and  $\text{C}_2\text{H}_6$  to the production of haze precursors as shown above in Reactions 1.5-1.10 above.

## 1.4 This Work

In the following chapters, I report work that I have completed in the past 5 years to better understand the requirements for accurately modelling exoplanet atmospheres and applying those models to observations. In Chapter 2, collaborators and I explore how our understanding of an exoplanets' host star impacts our ability to accurately model their atmospheres. In Chapter 3, I break down work I performed as part of observational efforts focused on characterizing the stars LHS 3844 and AU Microscopii, two red dwarf stars known to host exoplanets. In Chapter 5, I discuss generating a grid of sub-Neptune atmospheric models to investigate trends in haze formation and predict observational implications for transmission and emission spectroscopy.

## Chapter 2: Effects of UV uncertainty when modelling exoplanet atmospheres

The work contained in this section is published in *The Astrophysical Journal*, and can be found through the reference Teal et al. [186]<sup>1</sup> The text here is lightly edited for the purposes of this dissertation. I performed the vast majority of work for this published study, including significant updates to the `Atmos` photochemistry model (described in Section 2.2.1) and `Exo-Transmit` (described in Section 2.2.3).

### 2.1 Introduction

#### 2.1.1 Photochemical Modeling of Exoplanet Atmospheres

Observations taken with (*JWST*) will usher in an era of precise characterization of exoplanet atmospheres, including observations of smaller and cooler planets than ever before, and pushing ultimately toward the study of habitable worlds. As more advanced observatories come online, the need for models able to accurately predict observations becomes increasingly crucial. Disequilibrium chemistry in particular has become important as modelling efforts strive for accuracy.

Processes that drive an atmosphere away from chemical equilibrium include photochem-

---

<sup>1</sup>For convenience, it may be accessed at the URL <https://iopscience.iop.org/article/10.3847/1538-4357/ac4d99> or using the DOI [10.3847/1538-4357/ac4d99](https://doi.org/10.3847/1538-4357/ac4d99).

istry and atmospheric mixing (both vertical and horizontal). Such processes should impact planets across a range of parameter space. Less irradiated planets are vulnerable to disequilibrium chemistry because chemical reactions that restore an atmosphere to thermochemical equilibrium are strongly temperature dependent and tend to proceed more slowly at cooler temperatures. As such, the smaller and cooler exoplanets that will be uniquely observable with *JWST* are expected to be significantly impacted by disequilibrium chemical effects, which therefore must be taken into account when modeling their atmospheres. Conversely, hotter planets experience higher UV irradiation, commensurate with their higher instellation, and vertical mixing can be enhanced at higher temperatures [e.g. 147]. For hot Jupiters, the improved wavelength coverage and precision of *JWST* observations will highlight departures from chemical equilibrium that may have been less apparent with prior data sets.

Several processes can drive a planet's atmosphere away from equilibrium. Photochemistry and vertical mixing are examples of two common processes for terrestrial atmospheres. Reactions that restore an atmosphere to thermochemical equilibrium are sensitive to temperature, and are inefficient at low temperatures. As a result, observations of these atmospheres are expected to be significantly impacted by photochemistry and other effects. Conversely, hot planets experiencing strong photolyzing UV irradiation alongside temperature-enhanced vertical mixing [e.g. 147]. For these hot planets, the precision and resolution of *JWST* observations will be sufficient to detect observable consequences of atmospheric disequilibrium.

Chemical kinetics codes have been developed to predict the disequilibrium chemical composition of exoplanetary atmospheres by simultaneously tracking hundreds of chemical reaction rates and vertical mixing [e.g. 82, 88, 97, 111, 133, 141, 167, 191, 198]. The aforementioned codes use a numerical differential equation solver to enforce mass continuity throughout a one-

dimensional (1-D) atmosphere, given production and loss rates within each vertically stratified layer and flux terms acting at layer boundaries. Production and loss terms arise via the chemical reactions, and fluxes arise by processes such as eddy diffusion and molecular diffusion. After setting physically appropriate boundary conditions at the top and bottom of the atmosphere, a steady-state solution is found by time stepping the solver forward until the chemical composition of each atmospheric layer remains stable at a predetermined threshold.

Such chemical kinetics calculations have been applied to the study of exoplanet atmospheres to investigate the photochemical effects on atmospheric composition and aerosol production on a wide variety of exoplanet types, including hot Jupiters [e.g. 111, 140, 141, 198, 216], hydrogen-rich Neptunes and sub-Neptunes [112, 133, 142, 199], and terrestrial exoplanets orbiting a range of host stars [e.g. 170, 176, 212]. When taken together, these studies have confirmed the suspicion that cooler planets should generally be more strongly impacted by disequilibrium chemistry and that such effects should be more readily observable with *JWST*-quality spectra.

An important caveat is that photochemical hazes further complicate modeling predictions and observables. These optically thick particles, hydrocarbon and sulfurous hazes, are expected to become abundant below  $\sim 850$  K in planetary atmospheres with conditions conducive to forming haze precursor molecules [43, 56, 139]. Such hazes bring about significant departures from equilibrium chemistry solutions and are expected to have strong observable signatures [e.g. 8, 88, 90, 139].

## 2.1.2 Considering the Host Star's UV Spectrum

The UV spectrum of a planet's host star is a critical input to chemical kinetics models. It is the UV flux that establishes the rates of photolysis reactions and thereby governs a primary process that drives the atmosphere out of equilibrium at its upper boundary. Unfortunately, the UV spectra of many exoplanet host stars have not been measured, which makes it difficult to accurately model the photochemistry occurring in their planets' atmospheres. Currently, the *Hubble Space Telescope (HST)* is the only astronomical observatory capable of obtaining high resolution UV spectra of host stars between 1,000 and 3,000 Å. With *HST* nearing the end of its lifetime and no comparable UV missions on the near-term horizon, there is a pressing need to identify which UV observations of exoplanet host stars must be obtained now to ensure future success in modeling and interpreting exoplanet spectra obtained with upcoming facilities like *JWST*.

With that in mind, considerable *HST* observing time in recent years has been applied to UV monitoring of stars that are of particular interest to exoplanet studies. Notably, the MUSCLES<sup>2</sup> Treasury Survey (*HST* GO 13650, PI K. France) obtained UV observations with *HST* of 12 M and K stars known to host exoplanets and used these to create high-resolution flux-calibrated panchromatic spectra [46, 113, 214]. Later-type main sequence exoplanet hosts were targeted because UV observations of such stars were generally lacking, despite the fact that M stars offer the most favorable conditions for transit spectroscopy. Furthermore, the planets orbiting M stars are expected to be more highly impacted by the UV environment of their hosts which evolve over the course of a host star's lifetime [116, 178]. Since later type stars give off more UV

---

<sup>2</sup><https://archive.stsci.edu/prepds/muscles/>

radiation relative to their bolometric luminosities compared to earlier-type stars, this effect is particularly relevant to the most favorable targets for characterization of potentially habitable exoplanets. Following on the MUSCLES survey, the Mega-MUSCLES survey [*HST* GO 15071, PI C. Froning; 51] expanded the sample of UV-characterized host stars to additional and even later-type stars, and various other UV studies of exoplanet hosts and the M-dwarf population are being pursued as well [e.g. 14, 15, 18, 33, 47, 50, 115, 154, 202].

With that in mind, considerable *HST* observing time in recent years has been dedicated to UV monitoring of stars that are of particular interest to exoplanet studies. Notably, the MUSCLES<sup>3</sup> Treasury Survey (*HST* GO 13650, PI K. France) obtained UV observations with *HST* of 12 M and K stars known to host exoplanets and used these to create high-resolution flux-calibrated panchromatic spectra [46, 113, 214]. Other surveys—such as Mega-MUSCLES and Mega-MEATS[51, 207]—have expanded the present catalogue of M-dwarf spectra. Later-type main sequence exoplanet hosts were targeted because UV observations of such stars are generally lacking, despite the fact that M stars offer the most favorable conditions for transit spectroscopy.

Planets orbiting M stars are expected to be sensitive to their UV environment, which evolve over the course of a host star’s lifetime [116, 178]. Since later type stars give off more UV radiation relative to their bolometric luminosities compared to earlier-type stars, this effect is particularly relevant to the most favorable targets for characterization of exoplanets within the conservative habitable zone. Following on the MUSCLES survey, the Mega-MUSCLES survey [*HST* GO 15071, PI C. Froning; 51] expanded the sample of UV-characterized host stars to additional and even later-type stars, and various other UV studies of exoplanet hosts and the M-dwarf population are being pursued as well [e.g. 14, 15, 18, 33, 47, 50, 115, 154, 202].

---

<sup>3</sup><https://archive.stsci.edu/prepds/muscles/>

In the absence of observed UV data, various scaling relations have been defined to approximate a host star’s UV spectrum based on optical proxies related to the Ca II H & K lines. Youngblood et al. [215] determined a scaling relation between the equivalent width of the Ca II K line and various UV emission lines using the UV spectra from the MUSCLES survey. Melbourne et al. [132] extended this work to also consider the full set of available *HST* UV spectra of M dwarfs (a factor of  $\sim 7$  increase in sample size) and found that the  $R'_{HK}$  index — the Ca II H & K line core intensity index defined in Rutten [171] — was the best predictor of UV emission line strength of the observable proxies that they considered. The advantage of using optical proxies is that, in principle, a star’s UV spectrum can be approximated in the absence of observed UV data using information readily accessible to ground-based observatories. The Ca II H & K lines, at 3969 Å and 3934 Å, respectively, are historically well-observed, and the  $R'_{HK}$  index has been cataloged for many stars or can otherwise be calculated from existing optical spectra.

For models requiring UV spectra as inputs, such as photochemical models, determining if these reconstructions are sufficient in the absence of observations allows informed decision-making when choosing stars to observe before *HST* is unavailable. This work aims to close the loop on that question with respect to photochemical modeling in particular. We do this by directly comparing the outputs of photochemical models run using observed stellar spectra vs. those run using the Melbourne et al. [132] reconstructions of the same UV spectra. We then examine the degree to which the transmission spectra of each of the modeled exoplanets are altered by the use of the UV reconstructions, and we comment on implications for interpreting observations from *JWST*. In Section 2.2, we describe our photochemistry-climate model, the UV observations that we use as inputs to this model, and how we reconstruct the UV spectra of our input stars. In Section 2.3 we describe the results of our photochemical models, with discussion

of their resulting transmission spectra in Section 2.4. Section 2.5 explores the impact of various reconstructions of the UV continuum (rather than the UV emission lines), focusing on the host star GJ 176. Finally, Section 2.6 summarizes this work and offers discussion of the implications of our results, as well as motivation for future study.

## 2.2 Methods

### 2.2.1 Photochemistry and climate model

We use the `Atmos` coupled 1-D photochemistry and climate model to simulate the physical properties of all atmospheres in our study. This model is well-established in the literature, having been used to investigate the effects of stellar activity on Earth-like atmospheres [e.g. 175, 176], hazy terrestrial (“Archean”) atmospheres [e.g. 7, 8, 35], and numerous other studies of Earth-like atmospheres under various conditions [e.g. 1, 68, 87, 98, 131].

`Atmos` includes the option to iterate between a photochemical model and a 1-D climate (radiative-convective equilibrium) model until reaching a steady-state solution. `Atmos`’ photochemical model includes a variety of important physical processes—such as lightning [68], haze formation [7], sedimentation and rainout [8]—in addition to standard gas-phase chemical and photolysis reactions. This extensively developed and recently updated chemical kinetics model works in conjunction with the included climate model, which determines the 1-D temperature-pressure profile in radiative-convective equilibrium, to explicitly model temperature-sensitive processes such as water saturation and humidity [86, 99, 134]. These coupled models allow for feedback between radiative-convective equilibrium and chemical steady-state self-consistently.

`Atmos` provides two well-tested atmospheric templates that we use in this study: an

oxygen-rich, hazeless<sup>4</sup> modern Earth-like template and a hazy Archean Earth template suitable for low oxygen conditions. These serve as the initial conditions for each of our simulations. Table 2.1 shows the boundary conditions for each chemistry model, which include species specific to either atmospheric state. For our modern Earth and Archean models, we use updated and extended versions of the reaction networks described in Afrin Badhan et al. [1], Lincowski et al. [110] and Arney et al. [8], with the most up-to-date version of these reaction networks appearing in the `Atmos` GitHub repository<sup>5</sup>.

The latest public version of the `Atmos` model includes several significant updates from previously published versions. The changes relevant to this study are summarized below:

- For the climate model, the  $k$ -coefficients for H<sub>2</sub>O and CO<sub>2</sub> were updated using the HITRAN2016 database [63]. For H<sub>2</sub>O, we assume 25 cm<sup>-1</sup> line cut-offs using Lorentz profiles with the plinth removed. For CO<sub>2</sub>, we use 500 cm<sup>-1</sup> line cut-offs using the Perrin and Hartman sub-Lorentzian line profiles ([153]; standard values for coarse spectral resolution). The coefficients were generated using `HELIOS-k` [65].
- The photochemical model uses a 750 bin wavelength grid — the same one from Lincowski et al. [110] spanning 1176.5 – 10000 Å with a resolution of 100 cm<sup>-1</sup>. This grid resolves the UV-wavelength range critical to this study significantly better than the previous 118-bin grid. In particular, important UV lines such as Lyman- $\alpha$  are no longer spread over a broad wavelength range. Instead, these lines are better-resolved, resulting in more accurate calculations of photolysis rates for all molecules. When spread over a wider wavelength range as in the previous wavelength grid, molecules that are otherwise not sensitive to

---

<sup>4</sup>Technically, sulfur aerosols are included in the modern Earth template, but their abundances are trace, and they do not significantly alter the atmospheric state.

<sup>5</sup><https://github.com/VirtualPlanetaryLaboratory/atmos>

Species	Type	Value	Species	Type	Value
<b>Both models</b>			<b>Modern Earth</b>		
O	Deposition velocity	1.0	O <sub>2</sub>	Fixed Mixing Ratio	$2.1 \times 10^{-1}$
H	Deposition velocity	1.0	H <sub>2</sub>	Fixed Mixing Ratio	$5.3 \times 10^{-7}$
OH	Deposition velocity	1.0	CO	Flux	$3.7 \times 10^{11}$
HO <sub>2</sub>	Deposition velocity	1.0	CH <sub>4</sub>	Flux	$1.0 \times 10^{11}$
H <sub>2</sub> O <sub>2</sub>	Deposition velocity	$2.0 \times 10^{-2}$	N <sub>2</sub> O	Flux	$1.53 \times 10^9$
HCO	Deposition velocity	1.0	H <sub>2</sub> S	Flux	$1.0 \times 10^8$
H <sub>2</sub> CO	Deposition velocity	$2.0 \times 10^{-1}$	HO <sub>2</sub> NO <sub>2</sub>	Deposition Velocity	0.2
NO	Deposition velocity	$3.0 \times 10^{-4}$	<b>Archean Earth</b>		
NO <sub>2</sub>	Deposition velocity	$3.0 \times 10^{-3}$	H <sub>2</sub>	Deposition Velocity	$2.4 \times 10^{-4}$
HNO	Deposition velocity	1.0		Flux	$1.0 \times 10^{10}$
H <sub>2</sub> S <sup>(a)</sup>	Deposition velocity	$2.0 \times 10^{-2}$	O <sub>2</sub>	Deposition Velocity	$1.0 \times 10^{-4}$
SO <sub>2</sub>	Deposition velocity	2.0	CO	Deposition Velocity	$1.2 \times 10^{-4}$
	Flux	$1.0 \times 10^9$	H <sub>2</sub> S	Flux	$3.5 \times 10^8$
H <sub>2</sub> SO <sub>4</sub>	Deposition velocity	1.0	CH <sub>4</sub>	Fixed Mixing Ratio	$3.5 \times 10^{-3}$
HSO	Deposition velocity	1.0	C <sub>4</sub> H <sub>2</sub> (Aerosol)	Deposition Velocity	$1.0 \times 10^{-2}$
SO <sub>4</sub> (Aerosol)	Deposition velocity	$1.0 \times 10^{-2}$	C <sub>5</sub> H <sub>4</sub> (Aerosol)	Deposition Velocity	$1.0 \times 10^{-2}$
S <sub>8</sub> (Aerosol)	Deposition velocity	$1.0 \times 10^{-2}$	CO <sub>2</sub>	Fixed Mixing Ratio	$2.0 \times 10^{-2}$
O <sub>3</sub>	Deposition velocity	$7.0 \times 10^{-2}$			
CH <sub>3</sub>	Deposition velocity	1.0			
HNO <sub>3</sub>	Deposition velocity	$2.0 \times 10^{-1}$			

Table 2.1: Static boundary conditions at the surface of our model. Deposition velocity has units of cm/s. Flux is a constant surface flux of a species measured in molecules/cm<sup>2</sup>/s. We note that this does not include top-of-atmosphere fluxes, such as downward fluxes of CO and O, which are parameterized in the model based on abundances at the top of the atmosphere [1, 7]. Species highlighted in gray are those that are included as opacity sources in our Exo-Transmit calculations (Section 2.2.3).

(a) H<sub>2</sub>S deposition is an additional boundary condition alongside the fluxes and is the same across both model templates. This flux, along with fluxes of SO<sub>2</sub> and H<sub>2</sub>, are distributed within the troposphere and meant to account for volcanic outgassing in both models.

a given strong line will have an overestimated photolysis rate. Similarly, species very sensitive to these lines will have an underestimated photolysis rate.

- Comprehensive updates have been made to the photolysis cross sections and quantum yield data for the photochemical model [e.g. H<sub>2</sub>O cross sections from 161]. The updated cross section and quantum yield data were sourced from [78], [110], the JPL Publication 19-5 recommendations [19] and the MPI-Mainz UV/VIS Spectral Atlas [91]; and references therein.

- The treatment of hydrocarbon aerosols has been updated such that different production channels now all contribute to a single particle population. Previously, each production pathway formed non-interacting, distinct particle populations with only one pathway providing opacity in the climate model while the contribution of other pathways was neglected.
- We include new options for hydrocarbon aerosol optical constants, such as new UV-visible refractive index data for early Earth aerosols [58], which are used for the Archean models in this study, and different monomer sizes (ranging from 10 to 70 nm) for fractal particles.

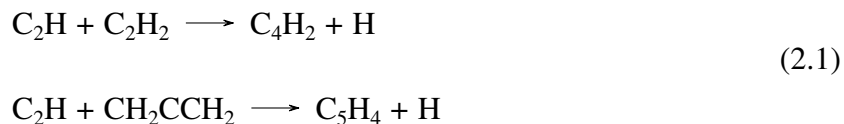
In addition to the list above, we have also implemented an updated convergence scheme for coupled photochemistry-climate models involving significant haze formation (i.e. our Archean Earth models). In contrast to an integrated model that solves both photochemistry and radiative transfer simultaneously, `Atmos` relies on external coupling of historically separate climate and photochemistry models — the two models are run sequentially in an iterative fashion. When the `Atmos` model is run in this manner, the external coupling between the two models may impede a self-consistent atmospheric solution in some cases. Feedbacks between molecular and/or aerosol abundances and the thermal state of the atmosphere can cause the coupled model to oscillate between two non self-consistent solutions with drastically different temperature-pressure and chemical profiles. For example, hazy states can lead to significant atmospheric heating, which in turn will destroy hazes on a subsequent model run — thus impeding overall model convergence. To avoid this problem, we use a “short-stepping” method, in which we do not allow the climate model to fully adjust the temperature-pressure profile to the radiative forcing exerted by the spectrally active species, and instead we interrupt the climate code after a limited number of iterative steps before re-calculating changes to the chemistry with the photochemistry model. Over many

iterations of the coupled code, this allows for more reliable convergence to a self-consistent atmospheric steady-state solution in radiative-convective equilibrium. Only in the final step of a coupled model run, once the thermal structure and chemical composition of the atmosphere appear to have settled into a stable state, do we finally allow the climate model to run to a converged solution.

### 2.2.1.1 Modelling aerosols

Hydrocarbon aerosol particles are thought to have intermittently existed in Earth's atmosphere during the Archean period [e.g., 219]. Such hazes are modeled in our Archean Earth template, replicating a complex mixture of massive molecules with distinct optical properties compared to gas-phase molecular species. These particles are thought to exist in a variety of atmospheric types and planetary conditions [39, 80, 219].

The formation of hydrocarbon haze is initiated by the photolysis of  $\text{CH}_4$  and then proceeds via complex and poorly understood chemical polymerization pathways. As a result, it is not feasible to model the entire chemical reaction network leading to haze production, and we instead follow a common modeling practice of converting certain high-order gas-phase hydrocarbon molecules directly into insoluble haze [7, 101, 107, 139, 148]. For the purposes of our model we assume two high-order hydrocarbon species will ultimately condense into haze particles with a 100% conversion efficiency. These “haze precursors” are  $\text{C}_4\text{H}_2$  and  $\text{C}_5\text{H}_4$ , formed via the reactions:



Large particles scatter very efficiently, introducing significant opacity to an atmosphere, which obscures the spectral features of other molecules and fundamentally alters the thermal balance throughout an atmosphere [6, 7, 8, 106]. The refractive index of experimentally-produced aerosol condensate is influenced by the chemical composition of the gas mixture in which it was produced, and may also be dependent on the energy source used to generate the particles [58, 59, 72, 73, 118, 195]. Gavilan et al. [58] found enhanced UV absorption in oxidized aerosol material produced in early Earth-like  $\text{N}_2/\text{CO}_2/\text{CH}_4$  mixtures compared to more reducing mixtures. The real and imaginary part of the refractive index may exhibit strong wavelength dependence, and data covering the whole UV/Vis/IR range is rarely available, with few exceptions [95].

To contend with these complications, the optical properties of haze particles require specific treatments in our modeling in order to adequately capture scattering, absorption, and emission from particles that consist of agglomerations of hydrocarbons with non-uniform chemical makeup. Several approaches have been used in previous work, including enhanced Rayleigh scattering and Mie scattering approximations. In this work, we follow the approach laid out in [7], which is to treat the hazes as fractal aggregates using the mean-field approximation [17, 163]. Further, we apply the refractive indices of Gavilan et al. [58] for early Earth like atmospheres ( $\text{N}_2:\text{CO}_2:\text{CH}_4=90:8:2$ ) in the UV-visible range over which they were reported, and Khare et al. [95] for the IR.

The mean-field approximation considers the effects of non-spherical haze particles on radiative transfer through the atmosphere. Given refractive indices for a non-spherical particle as a function of wavelength, we can then calculate the extinction coefficient  $Q_{ext}$ , single scattering albedo  $W_0$ , and asymmetry parameter  $G$  (Figure 2.1). These scattering parameters are employed in the two-stream radiative transfer calculations in both the `Atmos` photochemistry routines (for UV wavelengths) and climate routines (for visible / IR wavelengths) to account for multiple scattering off of aerosol particles. These same scattering parameters are also used in our transmission spectroscopy radiative transfer to calculate an effective extinction cross section  $\sigma_{ext}$ , further described in Section 2.2.3 (see Equation 2.3).

As shown in Figure 2.1, we use a grid of haze optical properties spanning radii of 1 nm to 2  $\mu\text{m}$  over wavelengths between 1216  $\text{\AA}$  and 9000  $\text{\AA}$ . In our model, the haze particle radius is determined based the coagulation time scale and removal times scales through diffusion and sedimentation at a given pressure level [7]. Particles are first treated like spherical Mie scatters as they grow from nucleation size to a size of 50 nm, after which they are considered fractal aggregates comprised of spherical monomers. This threshold is chosen to represent previous work done to understand the haze properties within the Archean Earth and Titan’s atmosphere, though we also find that our results are robust to other choices in initial particle sizes [105, 190]. As hazes form and interact with the local radiation field, they can significantly alter the thermal balance of an atmosphere. Previous studies have shown that increasing haze abundance significantly warms high altitudes where they form, while simultaneously cooling the planet’s surface [e.g., 8, 106, 148]. Furthermore, haze properties, particularly for larger particles, are sensitive to small changes in temperature [80], resulting in haze abundance, particle radii, and formation rates varying non-linearly over different temperatures and levels of irradiation. The

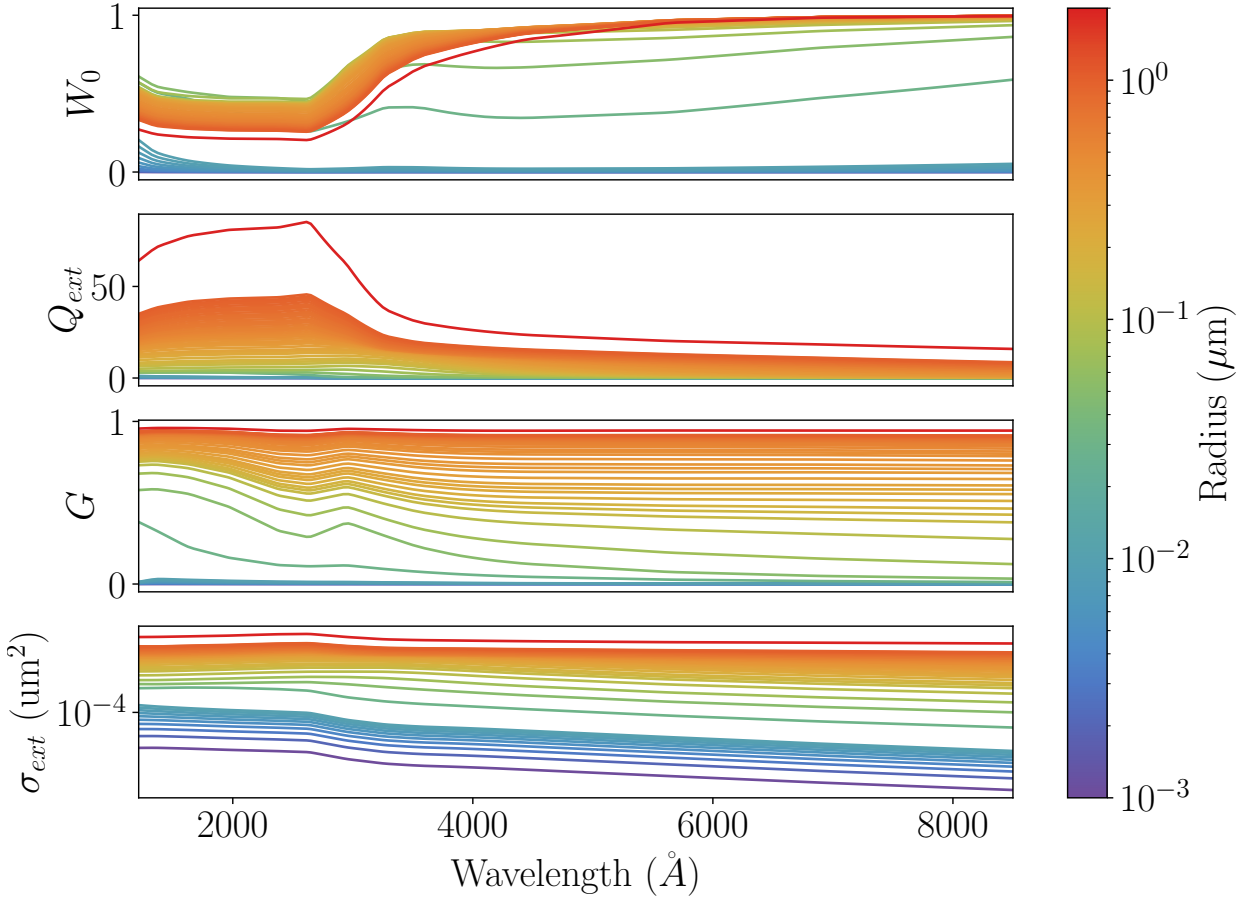


Figure 2.1: Optical properties for fractal haze (radius  $> 50$  nm) and spherical monomer (radius  $< 50$  nm) particles across radii modeled the photochemistry and climate models.  $W_0$  is the single scattering albedo,  $Q_{ext}$  is the extinction efficiency,  $G$  is the asymmetry parameter, and  $\sigma_{ext}$  is the effective haze extinction cross section for transmission spectroscopy. These are the same optical properties employed in both the `Atmos` and `Exo-Transmit` models. These optical properties are calculated using the fractal haze model described in [163] and [17], with haze optical properties from [58] and [95].

use of the `Atmos` coupled climate and chemistry models allows us to model and account for these sensitive feedbacks between haze properties and the thermal structure of the atmosphere.

## 2.2.2 UV input spectra for photochemical modeling

In this study, we focus on the validity and accuracy of reconstructed UV spectra as input to photochemical models. To that end, we select and reconstruct stellar UV spectra using the

following methodology.

Star name	Type	Radius ( $R_*$ )	$T_{eff}$ (K)	$\log_{10}(R'_{HK})$
Sun <sup>(a)</sup>	G2	1.	5800	
GJ 667c	M1.5	0.46	3450	-5.47
GJ 832	M2	0.56	3590	-5.22
GJ 581	M2.5	0.3	3500	-5.75
GJ 176	M2.5	0.45	3680	-4.89
GJ 436	M3	0.45	3420	-5.45
GJ 876	M4	0.38	3130	-5.48
GJ 1214	M4.5	0.21	2820	-5.47
GJ 551 (Proxima Centauri)	M5.5	0.14	3100	-5.23

Table 2.2: Table of MUSCLES stars used in this work. Each of the  $R'_{HK}$  values are taken from Melbourne et al. [132] and the citations therein.  $T_{eff}$  is the star’s effective temperature, and  $R'_{HK}$  is the Ca II H & K line core intensity index.

(a) The solar spectrum is not from the MUSCLES catalog, and instead is the default solar spectrum shipped with the `Atmos` photochemistry model. The model also scales this spectrum based on the age of the Solar System being used, but we do not scale any other spectra with age.

First, we create a set of baseline photochemical models using panchromatic spectra from the MUSCLES Treasury Survey [46, 113, 214]. We use the adaptive, constant-resolution data products to avoid overestimation of flux when handling negative flux bins and re-binning to the `Atmos` wavelength grid<sup>6</sup>. This sample contains 8 M-stars with spectral types ranging from M1.5 to M5.5. In addition, as our 9th host star, we run baseline models using the solar spectrum template included in the `Atmos` code. Figure 2.2 depicts the normalized spectra for all of the MUSCLES M-stars, as well as the Sun. In the following analysis, we treat these spectra as the “ground truth” for the stellar UV, though we discuss the nuances of this assumption in Section 2.5.3. Our baseline model grid is made up of 18 individual `Atmos` runs: models at both modern Earth and Archean Earth initial conditions are produced for each of the 9 host stars. Table 2.2 provides a list of stars used in this work as well as properties relevant to each star’s UV spectrum reconstruction and transmission spectrum calculations.

<sup>6</sup>See the [MUSCLES documentation](https://archive.stsci.edu/prepds/muscles/) at <https://archive.stsci.edu/prepds/muscles/>.

Next, we regenerate each of our photochemical models using reconstructed MUSCLES UV spectra obtained by applying the UV line scaling relations described in Melbourne et al. [132]. Specifically, these scaling relations estimate a given line luminosity using the following equation:

$$\log_{10}(L_{UV}/L_{bol}) = \alpha \log_{10}(R'_{HK}) + \beta \quad (2.2)$$

where  $R'_{HK}$  is the Ca H & K line core intensity index [171],  $\alpha$  and  $\beta$  are fit parameters given in Melbourne et al. [132], and  $L_{UV}$  and  $L_{bol}$  are the UV line luminosity and the star's bolometric luminosity, respectively. Using the values for  $\alpha$ ,  $\beta$ , and  $R'_{HK}$  from Melbourne et al. [132], we reconstruct each of 10 UV emission lines using Equation 2.2. The reconstructed line profiles are taken to be top-hat profiles with 2-Å width (filling two adjacent bins in the 1 Å-resolution input spectrum grid), centered on the line core, and with total wavelength-integrated luminosity equivalent to  $L_{UV}$ . Because the Melbourne et al. [132] scaling relations are only for the strongest UV lines, and because most of the stellar UV flux emanates from these emission lines, we initially make the simplifying assumption of zero UV continuum flux outside of the emission line wavelength ranges. Furthermore, the Melbourne et al. [132] relations are a linear regression of over 24 M-dwarf stars. Due to intrinsic scatter in line intensities across the sample, uncertainties arise in these relations. In this work, we take the reported scaling relation parameters at face-value. We have performed limited tests to assure that our results do not differ significantly when accounting for 1- $\sigma$  scatter in these scaling parameters.

Figure 2.3 shows the full set of UV reconstructed spectra overlaid on the MUSCLES spectra. In total, our full set of UV reconstructed photochemistry models consists of 16 individual Atmos runs — one for each of the MUSCLES M-stars at both modern Earth and Archean Earth

initial conditions. These UV reconstructed spectra effectively simulate a situation in which no observed UV data are available for a given exoplanet host star. This most basic reconstruction — i.e. completely ignoring any possible continuum flux — only has appreciable flux at the reconstructed lines. The remaining wavelengths are set to a constant value of  $10^{-50}$  erg/cm<sup>2</sup>/s/Å, which is vanishingly small but nonzero to avoid numerical instabilities when running the `Atmos` code.

Finally, we run a subset of models designed to quantify the impact of the UV continuum treatment on our results. In these cases we focus on the star GJ 176 (M2.5V), which is a representative early M-dwarf from the MUSCLES sample. In addition to the zero-continuum reconstructions described above, we examine three other approaches for reconstructing the UV continuum. In the three cases described below, and shown in Figure 2.4, the continuum treatment is applied at all UV wavelengths (5 - 4000 Å) other than those of the reconstructed UV emission lines, which are produced using the procedure already described above.

1. Blackbody continuum flux — Because a zero continuum level is certainly an underestimate of the true UV emission, we employ a first approximation of a blackbody UV continuum at a temperature of 9000 K. We select this temperature to compensate for increased UV flux not captured by a blackbody of an M dwarf’s effective temperature. This approach naïvely assumes the bulk of continuum flux originates from thermal radiation from plasma in the upper chromosphere [11, 45, 150]. We normalize our blackbody spectrum such that the total UV flux is equal to the total UV flux for GJ176 in the same wavelength range, minus flux contributions from the lines we reconstruct. Chromospheric temperatures can vary by several thousand degrees [127], which will change the continuum flux from

chromospheric emission appreciably. We choose a 9000 K continuum flux value to roughly follow the continuum flux exhibited in the MUSCLES data for GJ 176 as a test case based on observations.

2. Observed continuum flux — In this approach, we retain the continuum flux recorded by the observed MUSCLES spectra and stitch this together with the reconstructed UV emission lines. The goal here is to quantify how much of the photochemistry is being caused by the observed UV continuum vs. the strong (reconstructed) emission lines.
3. Synthetic continuum flux — Here we replace the continuum with a model UV spectrum. Specifically, we use the HAZMAT semi-empirical model spectra for this set of continuum reconstructions [151], which provide panchromatic spectra generated by the PHOENIX stellar atmospheric code and informed by GALEX and HST observations.
4. Adjacent spectral type — With this method, we take the observed continuum flux from a star of a neighboring stellar type and reconstruct the lines given by the scaling relations.

Figure 2.4 shows the reconstructed GJ 176 spectra using the first three continuum treatments from the list above. These comprise a set of 6 additional photochemical models — one for each continuum treatment at both modern Earth and Archean Earth conditions. We additionally apply the final continuum treatment — employing the continuum of an adjacent spectral type — to the Archean Earth model only, for two different adjacent host star spectra (GJ 581 and GJ 436).

### 2.2.3 Exo-Transmit transmission spectra

The `Exo-Transmit` code [92] is used to generate transmission spectrum observables for each of our model atmospheres. The version of `Exo-Transmit` we use has been modified from the original code to accept the non-equilibrium, vertically-defined chemical abundance profiles output by `Atmos`, rather than the equilibrium chemistry models provided. This modification consists of a major overhaul to the ordering in which chemistry, opacity, and optical depth data are read in and calculated within the code but otherwise leaves the transmission spectrum calculation unchanged.

Mixing ratio profiles for species output by `Atmos` and shaded gray in Table 2.1 are read into `Exo-Transmit`, in addition to  $\text{C}_2\text{H}_2$ ,  $\text{C}_2\text{H}_4$ ,  $\text{C}_2\text{H}_6$ ,  $\text{OCS}$ ,  $\text{NH}_3$ , and  $\text{HCN}$ , which have null boundary conditions in our models (and therefore do not show up in Table 2.1), but form through reactions. The molecular opacities we use for all species are those included in the public `Exo-Transmit` GitHub repository<sup>7</sup> and documented in Kempton et al. [92]. The total opacity for each layer is determined by geometrically weighting the individual species' opacities by their respective mixing ratios in each vertical layer of the atmosphere.

Our hazy (Archean) model runs must also include contributions of hydrocarbon haze particles to the opacity of the atmosphere. To accomplish this, we include the hydrocarbon aerosols as an additional extinction species in `Exo-Transmit` using the following procedure. We first calculate haze extinction cross sections  $\sigma_{ext}$  as a function of particle radius,  $r_{par}$ , according to

$$\sigma_{ext} = \pi r_{par}^2 Q_{ext}(1 - G^2) \quad (2.3)$$

---

<sup>7</sup>[https://github.com/elizakempton/exo\\_transmit](https://github.com/elizakempton/exo_transmit)

where  $Q_{ext}$  is the extinction efficiency, and  $G$  is the asymmetry parameter. (The final term in this equation is a correction based on the asymmetry parameter to account for the fraction of incoming starlight that is forward scattered and therefore remains in the beam.) For each atmospheric layer, the total haze opacity (in units of  $\text{m}^{-1}$ ) is obtained by selecting  $\sigma_{ext}$  at the nearest neighbor to the mean particle radius in that layer and then multiplying by the haze number density output by `Atmos`. We use the same wavelength-dependent haze optical properties from `Atmos` (Figure 2.1) for self-consistency between our `Atmos` and `Exo-Transmit` calculations.

## 2.3 Photochemical modeling results

In this section, we present the results from our photochemical modeling with `Atmos` for the baseline (i.e., observed MUSCLES spectrum) case and zero-continuum UV reconstructions. In general, we find that replacing the UV input with a reconstructed spectrum changes the abundances of photochemically active species. The differences prove significant, especially for our hazy (Archean) models, which exhibit the greatest deviation from our baseline models.

### 2.3.1 Modern Earth

We first present our `Atmos` model outputs for modern Earth conditions for each of the MUSCLES catalog M-stars (Figure 2.5). These models serve as our baseline case against which we will compare all of our UV-reconstructed models, and they also serve as a benchmark for comparison against similar previous works. For example, Wunderlich et al. [212] also modeled Earth-like planets orbiting the MUSCLES M-dwarf host stars using a similar version of the `Atmos` photochemistry-climate code but focusing on detectability of specific atmospheric

spectral features.

Overall, our models are in good agreement with Wunderlich et al. [212], with minor discrepancies being attributable to differences in model setup between our study and theirs. For example, in Wunderlich et al. [212], to preserve “Earth-like” conditions, the authors ran their models varying the instellation such that the planetary surface retained the temperature of modern Earth’s surface; whereas in our own work we retain Earth-like instellation across all of our models. This choice leads to surface temperatures that are on average  $\sim 25$  K higher in our models compared to the fixed surface temperatures of Wunderlich et al. [212]. As a result of the different treatment of instellation, and also presumably due to other subtle differences in model implementation (e.g. reaction rates, opacities, etc.), the Wunderlich et al. [212] version of `Atmos`’ climate model produces slightly differing temperature-pressure profiles compared to ours, including noticeably weaker (but still apparent) thermal inversions for the later-type M-stars.

These changes to the thermal structure of the atmosphere also result in notable differences in mixing ratios throughout the atmospheres.  $\text{H}_2\text{O}$ , which is parameterized below the tropopause as described in [123], is directly tied to the thermal structure at these altitudes. Furthermore, the column depths of photochemical species such as  $\text{O}_3$  differ from the Wunderlich et al. [212] models due to the temperature-sensitivity of their formation conditions.

Overall though, we achieve good qualitative agreement with trends seen in the Wunderlich et al. [212] models as a function of spectral type. Both of our works find more elevated upper-atmosphere temperatures above the tropopause with later spectral type and increasingly apparent stratospheric thermal inversions for later-type host stars. We also both identify general trends of increasing  $\text{H}_2\text{O}$ ,  $\text{CH}_4$ ,  $\text{CO}$ , and  $\text{N}_2\text{O}$  column depths with later spectral type, accompanied by

decreasing  $O_3$ .

We find that our `Atmos` models run with the reconstructed (zero-continuum) UV spectra compare favorably to our baseline models generated from the observed MUSCLES spectra (dashed lines vs. solid lines in Figure 2.5). Some variations, particularly in species dominated by photochemistry such as  $O_3$ , have differences in column depth up to a factor of two to three. Some of the specific host stars, such as GJ 551 (Proxima Centauri), which have observed line luminosities that vary significantly from those calculated with the Melbourne et al. [132] scaling relations, result in `Atmos` model outputs that deviate more severely. We find overall though that reconstructed input UV spectra capture the bulk characteristics of these modern Earth-like atmospheres, and they therefore serve as suitable input to photochemical models in place of observations. For focused studies, variation in trace species or photochemically-dominated species may be significant enough to warrant a more careful treatment.

### 2.3.2 Archean Earth

We similarly model a set of baseline `Atmos` simulations for hazy, Archean Earth-like atmospheres (Figure 2.6). These atmospheres have far more photochemically active species and the potential for strong radiative feedback from haze formation [7]. This results in a greater sensitivity of the Archean Earth models to the UV input spectrum, compared to our modern Earth simulations.

Vertical abundance profiles for hydrocarbon hazes are shown in the lower right-hand panel of Figure 2.6, and the corresponding particle size distributions in Figure 2.7. The disparate optical properties for each `Atmos` simulation (i.e., from the differing particle size distributions) couple

with the thermal properties at haze-bearing altitudes to impact the chemical profiles of other species. These differences are non-linear, with feedback between the climate and photochemistry models playing significant roles in all characteristics of these more complex, hazy atmospheres.

Compared to the modern Earth models, there are not such clear trends with stellar spectral type for both thermal structure and abundance profiles. GJ 551 — the latest M-star modeled — does tend to be an end-member, but overall the lack of clear trends with stellar effective temperature imply that these hazy models are more sensitive to the activity level and exact details of the stellar UV spectrum than for the more “well-behaved” modern Earth models. Of note, this increased sensitivity to the stellar UV is accompanied by increased challenges with model convergence — it generally takes significantly longer for the hazy Archean Earth models to fully converge, and we typically must resort to the model “short-stepping” procedure outlined in Section 2.2.1.

The baseline models demonstrate the sensitivity of haze formation and feedback to small changes in the UV irradiation, and this is further shown when we use our reconstructed UV spectra as inputs. The reconstructed UV spectra often do not accurately reproduce the abundances of certain major species such as CO, O<sub>2</sub>, and C<sub>2</sub>H<sub>6</sub> (shown in Figure 2.6). As for haze formation, in the majority of models, the abundances of haze particles are up to several orders of magnitude lower for our reconstructed spectra, resulting in a significant loss of UV opacity and changes to the thermal structure of the atmospheres.

An exception to our baseline models producing significantly more haze than the reconstructed models, GJ 551 produces orders of magnitude less haze using the MUSCLES spectrum as input compared to the reconstructed UV spectrum. This arises from the substantially higher line and continuum UV flux exhibited by GJ 551 compared to the other baseline input spectrum

cases. This high irradiation photolyzes haze precursors that would otherwise polymerize into haze particles in the model. Coupled with oxidation of haze precursors due to photolysis of CO<sub>2</sub> into oxygen radicals, the haze formation rate in the baseline GJ 551 model is negligible compared to the reconstruction case.

The degree of disagreement between the baseline and reconstructed models, and especially the systematic discrepancies in haze formation, leads us to suspect that other portions of the UV input spectra, beyond just the reconstructed emission lines, may be playing an important role. We revisit this idea in depth in Section 2.5. In the meantime, we conclude that the Melbourne et al. [132] UV reconstructions may not be adequate for modeling the photochemistry in hydrocarbon haze-producing atmospheres.

## 2.4 Transmission spectra results

We next examine how our model-derived temperature and abundance profiles impact the observable properties of the simulated exoplanets — specifically their transmission spectra between 0.3 and 30  $\mu\text{m}$ .

### 2.4.1 Modern Earth

As already shown in Figure 2.5, the dominant absorbing species in the modern Earth models do not differ significantly between our reconstructed and baseline scenarios, especially at the  $\sim$ mbar pressures probed by transmission spectroscopy. As a result, our `Exo-Transmit` transmission spectrum models (Figure 2.8), show negligible differences in the wavelength-dependent absorption produced by any of these model atmospheres, when comparing the reconstructed to

baseline cases.

For this set of modern Earth models, the largest absolute change in transit depth encountered between baseline and reconstructed models is 5 ppm (indicated by green bars for each of the spectra in Figure 2.8), which is below the anticipated noise floor for observatories like JWST. We note that while the 5 ppm bars in Figure 2.8 also make it look as though many of the modeled atmospheres are well out of reach for atmospheric characterization with JWST [with an expected noise floor for many instruments at the  $\sim 10\text{--}20$  ppm level; 126, 172, 173], these bars will scale down proportionally to both the planet’s radius and its equilibrium temperature, indicating that, all else being equal, hotter and larger planets are easier to characterize (further discussed in Section 2.4.2). That said, small, Earth-like planets will be characterizable with JWST with sufficient integration time, such as those of TRAPPIST-1 and some super-Earth TESS discoveries within the habitable zone [e.g., 30, 131, 136].

Our main finding here is that prominent broadband absorbers such as  $\text{H}_2\text{O}$ ,  $\text{CO}_2$ ,  $\text{CO}$ , and  $\text{CH}_4$  — and therefore the transmission spectra themselves — are essentially insensitive to UV spectrum reconstruction for a modern Earth atmospheric scenario.

## 2.4.2 Archean Earth

The Archean models behave more dramatically with respect to UV reconstructions. Figure 2.9 demonstrates the significant variations between hazy models produced in the baseline vs. reconstructed scenarios. The most significant differences between pairs of transmission spectra comes from the haze opacity itself, seen as a gentle downward slope, most prominent in the optical and UV. As discussed in Section 2.3.2, the reconstructed models generally produce less

haze than our baseline models, resulting in shallower transit depths and more prominent molecular absorption features at wavelengths shorter than  $3 \mu\text{m}$ . Differences in the optical scattering slopes between spectra are related to the differing particle size and vertical haze distributions. The magnitude of the differences between baseline and reconstructed transmission spectra also varies considerably with host star, but with no clear progression as a function of spectral type, in agreement with our photochemical modeling results from Section 2.3.2.

Significant discrepancies of up to 20 ppm also arise between our hazy model transmission spectra at IR wavelengths of  $\sim 6, 7, 12,$  and  $20 \mu\text{m}$ , as seen in Figure 2.9. Differences at 7 and  $12 \mu\text{m}$  are attributable to variations in the amount of  $\text{C}_2\text{H}_6$  across atmospheres, which is not as efficiently photolyzed by the reconstructed UV spectra. Differences at 6 and  $20 \mu\text{m}$  are a result of differences in haze abundance and optical properties.

The  $\sim 20$ -ppm differences between our baseline and UV reconstructed models are expected to be marginally distinguishable by JWST, and therefore using reconstructed UV spectra will potentially have observable consequences for these Archean Earth atmospheres. Furthermore, larger and/or hotter planets will produce even larger transmission spectral features, leading to more obvious differences between baseline and reconstructed scenarios for hazy atmospheres. More massive planets are more likely to host hydrogen-dominated atmospheres, resulting in significantly different chemical networks and haze formation pathways when compared to terrestrial atmospheres [e.g., 76]. As a result, differences in bulk composition may impact the nature of hazes produced [137], as well as their vertical distribution throughout the atmosphere, when compared directly to the terrestrial models we use in this study.

## 2.5 UV Continuum treatment results

### 2.5.1 Continuum models

Figures 2.10 and 2.11 show the results of using different UV continuum treatments, described in Section 2.2.2, for our modern and Archean Earth-like models of GJ 176, respectively. In the hazeless modern Earth atmospheres, the choice of continuum treatment has an observationally insignificant impact on the resulting abundance and temperature profiles. The abundances of the most prominent photoactive species (e.g.  $O_3$ ,  $N_2O$ ) are found to moderately depend on the magnitude of the continuum flux. Notably, the  $O_3$  abundance profile deviates significantly for all continuum treatments. These deviations do not prove observationally significant, as shown in Figure 2.12.

Our hazy Archean Earth-like models prove more sensitive to choice of UV continuum. Figure 2.11 demonstrates the severity of these discrepancies, with the worst case scenarios producing several orders of magnitude less haze than models using the baseline MUSCLES UV input spectrum. This translates to molecular species such as  $CO$ ,  $O_2$ , and haze precursors like  $C_2H_6$  differing significantly as well.

As a result of the sensitivity to the UV continuum in the Archean models, the model transmission spectra (Figure 2.13) also differ substantially. This is especially true in the visible and near-IR where the haze impacts on the transmission spectra are most apparent. A comparison between the reconstructed model with zero continuum vs. the one with the observed MUSCLES continuum (blue vs. orange line in Figure 2.13) is especially telling of the role that the UV continuum plays in shaping the properties of hazy atmospheres. Ignoring the continuum entirely

clearly neglects an important haze formation pathway and also impacts the transmission spectra via changes to thermal structures and the abundances of other key absorbers.

The HAZMAT reconstruction best reproduces the transmission spectrum generated from the MUSCLES observations for GJ 176, although the somewhat higher UV continuum in this reconstruction (see Figure 2.4) leads to a modest over-production of haze (seen as a deeper optical transit depth). Overall, we conclude that the UV continuum treatment definitely plays a non-negligible role when modeling hazy atmospheres.

### 2.5.2 Using a neighboring stellar type

Another way to account for continuum flux is to assume that the continuum of an observed star similar in stellar type will be sufficient for UV reconstruction. To that end, we provide a brief assessment of the applicability of such an approach in our GJ 176 reconstruction case.

Rather than using a *model* of the UV continuum, employing *observed* UV data for an actual star may allow us to account for physical effects not adequately captured by a model spectrum. Furthermore, one could hypothetically attempt to match a proxy star's observed continuum to other physical properties of the star one is reconstructing. For example, if a star with similar activity has an observed UV spectrum it may be better than a model or a quiescent spectrum for a neighboring stellar type.

Figure 2.15 shows the results of using the GJ 176 line reconstructions, as done previously (Figures 2.10 and 2.11), but using two different MUSCLES stars for the UV continuum fluxes. In this case, we choose the two stars closest in stellar type compared to GJ 176 (an M2.5V star): GJ 581 (M2.5V) and GJ 436 (M3V). Here we only model Archean Earth conditions —

as Sections 2.3.1 and 2.4.1 have already shown the relative insensitivity of our hazeless (modern Earth) models to the UV continuum. We reconstruct GJ 176’s UV spectrum using one of the neighboring star’s UV continuum to fill between our reconstructed lines using the GJ 551  $R'_{HK}$  values. At non-UV wavelengths the MUSCLES GJ 176 panchromatic spectrum is used (relevant only for the climate model). Once the spectrum reconstruction is complete, the full spectrum is re-normalized to have a total integrated instellation equivalent to Earth-equivalent flux at the top of the atmosphere.

We find that the continua of both stars do a reasonable job of replicating the baseline GJ 176 model, but again noticeable differences do arise. Haze abundances between the three models differ by up to an order of magnitude, and abundances of various molecules (e.g. CO, CH<sub>4</sub>, C<sub>2</sub>H<sub>6</sub>, O<sub>2</sub>) similarly disagree by factors of a few, as seen in Figure 2.15.

As for the resulting transmission spectra (Figure 2.16), significant discrepancies again arise at optical wavelengths due to differing haze abundances and particle sizes among the three models, and also at  $\sim 12 \mu\text{m}$  from C<sub>2</sub>H<sub>6</sub>, C<sub>2</sub>H<sub>4</sub>, and C<sub>2</sub>H<sub>2</sub> absorption. Interestingly, the M2.5 star GJ 581 does manage to replicate the baseline GJ 176 model (itself an M2.5 star) with reasonable accuracy, but only longward of  $2 \mu\text{m}$ . At shorter wavelengths the differences in haze properties become apparent. These differences in simulated transmission spectra for two stars of identical spectral classification indicate that spectral type is not a unique predictor of photochemical behavior of an exoplanetary atmosphere, nor of its observable properties.

### 2.5.3 Which UV continuum treatment is correct?

Based on our results, models with photochemical hazes can vary dramatically, even at an observable level, as a function of the UV continuum treatment applied. With this in mind, it is important to establish which UV continuum treatment is the “best” one to use in the absence of UV observations.

From Figures 2.13 and 2.16, we see that the HAZMAT and neighboring host star continuum treatments do the best job of replicating the behavior of our baseline Archean Earth model for GJ 176 from an observational perspective. In practice, semi-empirical spectral models have only been generated so far for a very limited number of host stars [41, 150, 151, 188], GJ 176 being one of them, and rely on observations of the host stars’ UV spectra for their models. As a result, in many cases it may be impractical to use such a model for replicating the UV continuum of an arbitrary exoplanet host star. Similarly, using observations of a neighboring spectral type for UV continuum reconstruction is also problematic, for reasons discussed in Section 2.5.2 — mainly that spectral type is not a unique predictor of UV continuum behavior. This also applies to using continuum flux from a star of the same stellar type, since factors such as age, composition, and activity level will all affect the strength of the continuum for a given host star. However, in many situations this may be the most practical solution, especially as the library of observed M star UV spectra continues to grow. It should be noted though that the “neighboring spectral type” approach is not guaranteed to produce accurate outcomes for photochemical modeling.

Two further caveats to this finding are as follows. First of all, we have only done a detailed examination of the UV continuum treatment for a single host star — GJ 176 — and therefore our results may not be fully generalizable. Secondly, we have based our modeling approach off of

the premise that the observed MUSCLES spectrum represents the ground truth of the host star's UV output. Unfortunately, due to the intrinsic UV-faintness of many M dwarfs, the MUSCLES-reported continuum fluxes are often representative of the photon-limited noise floor of the data, rather than a true detection of the stellar emission [113]. As a result, the MUSCLES UV continuum fluxes may be overestimates of the true UV emission, especially for fainter stars and at shorter wavelengths.

## 2.6 Conclusions

To summarize our study and its findings:

1. We have used the MUSCLES Treasury survey M-dwarf spectra [46] coupled with UV reconstructions from Melbourne et al. [132] to generate photochemical and transmission spectrum models of terrestrial atmospheres at Earth-like instellation, with and without hazes.
2. We find these reconstructions to be adequate for photochemical modeling of hazeless (modern Earth-like) terrestrial atmospheres. Deviations from our baseline models (i.e., those using the MUSCLES observations) are minimal, though species formed primarily via photochemistry are slightly underestimated. Models generated from MUSCLES observations and UV reconstructions produce nearly identical transmission spectra.
3. Photochemical models of hazy (Archean Earth) terrestrial planets are much more sensitive to the UV input spectrum. Chemical abundances, haze formation rates, and thermal profiles are all significantly impacted by the use of UV reconstructions of host star spectra. These

changes to the atmospheric structure and chemistry have observable implications in the transmission spectra of hazy exoplanets.

4. We further find that our hazy atmosphere results are sensitive to the UV continuum flux, which is not modeled in our nominal UV reconstructions. Changes in continuum fluxes — tested on our models of the early M-star GJ 176 — are also found to impact thermal structures, as well as haze and molecular abundances, at an observable level, resulting in transit spectra with significant differences across a broad range of wavelengths.

Given these results, we find that fully observing a host star’s UV spectrum, including multiple UV emission lines and the underlying continuum, remains the gold standard for modeling exoplanet atmospheres. While the Melbourne et al. [132] reconstructions are a good proxy for M-dwarf stellar spectra for the purpose of photochemically modeling non-hazy Earth-like atmospheres, they do not sufficiently capture a star’s UV spectrum for hazy planet modeling. For that reason, the observed stellar spectrum is especially necessary for predicting and interpreting transmission spectra of hazy exoplanets.

For cases in which it is not possible to observe the host star’s UV spectrum, we recommend the following procedure.

- Reconstruct the strongest UV emission lines using the Melbourne et al. [132] scaling relations. This requires knowledge of star’s the  $R'_{HK}$  index as well as an estimate of its bolometric luminosity — both of which should be readily obtainable through optical characterization. If certain UV lines (e.g. Ly  $\alpha$ ) have been observed, but the rest of the UV spectrum has not, one can use those observed line fluxes in tandem with the Melbourne et al. [132] scaling relations to fill in the fluxes of the remaining emission lines. We reiter-

ate here that [132] find  $R'_{HK}$  to be the most robust predictor of UV emission line strength across the M-dwarf spectral class, and therefore UV emission lines—in the absence of direct observations—should be generated following the  $R'_{HK}$  scaling relations.

- To reconstruct the UV continuum, either choose an observation of a star with a similar spectral type, as done in Section 2.5.2, or employ a synthetic model of the UV continuum, such as those provided by the HAZMAT program [151]. We have found that these two options produce model results most consistent with our baseline cases using the MUSCLES observed UV spectra. For cases in which neither of these two approaches are feasible, a blackbody continuum can be used, following the example of [11].

We note that it remains problematic to make use of observations of the stellar UV continuum in photochemical modeling because in many cases those observations simply represent the photon noise level, rather than a true detection of the stellar emission. We therefore recommend deeper observations of a benchmark set of exoplanet host stars that fully detect and resolve the UV continuum emission, accompanied by improved modeling of M-dwarf spectra in the UV. However, such observations may not be feasible for most exoplanet host stars without a more sensitive far-UV observatory, such as the 6-m UV/optical/IR observatory recommended by the Astro2020 Decadal Survey [143].

In order to generate our photochemical models for well-benchmarked cases, the planetary scenarios we've studied have low effective temperatures and masses compared to many favorable targets for atmospheric characterization. The trends and conclusions reached in this study can likely be generalized to larger, warmer exoplanets, although for such planets disequilibrium processes are less dominant in establishing atmospheric composition. To more accurately predict

trends in such atmospheres would require an extension of this study covering a broader parameter space.

Stellar activity changes the time-averaged high-energy irradiation of a planet's atmosphere, altering the photochemical equilibrium of a planet's atmosphere depending on the rate of flaring [176] and the stellar magnetic activity cycle. Some information about the activity for the MUSCLES target stars is folded into their observed spectra due to flares occurring during exposure time [46, 114], though this does not provide sufficient information to draw conclusions in our work. Since the UV flux during flaring events can increase by several orders of magnitude, understanding how these events change the time-dependent evolution of these atmospheres would improve upon the results, particularly in the case of haze-forming atmospheres.

As the community prepares for future space- and ground-based observatories capable of unprecedented atmospheric characterization, it is critical to understand what complementary data sets will be required to contextualize and interpret these future studies. Here, we have focused on the role that UV observations play in accurate modeling of disequilibrium chemistry in exoplanetary atmospheres. Our results have implications for addressing compelling questions in astrobiology, atmospheric evolution, and aerosol formation — all of which are fundamentally tied to the photochemistry occurring in a planet's atmosphere. Our work motivates the use of the aging HST facility to perform UV observations of exoplanet host stars at high precision as a critical input to photochemical models. Following the demise of HST, future UV missions from the flagship to the SmallSat scale, such as the 6-m UV/optical/IR flagship recommended by the Astro2020 decadal to smaller observatories in the nearer term on the Explorer and SmallSat scales like *CUTE* [37] and SPARCS [5] will have an important role to play in providing further UV information for exoplanet host stars. In the absence of UV observations, proxy scaling relations

and UV reconstruction techniques remain the best path forward.

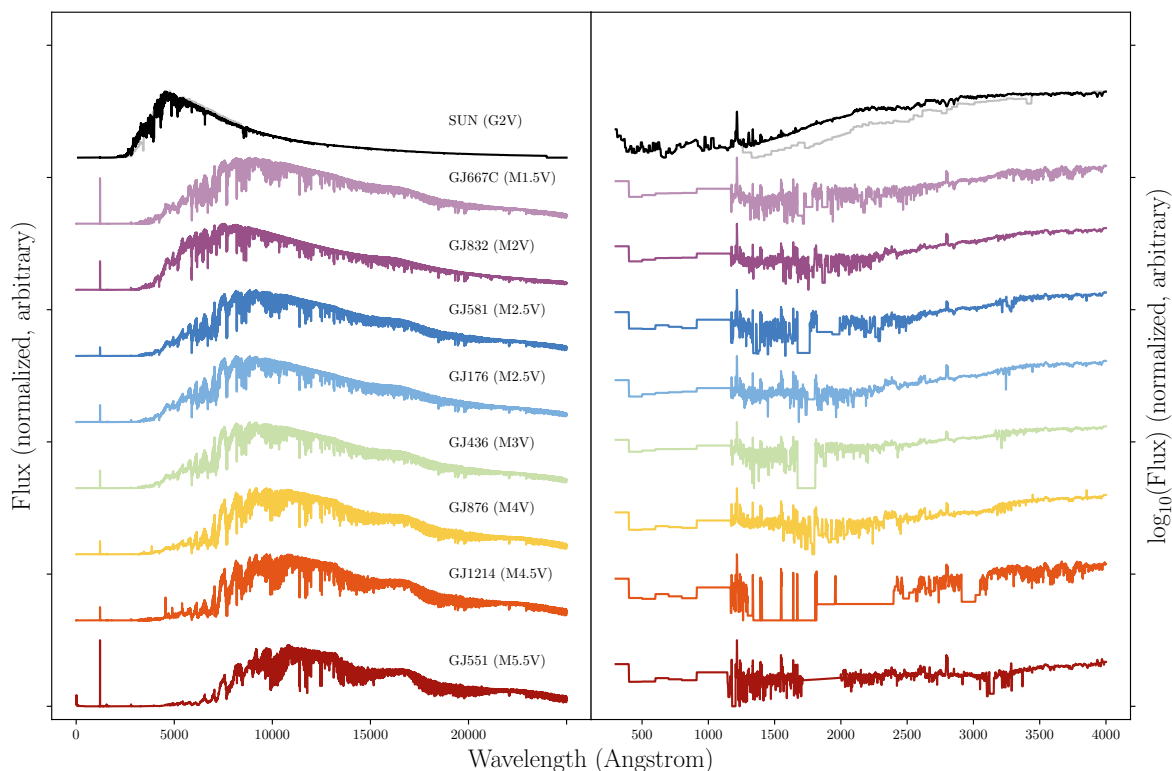


Figure 2.2: The spectra used in this work. The vertical axis represents the normalized stellar flux, with an arbitrary offset applied. When running `Atmos`, each spectrum is re-scaled such that the total instellation is Earth-like for the modern-Earth and Archean simulations, with the exception of the solar Archean model. For our Archean models using the solar spectrum as input, a model following Claire et al. [26] is used to account for predicted differences in the solar spectrum 2.7 billion years ago by scaling the observed modern Solar spectrum [7, 26]. This scaling treatment is not applied to our M-dwarf models, which are a mix of observed and model spectra as described in [45, 46]. The horizontal axis is wavelength, with the left panel being the full panchromatic MUSCLES spectrum (in linear flux units) and the right being a zoom-in on the UV wavelength range over which we reconstruct the spectrum (in log flux units). These UV wavelengths were observed with *HST*.

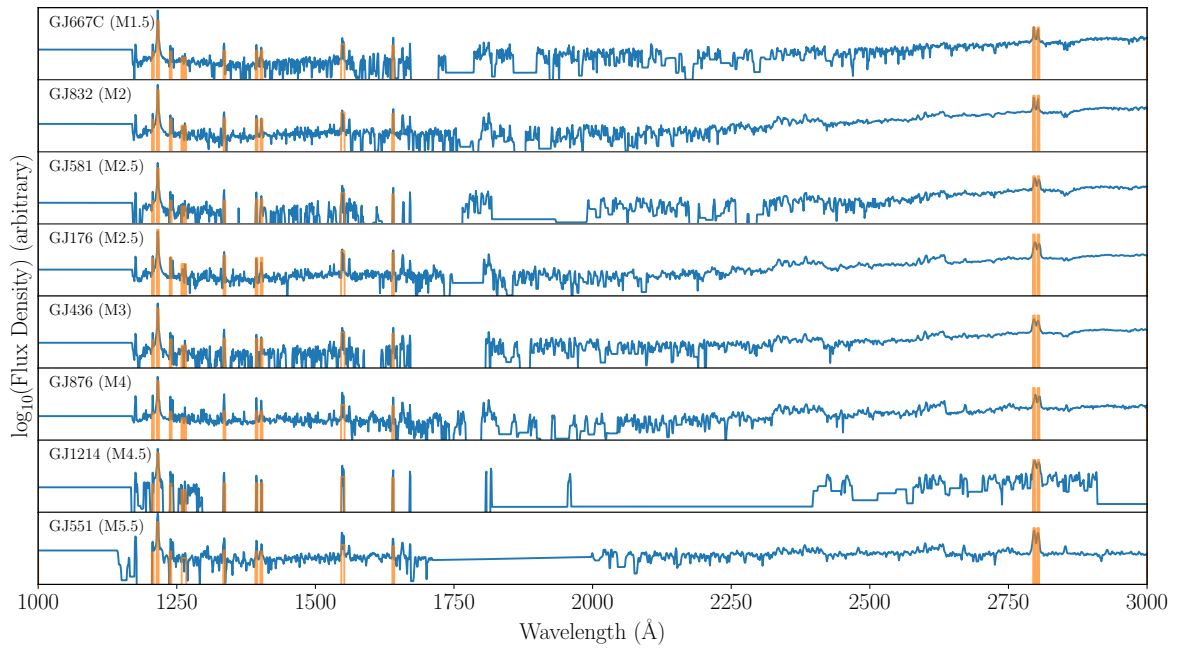


Figure 2.3: MUSCLES spectra (blue) overplotted with our line reconstructions (orange) using the Melbourne et al. [132] scaling relations. The reconstructed line profiles are 2-Å top-hat profiles, as described in the text. The reconstructed spectra shown here have our zero-continuum treatment applied. This wavelength range covers a large part of the *HST* wavelength coverage with COS.

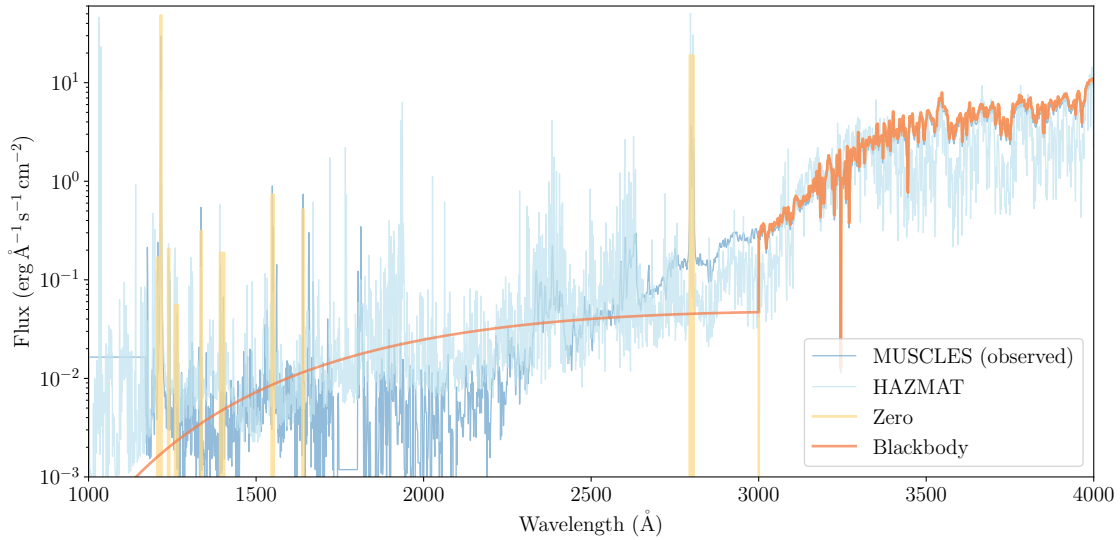


Figure 2.4: Input GJ 176 UV spectra for several of the tested continuum treatments. All cases plotted, save for the baseline observed MUSCLES spectrum case, have the same set of reconstructed emission lines as described in Section 2.2.2. We additionally run a final set of two Archean Earth models using the continua of GJ 581 (M2.5) and GJ 436 (M3) in place of GJ 176 (M2.5). HAZMAT denotes empirical models of UV spectra from Peacock et al. [152] covering the original COS wavelength range observed with the MUSCLES program.

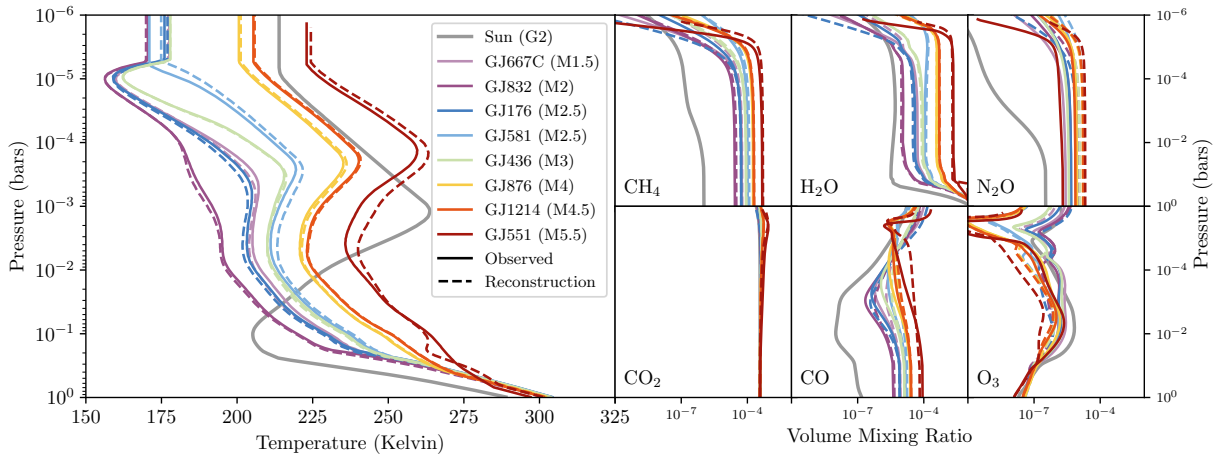


Figure 2.5: Modern Earth model results for our baseline case using the MUSCLES observations (solid curves), and the same models re-run with the (zero-continuum) Melbourne et al. [132] UV spectral reconstructions (dashed lines). These models are effectively haze-free. Vertical temperature-pressure profiles are plotted to the left, whereas mixing ratio profiles for various species (as indicated) are plotted in the right-hand panels. Thermal inversions for the M-dwarf models at  $\sim 10^{-3}$  bar are caused by  $\text{H}_2\text{O}$ , unlike Earth's inversion caused by  $\text{O}_3$  in the stratosphere.

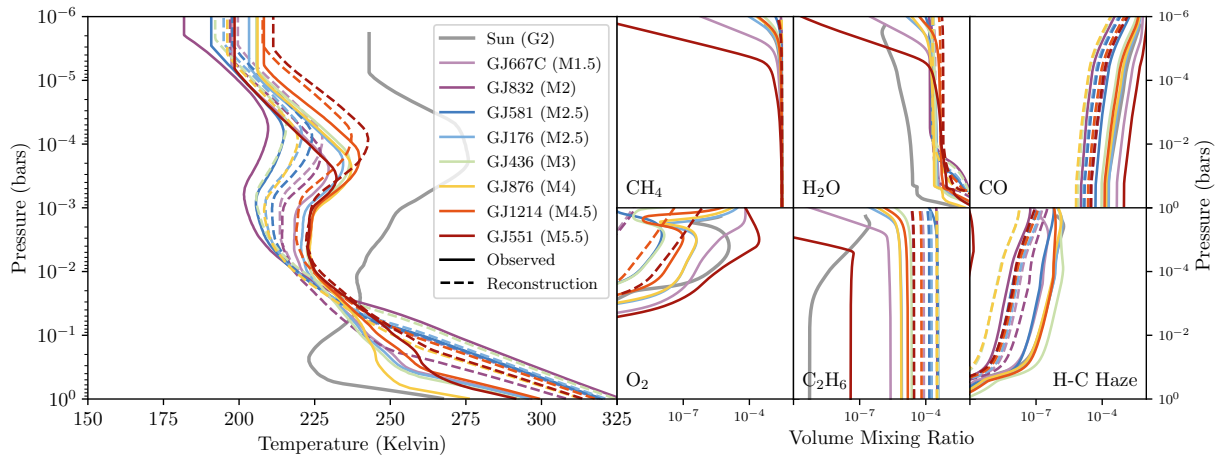


Figure 2.6: Same as Figure 2.5, but for our Archean Earth models including hydrocarbon haze. Significant hydrocarbon haze “precursors” are generated in these models, e.g.  $C_2H_6$ , as seen in the bottom middle mixing ratio panel.

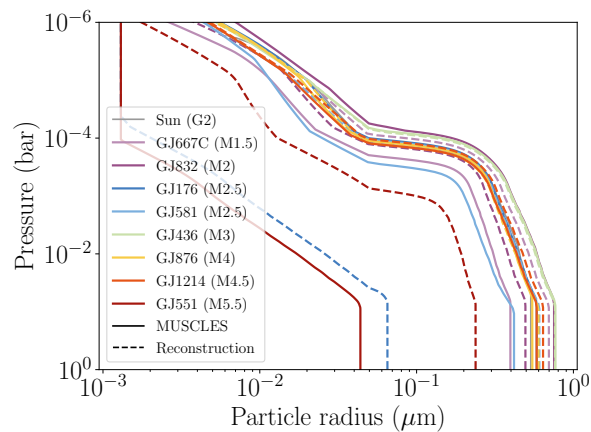


Figure 2.7: Vertical distribution of haze spherical radius. In general, higher incident UV fluxes produce haze particles that are able to sediment into larger radii at all altitudes. This is driven by higher abundances of hazes and haze precursors, which are able to agglomerate and sediment in the presence of more available haze particles. GJ 551 shows significantly smaller haze particle radii due to low abundances of haze precursors to polymerize into particles.

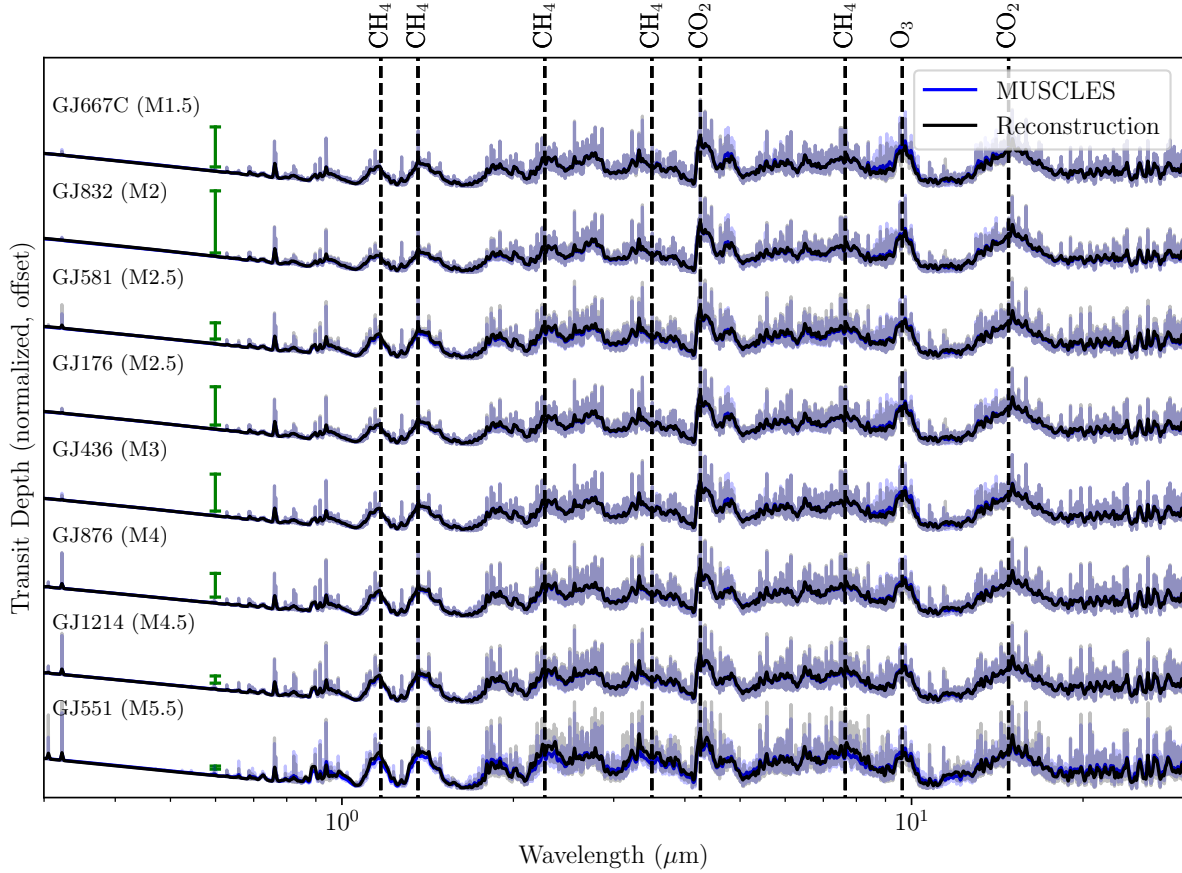


Figure 2.8: Model atmospheric transmission spectra of our Earth-like atmospheres. The black and blue curves are our baseline models with the raw MUSCLES spectrum and reconstructed (zero continuum) UV spectrum as inputs, respectively. The lighter colored lines are the full-resolution transmission spectra output by *Exo-Transmit* (at a spectral resolution of  $R = 1000$ ), while the dark, thick lines are smoothed for ease of visualization. Transit depths in both cases are normalized to the transmission spectrum for the baseline (MUSCLES) model. For reference, the green bars indicate an amplitude of 5 ppm for each host star, assuming the transiting exoplanet is Earth-size. For larger and/or hotter planets, these error bars will shrink proportionately. Spectral features of key molecules are indicated.

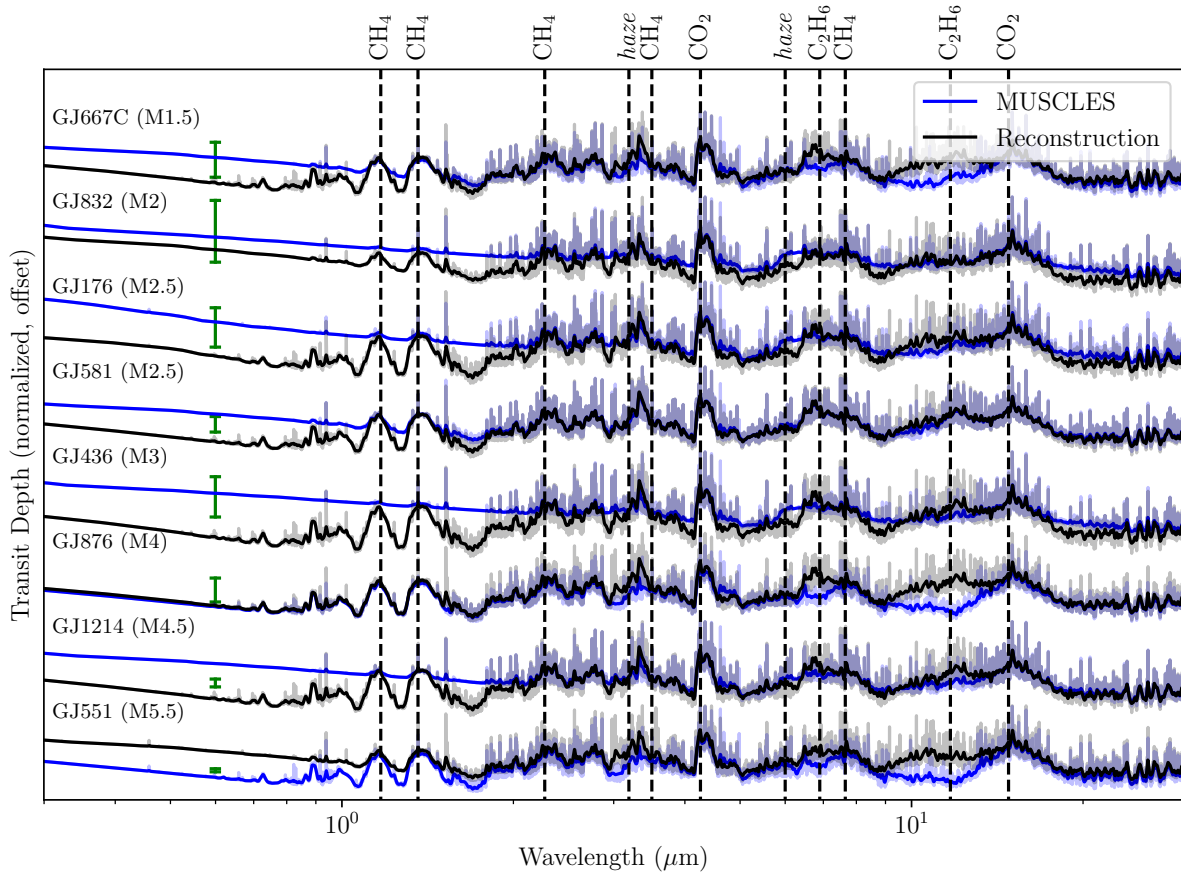


Figure 2.9: Same as Figure 2.8 but for the Archean Earth models. 'haze' indicates features associated with haze particles. For all stars with the exception of GJ 551, the model produces significantly less haze using the reconstructed UV spectra. In the case of GJ 551, our reconstruction actually produces more haze than in the baseline case (see Section 2.3.2.)

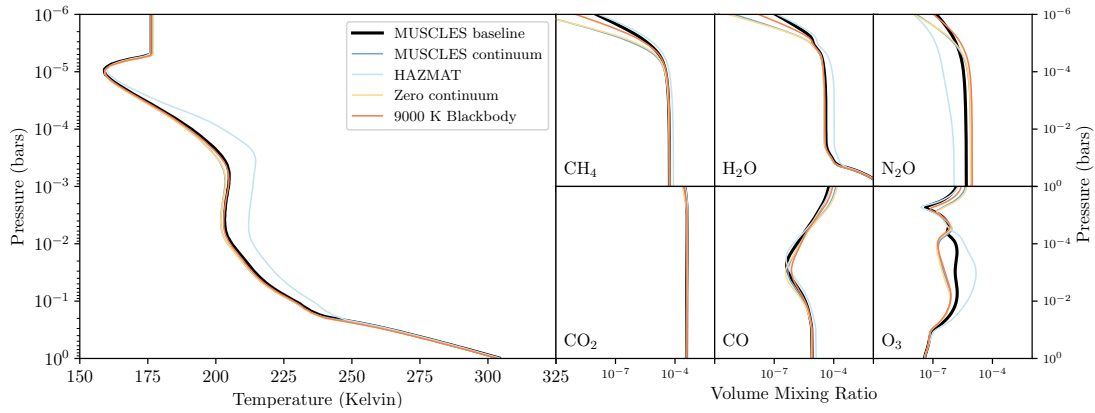


Figure 2.10: Temperature-pressure profiles and abundance profiles for different UV continuum treatments for our modern Earth-like models, specifically using the GJ 176 input case. “MUSCLES baseline” is the model using the raw (observed) MUSCLES UV spectrum. The rest of the models shown use the Melbourne et al. [132] scaling relations to reproduce the star’s UV emission lines, and one of our continuum reconstructions, as indicated. The majority of continuum treatments reproduce the baseline model, and no observationally significant differences arise across models (see Figure 2.13), though photochemically sensitive species such as O<sub>3</sub> and N<sub>2</sub>O deviate for certain continuum treatments.

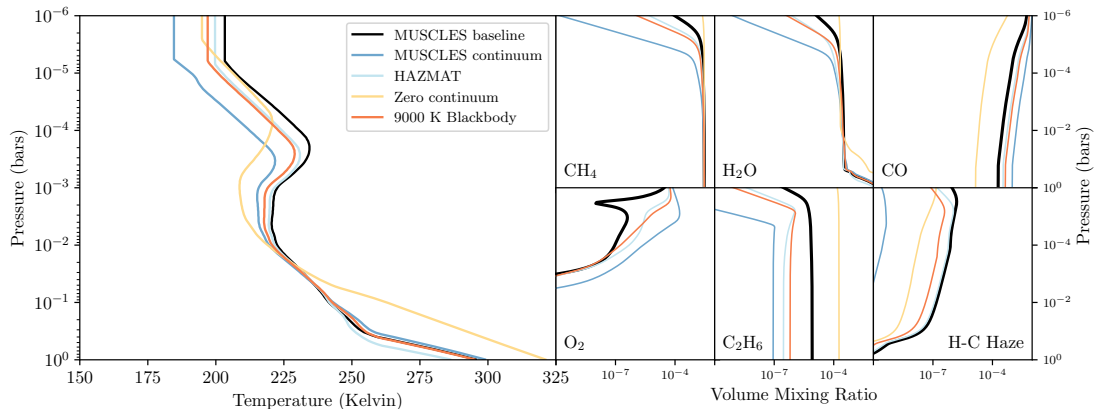


Figure 2.11: Same as Figure 2.10, but for our hazy Archean Earth-like models. These haze-forming models are much more sensitive to the properties of the host star’s UV continuum, particularly for hydrocarbon hazes and their precursors. These lead to observable differences, shown in Figure 2.13.

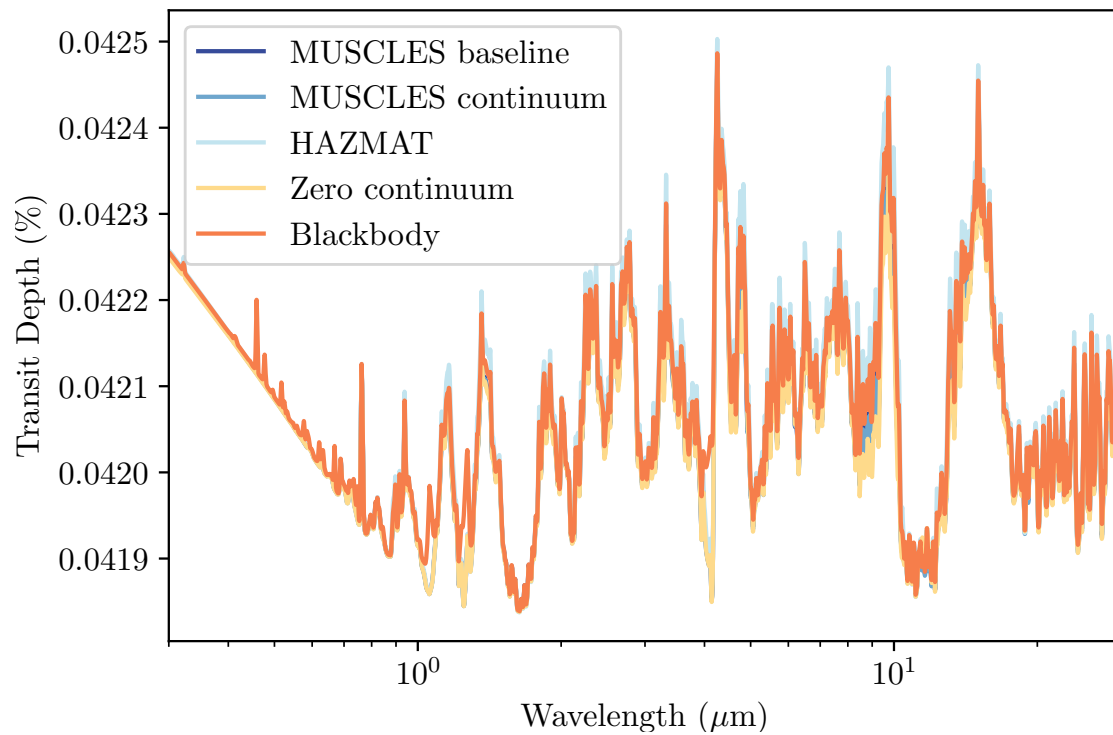


Figure 2.12: Model transmission spectra for modern Earth models of GJ 176 using different prescriptions for reconstructing the host star’s UV continuum, as indicated. The maximum difference of 2 ppm occurs at 1.5  $\mu\text{m}$ , a  $\text{CH}_4$  line, between the baseline and no-continuum case.

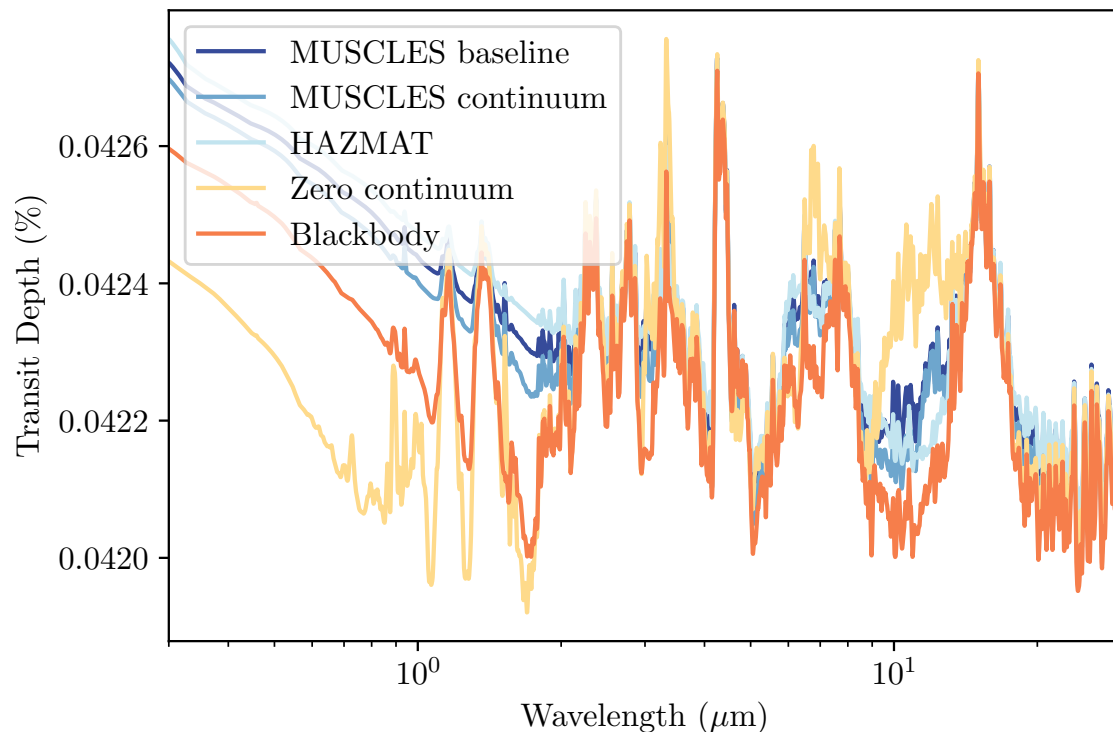


Figure 2.13: Same as Figure 2.12, using hazy Archean Earth-like models for these transmission spectra. A maximum difference between the baseline MUSCLES spectrum and the continuum treatments of 6 ppm occurs at  $1.01\mu\text{m}$  for the zero-continuum case.

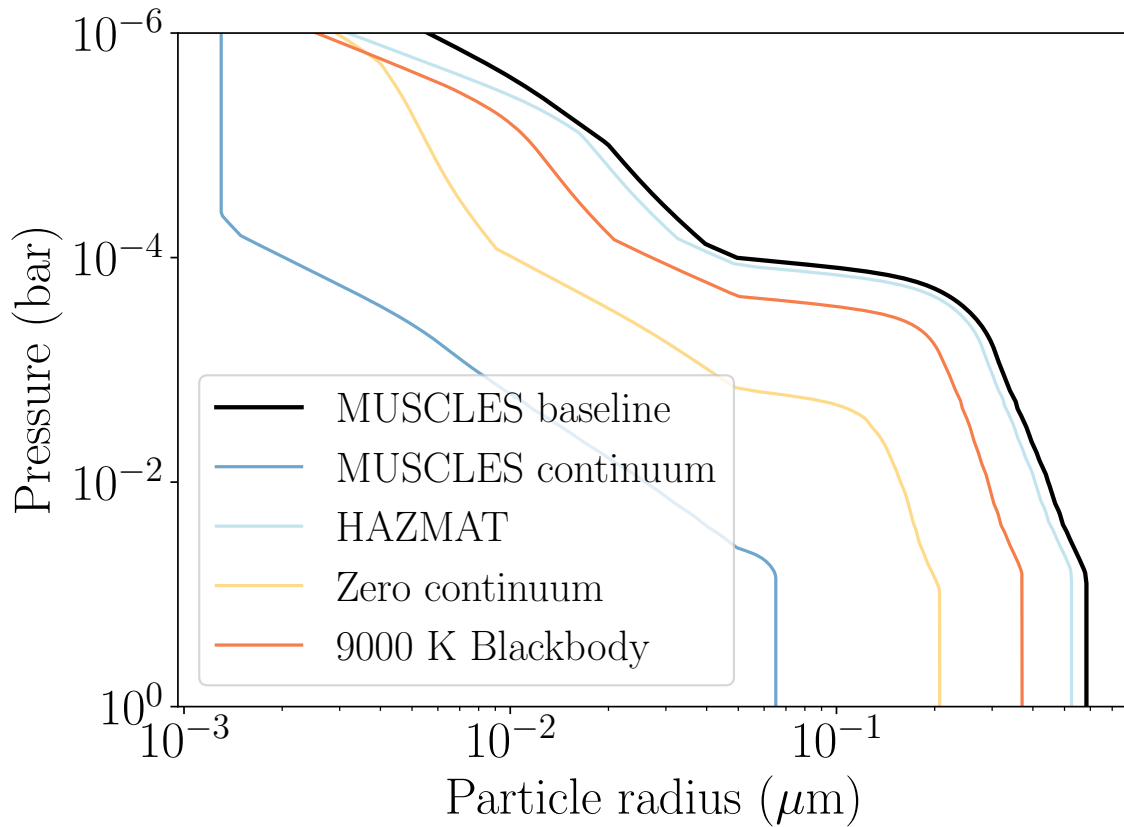


Figure 2.14: Vertical distribution of compact sphere equivalent radius for the various continuum treatments. All reconstructions produce smaller haze particles compared to our GJ 176 MUSCLES baseline case. In general, particle size varies with the total integrated continuum flux. However, when using the MUSCLES continuum flux, very small particles are created compared to any other reconstruction treatments. This is due to significantly variable photolysis rates, reported in the relevant supplementary data for each of our cases.

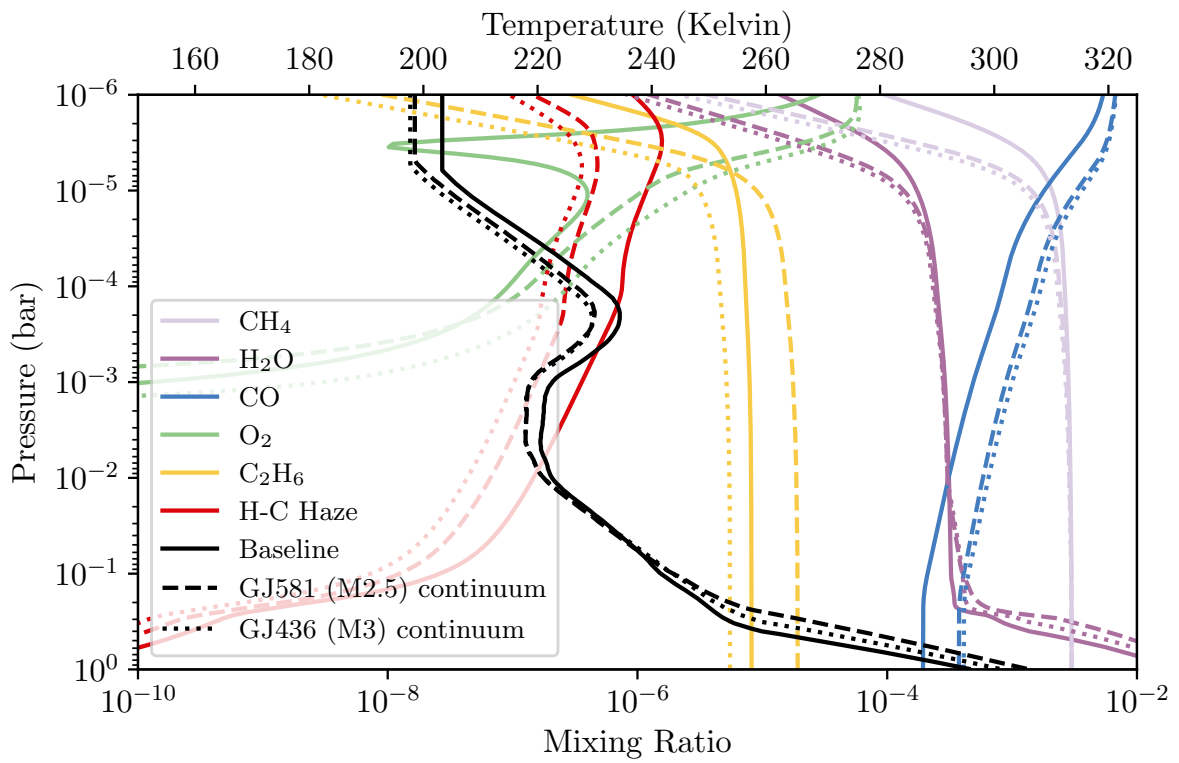


Figure 2.15: Model results using two MUSCLES stars of neighboring spectral types as proxy continua for a GJ176 reconstructed spectrum. Carbon-bearing species such as CO, CH<sub>4</sub>, and C<sub>2</sub>H<sub>6</sub> all have significantly different abundances compared to the baseline case, with the haze nearly an order of magnitude less abundant in either case.

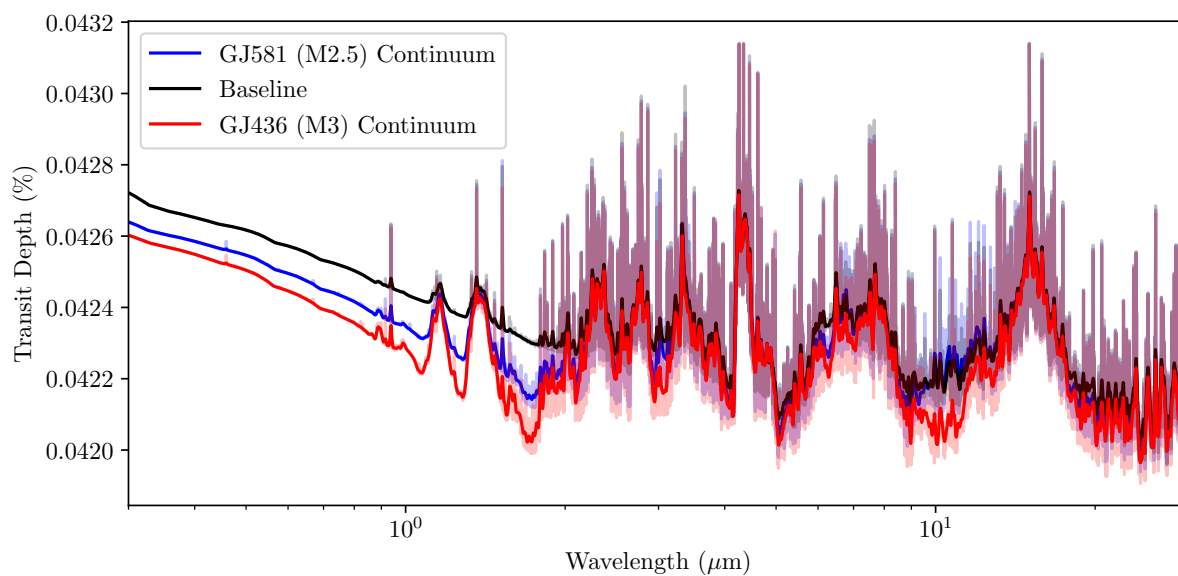


Figure 2.16: Transmission spectra resulting from the model results in Figure 2.15. The different haze abundances shown there are reflected in the transmission spectra’s haze absorption at wavelengths shortward of  $\sim 2 \mu\text{m}$ . Furthermore, a feature at  $10 \mu\text{m}$  is caused by different  $\text{C}_2\text{H}_6$  abundances in the model using the GJ 436 continuum as a proxy.

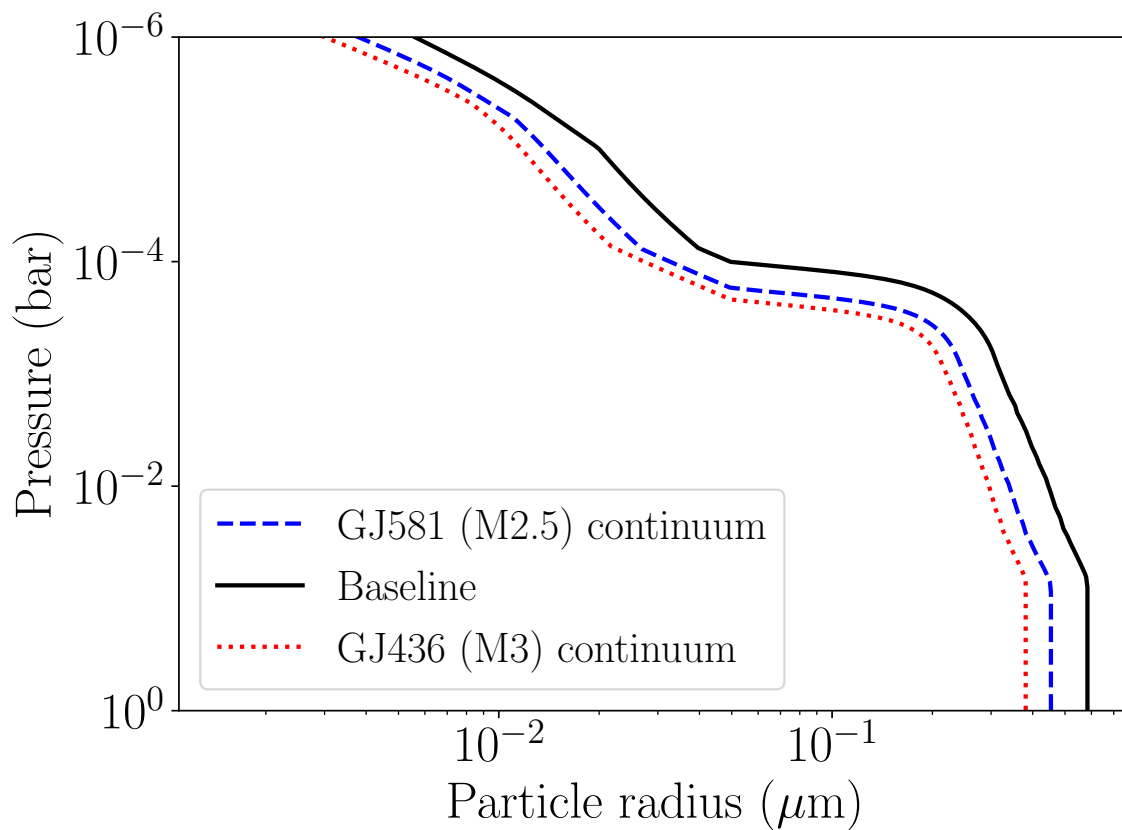


Figure 2.17: Vertical distribution of haze spherical radius using continuum from MUSCLES stars of neighboring stellar types compared to GJ 176 (of type M2.5), as in Figures 2.15 and 2.16.

## Chapter 3: Modeling atmospheres around newly characterized stars — LHS 3844 and AU Microscopii

As discussed in Chapter 2, characterizing host star’s spectra, particularly the UV and higher-energy wavelengths, provides critical inputs to modelling exoplanet atmospheres accurately.

As a part of my dissertation work, I participated in two studies characterizing the spectra of LHS 3944 and AU Microscopii, and modelled Earth-like atmospheres for each of the host stars. In this chapter, I will discuss the background of these studies and provide the results of my contributions with minor modifications and elaborations upon the original works. I discuss the work I performed in detail—specifically, modelling hypothetical and confirmed planets for each of the studies to understand how these observations enhance our capability to model exoplanets in diverse stellar environments.

Section 3.1 summarizes and discusses the work of Diamond-Lowe et al. [32]. Section 3.2 is a similar dissection of Feinstein et al. [36]. This dissertation focuses on the atmospheric modelling I performed for each of these papers, and how it ties into and expands upon previous work in Chapter 2.

### 3.1 Characterizing the high-energy spectrum of LHS 3844

LHS 3844 is a nearby, inactive mid-M dwarf with one confirmed exoplanets (LHS 3844 b) [196]. Although the planet is unlikely to bear an atmosphere greater than 1 bar based on phase-curve data and ground observations [31, 103], this type of star is a favorable one for characterizations of exoplanet atmospheres.

In this work, we describe the pan-chromatic spectrum of LHS 3844 as reported in Diamond-Lowe et al. [32], and then highlight using these spectra with `Atmos` to model a hypothetical, haze-less modern Earth-like planet orbiting in LHS 3844’s habitable zone under quiescent and flaring states. Work described here was published as a part of Diamond-Lowe et al. [32], with Section 3.1.2 being drawn from the text with minor modifications from the published version in *The Astrophysical Journal* to retain flow and clarity.<sup>1</sup> All other text in this section is original text by the author of this dissertation.

#### 3.1.1 Panchromatic spectra of LHS 3844: Flaring and Quiescent

Diamond-Lowe et al. [32]’s primary data product is a panchromatic spectrum of LHS 3844, which is obtained through taking existing observation and models, coupled with unprecedented characterization of LHS 3844’s high-energy spectrum.

This work used *HST*’s Cosmic Origins Spectrograph (COS) instrument to observe the UV spectrum of LHS 3844 at wavelengths of 1131 Å to 3215 Å. Three gratings were use to collect these data, described in Table 3.2. These gratings collectively cover the NUV and FUV regimes of

---

<sup>1</sup>The published paper may be found a the URL <https://iopscience.iop.org/article/10.3847/1538-3881/abfalc> or using the DOI [10.3847/1538-3881/abfalc](https://doi.org/10.3847/1538-3881/abfalc).

<b>LHS 3844</b>	Value	Uncertainty	Reference
Distance (pc)	14.8909	0.0113	[53]
Radius ( $R_{\odot}$ )	0.178	0.012	[103]
Mass ( $M_{\odot}$ )	0.158	0.004	[103]
Effective Temperature (K)	3036	77	[196]
Spectral Type	M4.5V - M5V		[196]
<b>LHS 3844 b</b>			
Equilibrium Temperature (K)	805	20	[196]
Semi-major axis (au)	$6.2 \times 10^{-3}$	$0.17 \times 10^{-3}$	[196]
Instellation ( $\text{erg cm}^{-2} \text{s}^{-1}$ )	$8.59 \times 10^7$		a
Planet Radius ( $R_{\oplus}$ )	1.244	0.006	[103]
Planet Mass ( $M_{\oplus}$ )	2.2	1.0	[24]

Table 3.1: Stellar and planetary parameters for LHS 3844 and LHS 3844 b. All values except spectral type and planet mass taken from Diamond-Lowe et al. [32] with original citations.

\* - The planet’s mass is derived from the relation described in [24].

a - Calculated from other table values.

Grating	$\lambda_c$ (Å)	$\lambda$ (Å)
G130M	1291	1131-1429
G160M	1600	1407-1775
G230L	2950	1678-3215

Table 3.2: *HST* COS instrument gratings used to collect the UV spectrum of LHS 3844. For information about exposure time and instrument modes, see [31].

**Key:**  $\lambda_c$  — central wavelength;  $\lambda$  — wavelength coverage

LHS 3844’s electromagnetic spectrum. These observations were made as a time series, meaning that changes to LHS 3844’s spectrum are captured in real time.

During *HST* observations, LHS 3844 underwent a strong flaring event while observing with the G130M NUV grating, changing the nature of its UV spectrum dramatically. We can use this spectrum to consider the changes in a theoretical planet’s atmosphere when undergoing such events frequently.

Figure 3.1 shows the panchromatic spectra constructed from these observations of LHS 3844 stitched together with models. Specifically, a PHOENIX model matching the physical properties of LHS 3844 is used for wavelengths longer than 3215 Å. For EUV and X-ray wave-

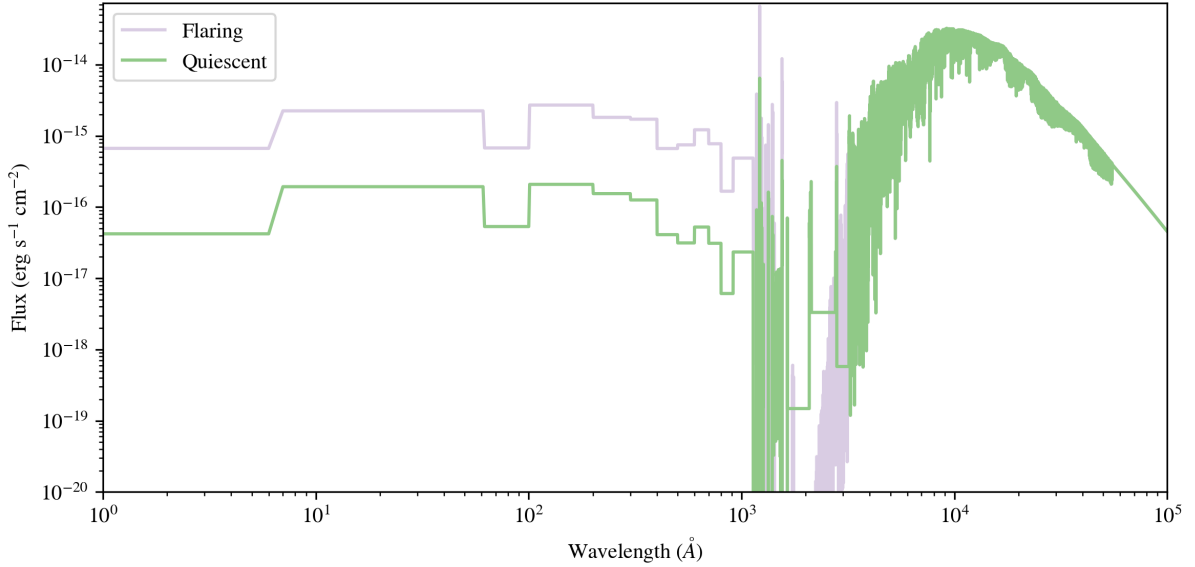


Figure 3.1: Flaring (lavender) and quiescent (green) spectra of LHS 3844. See text for details of constructing these spectra; the observed portion of the spectrum spans 1131 Å- 3215 Å for the quiescent spectrum and 1407 Å-1775 Å for the flaring spectrum, other regions are modelled and combined with these observations to complete the panchromatic wavelength space. Figure and caption shown as in [32].

lengths shorter than 1291 Å, the fluxes are estimated based on a differential emission measure (DEM) and scaling relations for Ly- $\alpha$  ([34] and [215], respectively). Fluxes at optical, infrared, and longer wavelengths are taken from a PHOENIX stellar model with stellar parameters similar to those in Table 3.1.

### 3.1.2 Atmospheric Models

While LHS 3844 b is unlikely to retain an atmosphere, the panchromatic spectrum we present here for LHS 3844 can be an input to atmospheric models of planets in inactive mid-M dwarf systems. For instance, we consider the case of a hypothetical Earth-like planet in the habitable zone of the LHS 3844 system. We use the quiescent and flare LHS 3844 spectra as inputs to

Species	Type	Value	Species	Type	Value
O	Deposition velocity	1.0	O <sub>2</sub>	Fixed Mixing Ratio	$2.1 \times 10^{-1}$
H	Deposition velocity	1.0	H <sub>2</sub>	Fixed Mixing Ratio	$5.3 \times 10^{-7}$
OH	Deposition velocity	1.0	CO	Flux	$3.7 \times 10^{11}$
HO <sub>2</sub>	Deposition velocity	1.0	CH <sub>4</sub>	Flux	$1.0 \times 10^{11}$
H <sub>2</sub> O <sub>2</sub>	Deposition velocity	$2.0 \times 10^{-2}$	N <sub>2</sub> O	Flux	$1.53 \times 10^9$
HCO	Deposition velocity	1.0	H <sub>2</sub> S	Flux	$1.0 \times 10^8$
H <sub>2</sub> CO	Deposition velocity	$2.0 \times 10^{-1}$	HO <sub>2</sub> NO <sub>2</sub>	Deposition Velocity	0.2
NO	Deposition velocity	$3.0 \times 10^{-4}$	NO <sub>2</sub>	Deposition velocity	$3.0 \times 10^{-3}$
HNO	Deposition velocity	1.0	H <sub>2</sub> S <sup>(a)</sup>	Deposition velocity	$2.0 \times 10^{-2}$
SO <sub>2</sub>	Deposition velocity	2.0	H <sub>2</sub> SO <sub>4</sub>	Deposition velocity	1.0
	Flux	$1.0 \times 10^9$	HSO	Deposition velocity	1.0
SO <sub>4</sub> (Aerosol)	Deposition velocity	$1.0 \times 10^{-2}$	S <sub>8</sub> (Aerosol)	Deposition velocity	$1.0 \times 10^{-2}$
O <sub>3</sub>	Deposition velocity	$7.0 \times 10^{-2}$	CH <sub>3</sub>	Deposition velocity	1.0
HNO <sub>3</sub>	Deposition velocity	$2.0 \times 10^{-1}$			

Table 3.3: Static boundary conditions at the surface of our atmospheric model. Deposition velocity has units of cm/s. Flux is a constant surface flux of a species measured in molecules/cm<sup>2</sup>/s. We note that this does not include top-of-atmosphere fluxes, such as downward fluxes of CO and O. These are parameterized in the model using abundances at the top of the atmosphere as described in Arney et al. [7] and Afrin Badhan et al. [1].

(a) H<sub>2</sub>S deposition is an additional boundary condition alongside the fluxes shown here. This flux, along with fluxes of SO<sub>2</sub> and H<sub>2</sub>, are distributed within the troposphere and meant to account for volcanic outgassing on Earth.

the Atmos<sup>2</sup> coupled photochemical and climate model [8] with updated opacities and molecular cross sections [64, 66, 67]. The nondetection of the UV continuum in the HST/COS data leads to negative flux density values in this part of the spectrum, which can create instabilities in the Atmos code. As explored in the previous chapter, these fluxes are critical to accurately modelling species such as O<sub>3</sub> and N<sub>2</sub>O. To avoid numerical problems and ensure accurate models of this hypothetical atmosphere, we create versions of the panchromatic spectra that are binned and resampled to 1 Å such that negative flux density values are eliminated but the overall flux is conserved. This re-binning is of higher-resolution than the photochemical cross sections used in the model, implying that it should be sufficient for accurately capturing photochemical interactions across these wavelengths.

<sup>2</sup><https://github.com/VirtualPlanetaryLaboratory/atmos>

We determine the steady-state temperature–pressure (T–P) profiles and mixing ratios for molecular species under both the quiescent and flare states of LHS 3844. The quiescent and flare spectra result in negligible differences in the T–P profiles, but yield significant differences in mixing ratios (Figure 3.2, left panel). During the flare, additional ozone ( $\text{O}_3$ ) is produced in the upper atmosphere, while oxygen ( $\text{O}_2$ ), water ( $\text{H}_2\text{O}$ ), and methane ( $\text{CH}_4$ ) are dissociated.

The T–P and abundance profiles are fed into a modified version of the open-source `Exo-Transmit` code in order to produce model transmission spectra [92]. With this modification, we are able to read in vertically defined abundance profiles, as opposed to the equilibrium chemistry tables defined on preset T–P grids provided with `Exo-Transmit`. Investigating the timescale of the planet’s atmospheric response to the observed flare is beyond the scope of this work. We note that studies of energetic flares on active M dwarfs like AD Leo imply that they have a lasting affect on the steady state of a planetary atmosphere that may be detectable in transmission spectra [199]. It is likely that LHS 3844 exhibited heightened energetic flaring earlier in its lifetime, but it is not clear how long the relatively small flare we observed in this work would impact a planet’s atmosphere. Based on the T–P profiles we produce for the hypothetical planet we consider here, we do not detect large differences in the resulting transmission spectra (Figure 3.2, right panel).

Based on studies of high-energy flares on active M stars, it is likely that low-energy stellar flares like the one observed in this work would leave atmospheric  $\text{O}_3$  intact if it were to exist in a planetary atmosphere [176, 189]. We are also not likely to see the effects of small stellar flares in the photochemical imprints they leave on planetary atmospheres, though it has been suggested that early stellar activity is a source of abiogenesis [162, 168], which in turn could alter atmospheric compositions on geological times, as with the oxygenation of Earth by cyanobacteria. Atmospheric detections on terrestrial exoplanets are therefore best understood in the context of

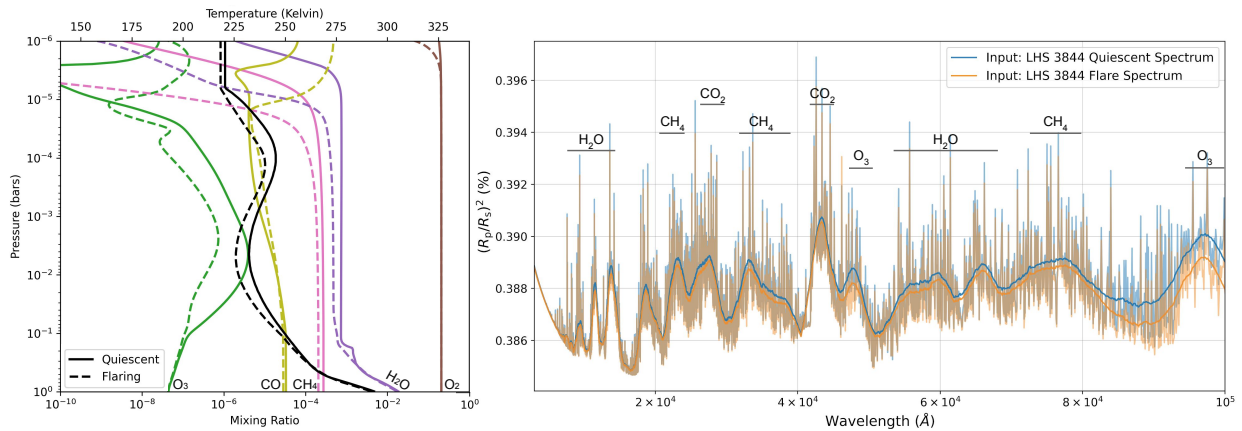


Figure 3.2: Photochemical models for an Earth-like planet in the habitable zone of the LHS 3844 system, with LHS 3844’s quiescent and flare spectra as inputs. Left: T–P profiles for the quiescent and flare cases (black solid and dashed lines, respectively) along with mixing ratios for prominent molecules in Earth’s atmosphere. Right: model transmission spectra derived from the photochemical models. The dominant species contributing to various spectral features are labeled. Figure and caption shown as in Diamond-Lowe et al. [32].

high-energy stellar radiation.

### 3.2 Quiescent and Flaring observations of AU Microscopii in the FUV

AU Mic is an active M-dwarf hosting a circumstellar disk and two known planets, AU Mic b & c. Each of the planets orbits interior to the disk, close to the host star. In this study, a UV spectrum of AU Mic was obtained using *HST*’s COS instrument and used to model theoretical atmospheres for AU Mic b & c.

First, we will describe the nature of the observations and constructing the panchromatic spectrum of AU Mic. We then describe modelling 1-D atmospheric models of AU Mic b & c, as well as their transmission spectra. Work described here was published as a part of Feinstein et al. [36], with Section 3.2.2 being drawn from the text with minor modifications from the published version in *The Astrophysical Journal* to retain flow and clarity.<sup>3</sup> All other text in this section is

<sup>3</sup>The published paper may be found at the URL <https://iopscience.iop.org/article/10.3847/1538-3881/ac8107> or using the DOI 10.3847/1538-3881/ac8107.

original text by the author of this dissertation.

<b>AU Mic</b>	Value	Uncertainty	Reference
Distance (pc)	9.7248	0.0046	[53]
Radius ( $R_{\odot}$ )	0.75	0.03	[205]
Mass ( $M_{\odot}$ )	0.50	0.03	[156]
Effective Temperature (K)	3700	100	[155]
Spectral Type	M1V		[119]
<b>AU Mic b</b>			
Equilibrium Temperature (K)	593	21	[125]
Instellation ( $\text{erg cm}^{-2} \text{s}^{-1}$ )	$3.11 \times 10^7$		a
Semi-major axis (au)	0.0645	0.0013	[125]
Planet Radius ( $R_{\oplus}$ )	4.07	0.17	[125]
Planet Mass ( $M_{\oplus}$ )	17	5	[125]
<b>AU Mic c</b>			
Equilibrium Temperature (K)	454	16	[125]
Instellation ( $\text{erg cm}^{-2} \text{s}^{-1}$ )	$1.07 \times 10^7$		a
Semi-major axis (au)	0.1101	0.0022	[125]
Planet Radius ( $R_{\oplus}$ )	3.24	0.16	[125]
Planet Mass ( $M_{\oplus}$ )	13.6	11.4	[125]

Table 3.4: Stellar and planetary parameters for AU Mic and AU Mic b & c.

a - Calculated from other table values.

### 3.2.1 The Far-UV spectrum of AU Mic

This work used the same instrument as Diamond-Lowe et al. [33], though only using the COS G130M grating (see Table 3.2). This provides a wavelength coverage of 1060 Å-1360 Å, though it masks wavelengths 1210 Å-1225 Å to avoid over-saturation from the star’s Ly- $\alpha$  line, which is then reconstructed using an empirical model outlined in Feinstein et al. [36]. Being an active star, AU Mic’s flaring activity fundamentally shifts the energetic environment of its circumstellar disk and planets, increasing the amount of UV irradiation output by the star several orders of magnitude. Given the proximity of AU Mic, we were able to obtain a significant detection of an M dwarf continuum with these observations.

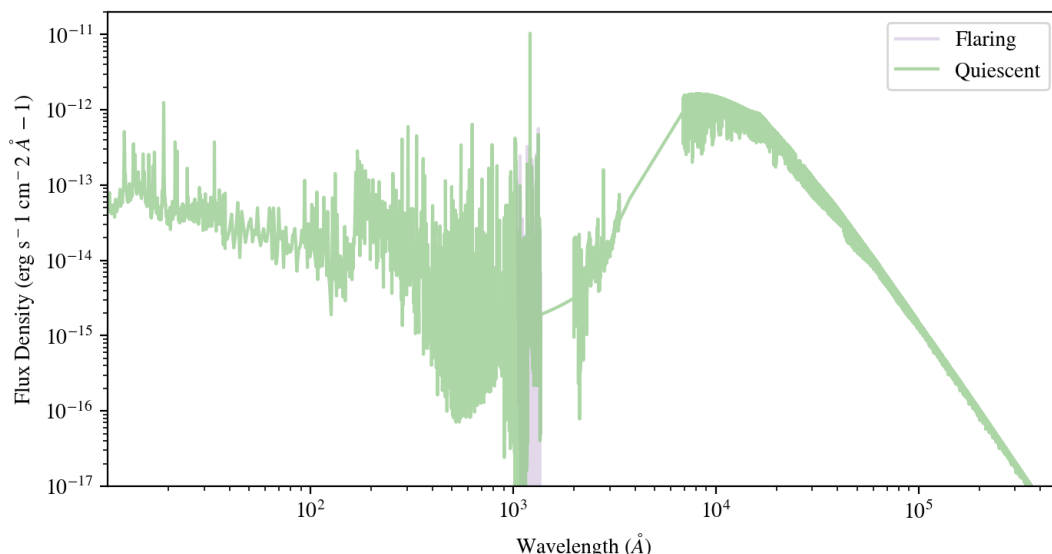


Figure 3.3: Panchromatic spectrum of AU Mic used in Feinstein et al. [36]. Regions without observations or phoenix models are extrapolated in our model using a blackbody function set to AU Mic’s effective temperature and an appropriate bolometric flux at the stellar surface (see Table 3.4). The flaring event only changes fluxes at 1000 Å- 1360 Å as these correspond to the *HST* COS instrument grating used for the observations.

Figure 3.3 shows the flaring and quiescent spectra of AU Mic taken with *HST*. As with LHS 3844, the panchromatic spectra are created by stitching together *HST* observations and several models for unobserved wavelengths.

### 3.2.2 Modelling AU Mic b & c

Stellar activity affects the chemical composition of planetary atmospheres via photochemistry and atmospheric escape. [23] presented chemistry-climate model simulations that explored the effects of G, K, and M dwarf flares on the atmospheres of rocky planets. They demonstrated that the time-averaged flares and accompanying energetic particles can significantly alter the chemical composition of the atmospheres. The global NO and OH increased by an order of magnitude, while the global O<sub>3</sub> decreased by less than an order of magnitude after 300 days of

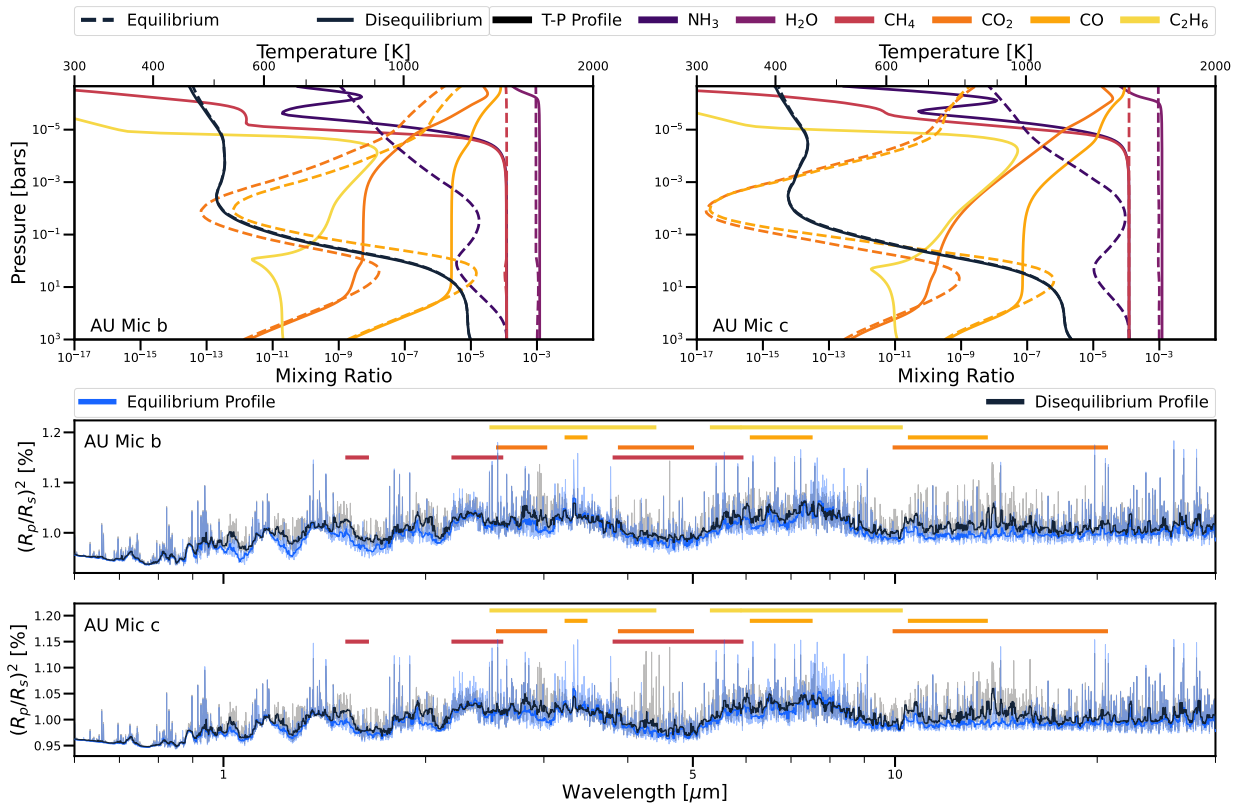


Figure 3.4: Photochemical models for AU Mic b & c. Temperature-pressure profiles (black lines) and mixing ratios (colored) for AU Mic b (top left) and AU Mic c (top right). We model the planets in equilibrium (dashed) and disequilibrium (solid). Normalized transmission spectra as observed from  $0.6 - 12\mu\text{m}$  for AU Mic b (middle row) and AU Mic c (bottom row). Dominant  $\text{CH}_4$ ,  $\text{CO}_2$ ,  $\text{CO}$ , and  $\text{C}_2\text{H}_6$  are labeled in the normalized transmission spectra. These models follow the methods presented in [186] and are evaluated with AU Mic in quiescence.

This figure and caption are presented as in Feinstein et al. [36] with some modifications for clarity. The code that generated this plot is open-source and publicly available at [https://github.com/afeinstein20/cos\\_flares/blob/paper-version/notebooks/tp\\_profile.ipynb](https://github.com/afeinstein20/cos_flares/blob/paper-version/notebooks/tp_profile.ipynb)

post-flare evolution in the atmospheres of planets around M dwarfs.

The atmospheres of AU Mic b and AU Mic c could be pristine tracers of their primordial atmospheres, although they may have experienced metal enrichment by accreting comets [177]. Nevertheless, measuring elemental/compound abundances can provide constraints as to where these planets originally formed within the protoplanetary disk [144]. The chemistry and long-term stability depends sensitively on the XUV irradiance of the host star [84, 187]. Here, we

Species	Type	Value	Species	Type	Value
O	Deposition velocity	0.1	O <sub>2</sub>	Deposition velocity	$1.0 \times 10^{-8}$
OH	Deposition velocity	0.1	H <sub>2</sub>	Fixed Mixing Ratio	0.852
HO <sub>2</sub>	Deposition velocity	$1.0 \times 10^{-2}$	CH <sub>4</sub>	Fixed Mixing Ratio	$4.19 \times 10^{-4}$
H <sub>2</sub> O <sub>2</sub>	Deposition velocity	$1.0 \times 10^{-2}$	NH <sub>3</sub>	Fixed Mixing Ratio	$1.181 \times 10^{-4}$
H <sub>2</sub> O	Fixed Mixing Ratio	$8.215 \times 10^{-4}$	O <sub>3</sub>	Deposition velocity	$1.0 \times 10^{-3}$
HNO <sub>3</sub>	Deposition velocity	$2.0 \times 10^{-1}$	C <sub>4</sub> H <sub>2</sub> (Aerosol)	Deposition Velocity	$1.0 \times 10^{-8}$
C <sub>5</sub> H <sub>2</sub> (Aerosol)	Deposition Velocity	$1.0 \times 10^{-8}$			

Table 3.5: Static boundary conditions at the surface of our atmospheric model for AU Mic b & c. Deposition velocity has units of cm/s. We note that this does not include top-of-atmosphere fluxes, such as downward fluxes of CO and O. These are parameterized in the model using abundances at the top of the atmosphere as described in Arney et al. [7] and Afrin Badhan et al. [1].

model transmission spectra of AU Mic b and AU Mic c in quiescence using the panchromatic spectrum presented in Figure 3.3. We note that AU Mic b & c have the highest Transmission Spectroscopy Metrics ( $\geq 350$ , Kempton et al. 93) of all known young transiting exoplanets, making these planets priority targets for future JWST observations.

Here we summarize the methods used for this calculation. We run the `Atmos` 1-D photochemical model for solar composition atmospheres of AU Mic b & c. We use a recently updated version of `Atmos` which is appropriate for atmospheres of sub-Neptune (i.e. hydrogen-rich) composition, as described in Harman et al. [70]. This updated version includes the addition of reactions for nitrogen-bearing species and the hydrocarbon haze prescription from Arney et al. [7, 8]. The temperature-pressure profiles used were computed with the `HELIOS` radiative-convective equilibrium radiative transfer code [120, 122] for AU Mic b & c analog planets with 500 K and 600 K equilibrium temperatures, respectively. The photochemical modeling was conducted using the stellar input spectrum for AU Mic from Figure 3.3, scaled such that the top-of-atmosphere flux corresponds to the orbital distances of each planet as reported by [125]. We then run the resulting atmospheric abundance profiles from the photochemical modeling through an updated version of the `Exo-Transmit` radiative transfer code discussed in the previous section to pre-

dict the transmission spectra for both planets [92]. For this calculation, we followed the methods presented in detail in Teal et al. [186].

Figure 3.4 shows two `Atmos` disequilibrium (black) and two `FastChem` [183] equilibrium (blue) models for AU Mic b & c, as well as affiliated mixing ratios and temperature-pressure profiles. Both cases use the same temperature pressure profiles, since we do not account for the feedback of disequilibrium chemistry on the thermal structure of the atmosphere. The equilibrium chemistry models do not capture the formation of species such as  $\text{CH}_4$ ,  $\text{CO}_2$ ,  $\text{CO}$ , and  $\text{NH}_3$ , which are under predicted at altitudes that influence the transmission spectrum for these atmospheres. As a result, prominent spectroscopic features such as the  $10.5 \mu\text{m}$   $\text{CO}_2$  feature are absent from transmission spectra using equilibrium chemistry assumptions (see Figure 3.4, bottom two panels).

Although we include hydrocarbon haze formation pathways in each of our `Atmos` models, neither of our atmospheres form significant amounts of photochemical haze. We find that without data within the regions of  $1500 \text{ \AA}$ - $2000 \text{ \AA}$ , photolysis of hydrocarbon species typically resulting in the formation of hydrocarbon hazes are somewhat under-productive. Compounding this, in our disequilibrium models a significant abundance of  $\text{C}_2\text{H}_6$  forms and proves relatively stable at high altitudes, removing C that may otherwise be available to form large haze monomers in our haze production model. JWST is capable of obtaining in-transit spectra from  $0.5 - 28 \mu\text{m}$ . It is unclear what level of contamination from stellar activity will be present in these data [160, 218]. Any of the instruments on JWST can be used to measure the transit depth and The higher resolution of NIRSPEC compared to NIRISS would make this an ideal instrument to observe  $\text{H}_2\text{O}$  and  $\text{CO}_2$  at  $\lambda < 5.3 \mu\text{m}$ . Additionally, MIRI could be used to look at  $\text{H}_2\text{O}$ ,  $\text{CH}_4$ , and  $\text{O}_3$  at  $\lambda > 5 \mu\text{m}$ .

While any of its instruments can be used to measure the transit depth and distinguish be-

tween the equilibrium and disequilibrium models, the primary differences for AU Mic b & c lie at  $\lambda < 3 \mu\text{m}$ . Due to  $\text{CH}_4$  and  $\text{C}_2\text{H}_6$  having drastically different abundances at the altitudes probed by transmission spectroscopy (see top sub-plots of AU Mic b & c in Figure 3.4). For AU Mic b at  $1 \leq \lambda \leq 2 \mu\text{m}$ , we estimate differences in transit depths of  $\approx 200$  ppm between the two presented models. While for AU Mic c, we estimate differences of  $\approx 70$  ppm. For AU Mic b & c at  $3 \leq \lambda \leq 5 \mu\text{m}$ , we estimate differences transit depths of  $\approx 160$  ppm. All values predicted by these models are above the estimated noise floor for JWST [126, 172, 173].

[186] identified that uncertainties in the UV continuum of exoplanet host stars are the primary drivers of uncertainties of photochemical models for hazy exoplanets. With the addition of AU Mic’s continuum in our panchromatic spectrum, we are able to further constrain our uncertainties. In general, it is challenging to detect the continua of relatively faint M stars. . Because of this, AU Mic is an essential benchmark star for understanding UV continua of M dwarfs, and accurately modeling transmission spectra for planets around these types of stars.

### 3.3 Summary

During the course of this thesis, I used a fully-coupled atmospheric model to understand the nature of atmospheres around stars with different levels of activity, taking new *HST* observations and applying the same treatments used in Chapter 2. This work extended the results of Chapter 2 by reaffirming the importance of host star characterization to interpret observations of atmospheres around M-dwarfs.

However, the inputs to our model serve as one facet of uncertainty in our understanding of exoplanet atmospheres. Another pressing subject of investigation is the origin and nature of

hazes in exoplanet atmospheres, and whether our current understanding of hazes themselves is sufficient to make predictions through forward modelling.

## Chapter 4: The origins of haze via the protoplanetary disk

### 4.1 Volatile carbon content as a pathway to haze formation

Planets, especially their atmospheres, are defined by their formation histories. The composition and structure of the protoplanetary disk determines where and how planets form in proximity to their host star.

The work here was performed as part of Bergin et al. [13] originally published in *The Astrophysical Journal*,<sup>1</sup> with an introduction written by the author of this dissertation and Sections 4.1.2 and 4.2, which are work performed by the author of this dissertation, are included with light editing for clarity and flow. I performed much of the atmospheric modelling, and all of the transmission spectrum modelling outlined in this section, including modifying to include new haze opacity calculations for three separate hazes of different radii and vertical distributions.

#### 4.1.1 The planetary nebula

The protoplanetary disk is structured radially around the host star, with parts of the disk closer to the host star experiencing higher irradiation than further regions of the disk. This leads to the formation of “snow/ice lines”—distances at which certain compounds are able to solidify.

---

<sup>1</sup>For convenience, the original published work may be found at the following URL <https://iopscience.iop.org/article/10.3847/2041-8213/acd377> or using the DOI [10.3847/2041-8213/acd377](https://doi.org/10.3847/2041-8213/acd377).

Bergin et al. [13] postulates that a “soot” line, defined as the place in the disk where organic compounds are completely destroyed by irradiation and thermal environment, is a key location in the protoplanetary disk that directly influences carbon content in planetary atmospheres should form within or beyond this point in the disk.

Historically, such lines have been foundational to our understanding the dispersion of H<sub>2</sub>O and CO in the solar nebula. The H<sub>2</sub>O-ice and CO-ice lines, which correspond to oxygen and carbon availability to planets, are of considerable important to planetary formation [144]. However, not all carbon originates in volatile compounds that freeze out far away (several AU) from the host star. Large organic compounds carry a significant amount of the carbon content in the interstellar medium [2, 12, 135]. These compounds are in the solid phase at relatively high temperatures, and at a specific temperature are decomposed into more readily volatile elements which cannot return to the solid state [109]. The disk beyond this “soot line”, as further described in Bergin et al. [13], could prove a carbon source for protoplanetary accretion interior to the H<sub>2</sub>O-ice line. Of note, the location of the soot line can vary by orders of magnitude depending on the speed of disk accretion onto the host star [109], and other physical processes could deplete its carbon by destroying these soots and losing the constituent volatile compounds [79].

In this work, we modelled sub-Neptune atmospheres that would evolve from the formation scenarios described in Bergin et al. [13]. These formation scenarios could produce atmospheres highly enriched in carbon, which in turn could produce large amounts of hydrocarbon haze. We contributed the following text and figures, which have been edited for clarity and flow from the original work.

% Soot <sup>a</sup> (by mass)	% H <sub>2</sub> O <sup>a</sup>	M <sub>p</sub>	M <sub>p,soot</sub> (M <sub>⊕</sub> )	M <sub>p,H<sub>2</sub></sub>	P (MPa)	log <sub>10</sub> (f <sub>O<sub>2</sub></sub> )	N <sub>2</sub>	H <sub>2</sub> O	H <sub>2</sub>	CO <sub>2</sub>	CO	CH <sub>4</sub>	Element Fractions		
													H	O	C
1.0	0.0	0.30	0.003	8.7×10 <sup>-8</sup>	84.08	-10.47	0.00	0.04	0.23	0.03	0.66	0.03	0.314	0.351	0.335
1.0	0.0	1.00	0.01	1.5×10 <sup>-4</sup>	98.47	-10.55	0.00	0.05	0.33	0.02	0.52	0.07	0.459	0.271	0.270
1.0	0.0	3.00	0.03	1.4×10 <sup>-2</sup>	2970.00	-14.80	0.00	0.00	0.59	0.00	0.00	0.41	0.874	0.000	0.126
0.1	0.0	0.30	0.003	8.7×10 <sup>-8</sup>	71.28	-10.19	0.00	0.00	0.01	0.05	0.94	0.00	0.007	0.508	0.484
0.1	0.0	1.00	0.01	1.5×10 <sup>-4</sup>	70.52	-10.26	0.01	0.01	0.07	0.04	0.87	0.00	0.082	0.471	0.446
0.1	0.0	3.00	0.03	1.4×10 <sup>-2</sup>	866.10	-14.80	0.00	0.00	0.95	0.00	0.00	0.05	0.977	0.000	0.023
0.1	1.0	0.30	0.003	8.7×10 <sup>-8</sup>	109.34	-10.36	0.00	0.08	0.50	0.01	0.29	0.10	0.668	0.165	0.167
0.1	1.0	1.00	0.01	1.5×10 <sup>-4</sup>	188.16	-10.43	0.00	0.06	0.42	0.01	0.28	0.21	0.679	0.135	0.186
0.1	1.0	3.00	0.03	1.4×10 <sup>-2</sup>	1120.00	-14.84	0.00	0.00	0.96	0.00	0.00	0.04	0.983	0.000	0.017

<sup>a</sup>Percent mass added to M<sub>p</sub>.

Table 4.1: Base Atmosphere properties and composition for our soot-forming models. These were generated using equilibrium chemistry models outlined in Bergin et al. [13] that account for excess carbon accretion from the protoplanetary disk and geochemistry at the planet’s surface. These are used as inputs to our 1-D atmospheric model to serve as boundary conditions and to initialize our model with an appropriate metallicity and C/O ratio. This table was recreated from Bergin et al. [13].

#### 4.1.2 Implementation of Haze Model

Models of haze formation have been developed for exoplanetary atmospheres based upon irradiation of methane and other carriers. We apply one such model including chemical kinetics, photochemistry, and haze formation to our 3 M<sub>⊕</sub> planet with 0.1% soot and no water. We stress that this hydrocarbon-based haze model is for illustrative purposes. Our calculations show that these atmospheres will be methane rich. But nitrogen and sulfur are carried alongside carbon within soot [3]. Thus, other chemical solutions for hazes are possible. Regardless, methane will be present in these systems in abundance.

The baseline haze model is discussed in Section 4.2. We specifically model the planet at an equilibrium temperature of 600 K placed in orbit around an M-dwarf host star to align its properties with sub-Neptune exoplanet targets that will be observed with JWST during its first year of operations. The resulting chemical abundance profiles are presented in Fig. 4.1, which demonstrate that these atmospheres readily produce hazes via hydrocarbon polymerization channels.

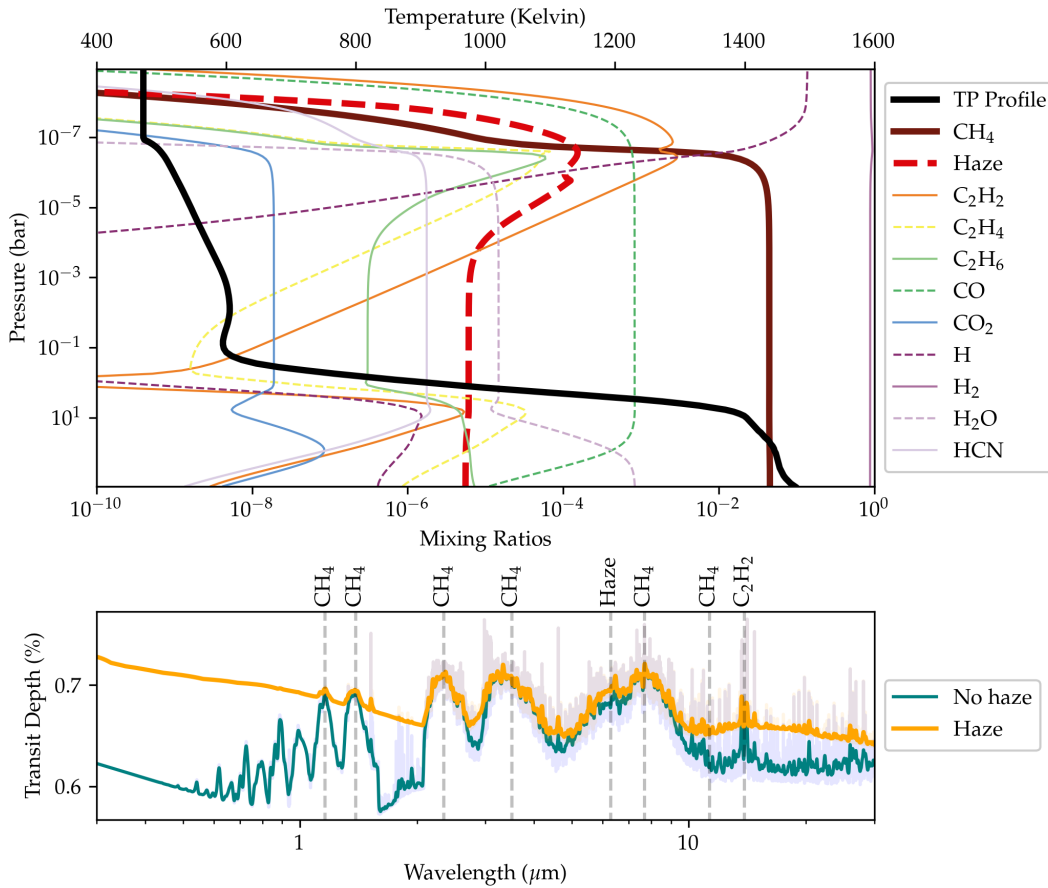


Figure 4.1:

**Top panel:** Abundance and temperature-pressure profiles for a  $3 M_{\oplus}$ , 600 K equilibrium temperature planet, with 0.1% soot, orbiting an M-dwarf star. Even under the harsh UV irradiation environment of the host star, high abundances of methane (thick brown line) persist to high altitude and low pressure. A combination of methane photolysis in the upper atmosphere, vertical mixing, and thermochemistry give rise to significant quantities of higher-order hydrocarbons such as C<sub>2</sub>H<sub>2</sub>, C<sub>2</sub>H<sub>4</sub>, and C<sub>2</sub>H<sub>6</sub>. Subsequent photolysis and polymerization reactions result in the formation of hydrocarbon haze (thick dashed red line).

**Bottom panel:** The resulting model transmission spectrum (orange line) of this planet is shaped considerably by haze with some strong methane features permeating through the haze at longer wavelengths. The teal line shows the transmission spectrum of the same planet but with the haze opacity artificially removed, while the transparent colored line shows these data at a spectral resolution of  $R=1,000$ .

This figure and its caption are lightly modified from its corresponding figure in Bergin et al. [13].

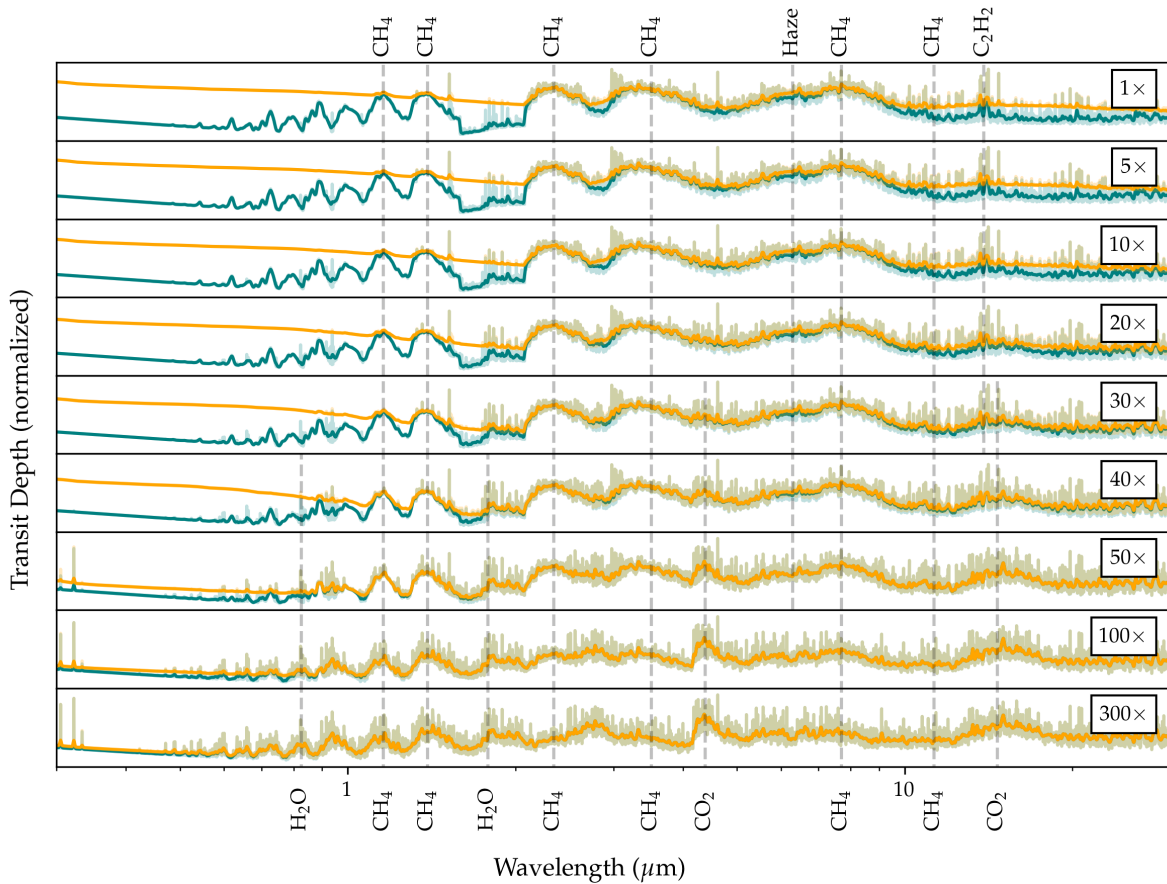


Figure 4.2: Changes in model transmission spectra for increasing enhancement of atmospheric oxygen by factors of 1-300 $\times$  from top to bottom. The full spectra (orange lines) are compared to “hazeless” spectra for which the opacity contribution of haze was removed from the calculation (teal lines), revealing the otherwise muted molecular features of the gas phase species. The transparent colored lines represent the full-resolution transmission spectra output by `Exo-Transmit` (spectral resolution of  $R = 1000$ ), while the opaque, thick lines are smoothed for ease of visualization. The baseline case (1 $\times$ ) corresponds to Figure 4.1. The bulk composition of the atmosphere changes with increasing oxidation, and new molecular features of  $\text{H}_2\text{O}$  and  $\text{CO}_2$  become apparent as their abundance increases. Haze dominates the transmission spectrum until oxygen has been added to the atmosphere at  $\sim 50\times$  its baseline value. At an oxygen enhancement of 300 $\times$ , the production of haze is effectively suppressed and its impact on the transmission spectrum is negligible. We note that the feature labelled as haze near  $7\ \mu\text{m}$  is a spectroscopic feature resulting a sharp rise in the extinction coefficient at that wavelength in the Haze model. This figure and caption is lightly edited from its version in Bergin et al. [13].

## 4.2 Modeling the Observable Atmosphere

To model the composition of the portion of the atmosphere that would be observable via spectroscopic techniques with JWST, we apply two different methodologies. The first is a chemical equilibrium calculation of atmospheric abundances as a function of atmospheric pressure. The second is a chemical kinetics calculation that includes photolysis reactions and photochemical production of important hydrocarbon haze precursors, and thus haze.

For the chemical equilibrium calculation, we start from the surface composition at the atmosphere-mantle boundary (Table 4.1), calculated as described in Bergin et al. [13]. We then derive the underlying *elemental* abundances (i.e.,  $\text{H}_2\text{O} \rightarrow 2 \text{H} + 1 \text{O}$ ) of H, C, N, O, S, and Ar. From these abundances, we re-derive thermochemical equilibrium as a function of temperature and pressure using the Gibbs free energy minimization techniques described in Mbarek & Kempton [130]. We perform our calculations over a pressure range of 1  $\mu\text{bar}$  – 100 bar and for temperatures from 300 K to 1200 K for a set of 69 molecules made up of H, C, N, O, and S (and Ar).

For the chemical kinetics modeling, we first must generate realistic temperature-pressure (T-P) profiles for the atmospheres in question. (This step is unnecessary for the chemical equilibrium modeling, described above, because in that case the chemical composition depends uniquely on the local temperature and pressure of the gas, rather than the full vertical T-P profile.) We use the open-source HELIOS<sup>2</sup> code [120, 122] to calculate temperature-pressure profiles in radiative convective equilibrium. We generate T-P profiles for the 3  $M_{\oplus}$  planet, which for reasons already discussed in the text is the scenario for which we believe our modeled atmospheres are

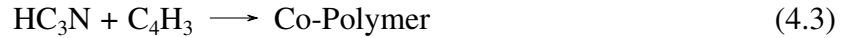
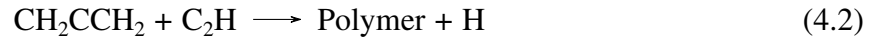
---

<sup>2</sup><https://github.com/exoclimate/HELIOS>

most representative of the evolved planets that will typically be observed with JWST. We model planets with equilibrium temperatures of 600, 900, and 1200 K (we focus on the 600 K model in the main text as these models best represent planets that would form within the soot line, and these planets reliably form appreciable haze), set by selecting the planet’s orbital semi-major axis assuming zero albedo and fully efficient day-night heat redistribution. The pressure at the bottom of the atmosphere is set to  $10^3$  bar. The host star properties and spectrum are selected to match the M-dwarf star GJ 876 ( $T_{eff} = 3300$  K,  $R_{\star} = 0.367R_{\odot}$ ) as representative of a typical system that would be observed with JWST.

The resulting HELIOS T-P profiles are then passed into a chemical kinetics code to calculate atmospheric abundances of gas-phase species and hydrocarbon haze as a function of altitude. As the impact of photodissociation is particularly pronounced at low pressures beyond the pressure cut-offs commonly used in radiative transfer models (here:  $10^{-7}$  bar), we extrapolate the HELIOS T-P profiles as isothermal to  $10^{-9}$  bar. We use the version of the `Atmos` photochemistry code described in Harman et al. [70], with the addition of carbon-bearing species and chemical reactions up to C-4 ( $C_3H_2$ ,  $C_3H_3$ ,  $C_3H_4$ ,  $C_4H_2$ ,  $C_4H_3$ ,  $C_4H_5$ ) and nitrogen-bearing species and reactions ( $N_2$ , N, NH,  $NH_2$ ,  $NH_3$ ,  $N_2H$ ,  $N_2H_2$ ,  $N_2H_3$ , CN, NCO, HCN, HNO, HNCO, NO,  $H_2CN$ ,  $HC_3N$ ,  $C_2H_3CN$ ,  $CH_2NH$ ,  $CH_2NH_2$ ,  $CH_3NH_2$ ,  $CH_2CN$ ,  $CH_3CN$ ) sourced from Tsai et al. [193]. We additionally account for the formation of organic haze using the fractal haze model from Arney et al. [7, 8], Wolf & Toon [209] adapted for an  $H_2$ -dominated atmosphere by including an updated reaction network based on a combination of the reaction networks used by Harman et al. [69], Venot et al. [197], and [146]. Haze formation is primarily initiated by  $CH_4$  photolysis, which catalyzes the formation of complex organic molecules in the atmosphere. Our chemical network cannot capture the full complexity of reactions occurring among all of these high-order hydrocar-

bon molecules. We instead follow a common practice of selecting lower-order haze “precursor” species from our chemical network that are formed high up in the atmosphere. For the current work we select polyacetylene ( $C_{2n}H_2$ ) [e.g. [4, 107, 208]] and allene ( $CH_2CCH_2$ ) polymerization [149] pathways, both proceeding through reactions with the ethynyl radical  $C_2H$ , and a nitrogen bearing co-polymer pathway based on cyanoacetylene  $HC_3N$  [101, 107] for haze production:



We assume a 100% conversion efficiency into haze. Once hazes form in the photochemistry model they scatter and absorb incoming UV photons, which ultimately self-regulates the formation of additional haze. Aerosol particles form as Mie scattering particles that grow and eventually coagulate into fractal aggregate particles composed of monomers of a fixed size of 50 nm. Haze optical properties for spherical and fractal aggregate particles were calculated with the mean field approximation model described in Rannou et al. [164] and Botet et al. [17] assuming Titan tholin complex refractive indices from Khare et al. [95]. The irradiating host star is again selected to be GJ 876, using its UV spectrum from the MUSCLES catalog [44, 46]<sup>3</sup>. We assume a uniform Eddy diffusion coefficient of  $K_{zz} = 6 \times 10^8 \text{ cm}^2 \text{ s}^{-1}$ , similar in range as previous studies [70, 89, 193]. While the choice of  $K_{zz}$  influences particle coagulation and atmospheric mixing, we forgo a detailed discussion and note that all atmospheric models we generated produced sig-

---

<sup>3</sup><https://archive.stsci.edu/prepds/muscles/>

nificant amounts of haze for the complete range of  $K_{zz}$  values we tested ( $5 \times 10^8 - 5 \times 10^{10}$   $\text{cm}^2 \text{s}^{-1}$ ). The atomic composition determined above in the chemical equilibrium modeling was scaled to preserve the relative abundance ratios while introducing a solar metallicity abundance of He, which `Atmos` uses as a (required) non-reactive filler gas. The planet’s gravity at the  $10^3$  bar level and radius were set to  $1481.86 \text{ cm s}^{-2}$  and  $1.41 R_{\oplus}$ , respectively.

Finally, we model the transmission spectra of the resulting atmospheres. For this we use the `Exo-Transmit` code [92], as modified in Teal et al. [186], to generate transmission spectra from the vertical abundance profiles output by the chemical kinetics code. Haze opacities are included in this version of `Exo-Transmit`, which depend on the haze particle radius. We use an identical set of hydrocarbon haze optical properties for all haze particles in the atmosphere, regardless of which of the three precursor formation pathways generated the haze. There is little evidence to suggest optical properties are identical between hazes formed via Equations 5.2, 5.3, 1.15, limited laboratory work exists for haze optical properties outside of Titan-like tholins formed under laboratory conditions. The best approximation currently applied by various studies is to treat haze particles as optically indistinct [7, 27, 186]. Laboratory characterization of hazes formed under a variety of conditions favoring specific pathways would be useful, but is difficult to implement due to the complex and diverse nature of individual particles formed in inhomogenous gases [27]. In Figure 4.1, we show versions of the transmission spectra with the haze opacity included and removed, emphasizing the impact of hazes on muting/obscuring spectral features.

Species	Type	Value	Species	Type	Value
O	Deposition velocity	0.1	O <sub>2</sub>	Deposition velocity	$1.0 \times 10^{-8}$
OH	Deposition velocity	0.1	H <sub>2</sub>	Fixed Mixing Ratio	0.852
HO <sub>2</sub>	Deposition velocity	$1.0 \times 10^{-2}$	CH <sub>4</sub>	Fixed Mixing Ratio	$4.19 \times 10^{-4}$
H <sub>2</sub> O <sub>2</sub>	Deposition velocity	$1.0 \times 10^{-2}$	NH <sub>3</sub>	Fixed Mixing Ratio	$1.181 \times 10^{-4}$
H <sub>2</sub> O	Fixed Mixing Ratio	$8.215 \times 10^{-4}$	O <sub>3</sub>	Deposition velocity	$1.0 \times 10^{-3}$
HNO <sub>3</sub>	Deposition velocity	$2.0 \times 10^{-1}$	C <sub>4</sub> H <sub>2</sub> (Aerosol)	Deposition Velocity	$1.0 \times 10^{-8}$
CH <sub>2</sub> CCH <sub>2</sub> C <sub>2</sub>	Deposition velocity	$1.0 \times 10^{-8}$	HC <sub>3</sub> N-C <sub>4</sub> H <sub>3</sub> co-polymer (Aerosol)	Deposition Velocity	$1.0 \times 10^{-8}$

Table 4.2: Static boundary conditions at the surface of our atmospheric model. Deposition velocity has units of cm/s. We note that this does not include top-of-atmosphere fluxes, such as downward fluxes of CO and O. These are parameterized in the model using abundances at the top of the atmosphere as described in Arney et al. [7] and Afrin Badhan et al. [1]. Our aerosols share a deposition velocity, though it also depends on sedimentation rate, which is a function of the particle radius (described in Section 1.3.4).

### 4.3 Discussion & Summary

This work posits that carbon species available from the protoplanetary nebula in the form of soots could enhance haze formation in exoplanet atmospheres. To do this, models were generated by collaborators that accounted for this increased carbon content in the context of planetary formation and used to inform boundary conditions and bulk atmospheric composition for our photochemistry and radiative transfer models. We found that models based on planets forming within a soot-bearing protoplanetary disk produce significantly more haze. In order to quench haze formation in such atmospheres, the atmosphere requires 50x as much oxygen as the baseline formation model contains (see Figure 4.2).

We find that our most productive haze pathway is the polyacetylene haze (Eq. 4.1), producing 99% of the haze shown in Figure 4.1. Our allene pathway (Eq. 4.2) and nitrile pathway (Eq. 4.3) for the remaining haze, or about 1% of the haze in Figure 4.1 and not significantly influencing the resultant transmission spectra. Even for highly oxidized atmospheres ( $> 100\times$  the oxygen content of our baseline models), we see no change in this behavior and the fractions of haze particles formed through each formation pathway are the same.

Such a soot line could be a mechanism for forming very hazy atmospheres close-in to the host star, and observing planets possibly formed through such a process will shed light on how warm and hot planets with high-altitude aerosols form and evolve. *JWST* is already observing sub-Neptune exoplanets, like the one we modelled in this study [57, 94]. It will be able to characterize the hazes themselves as well as methane features indicative of hydrocarbon aerosol formation.

## Chapter 5: Photochemical Haze Production in sub-Neptune Atmospheres

This work is work done as part of my dissertation work. I performed a deep investigation of a newly coupled `Atmos/HELIOS` 1-D atmospheric model capable of self-consistently modelling hazes in sub-Neptune atmospheres. This type of work, which has not been done self-consistently across a wide parameter space in the past, investigates the nature of haze production and observable impacts of haze across the known population of sub-Neptune planets. This work involved significant development efforts working on `Atmos`, `HELIOS`, and `Exo_Transmit`, which are outlined in Section 5.2.

### 5.1 Introduction

Previous work in this thesis has asserted the crucial role photochemical hazes play in characterizing exoplanet atmospheres; their dominating optical properties and complex formation pathways are essential for understanding atmospheric composition through transmission, emission, and reflection spectroscopy. While commonly regarded as a pesky optical barrier to probing molecular lines through various observational techniques, the presence or absence of a strong aerosol signal can provide insights into a number of atmospheric properties, such as metallicity, radiative processes, and habitability [27, 174].

In this study, we create an extensive grid of sub-Neptune atmospheres using well-established

atmospheric models. Sub-Neptunes are the most commonly occurring type of planet able to be readily accessed through transit spectroscopy. The atmospheres of these planets have revealed obfuscation of expected molecular features likely explained by the presence of high-altitude aerosols, with photochemically produced hazes being the leading explanation for the difficult-to-characterize, featureless transmission spectra [94, 102]. In doing so, we explore trends in haze formation and seek observable consequences for various stable atmospheres that arise in our model grid. This work builds on a steadily increasing body of literature and laboratory measurements to precisely characterize and comprehend hazes in familiar and alien environments.

The work presented here is still being prepared for publication, discussed in Section 5.4. Section 5.2.2 was primarily written by co-author Sandra Bastelberger, though it has been reformatted and heavily updated for this thesis. The remaining text, and all figures, have been generated specifically for this thesis.

### 5.1.1 Aerosols and Exoplanet Atmospheres

Characterizing aerosols is a rich field of study. Aerosols are strong scatterers compared to many gas-phase molecules, obscuring molecular spectral features leading to a “flat” transmission spectrum with muted molecular lines. However, determining the specific aerosol present in an observation, including fundamental properties like distinguishing between clouds, hazes, and other particulates, is challenging. Modelling and experimental efforts have considered a range of plausible scenarios for haze formation pathways [38, 40, 55]. Aerosols can be categorized into specific types based on whether they form via condensation, photolysis, thermochemistry, or other physical processes [54, 55]. Nonetheless, it has been demonstrated that small deviations

in environmental factors, such as formation conditions and the radiative environment of a planet, can have a significant impact on models involving different types of aerosols [27, 186].

Aerosols are found throughout the atmospheres of the Solar System and are thought to be common across exoplanetary atmospheres. From the tenuous photochemical hazes hovering above the surface of Pluto [62], to anthropogenic soots and smogs that interact with various processes on Earth [201], to the auroral hazes of Jupiter [211], the nature of aerosols is diverse. Aerosols are thought to be similarly ubiquitous across atmospheres of planets beyond the Solar System; the first detection of a “flat” spectrum attributable to aerosols in a planetary atmosphere was made by [179], and since then evidence of clouds has been found across a variety of exoplanets of different compositions and environs [28, 61, 102, 180]. With *JWST* operational, higher-resolution characterization of these exoplanets will provide further insights into the nature of their aerosols and enable atmospheric characterization of Earth- to Neptune-sized planets.

Photochemical hazes, with formation governed by the efficiency of photolysis reactions, are of particular interest for study due to their presence in solar system bodies and accessibility to *in-situ* and laboratory study. They are thought to be common in warm and cool exoplanets with effective temperatures  $T_{\text{eff}} \lesssim 800K$  and sufficiently high metallicity to form appreciable hydrocarbons [55], though experimental evidence of photochemical hazes forming at high temperatures exists [e.g., 40].

The formation pathways of hazes in exoplanet atmospheres are complex hydrocarbon reactions that are not well understood. Most modelling efforts extrapolate Solar System environments to exoplanet atmospheres, but most atmospheres favorable to characterization are physically distinct from any solar system body in their formation histories and orbital evolution. Laboratory studies such as Fleury et al. [38], Fleury et al. [40], Gavilan et al. [58, 59], He et al. [74], He et al.

[75, 77], Hörst et al. [80], and Moran et al. [138] have expanded our understanding of the nature of hazes in environments akin to exoplanet atmospheres, contributing significantly to modelling capabilities [55].

### 5.1.2 Sub-Neptune Atmospheres

Kreidberg et al. [102] found evidence of a high-altitude aerosol when they observed the “flat”/“featureless” transmission spectrum of GJ 1214 b—a planet categorized as a “sub-Neptune” exoplanet not represented by any solar system planets. Further characterization of super-Earth/sub-Neptune atmospheres is presently underway with *JWST*, already including further characterization of GJ 1214 b and its aerosols [57, 94]. Figure 5.1 illustrates *TESS* candidates with planned follow-up observations using *JWST* to characterize their atmospheres. Interpreting these observations requires forward modeling predictions to compare against. Although hazes are believed to be widespread in atmospheres, few forward models are capable of self-consistently modelling the chemical production and thermal feedback of photochemical hazes in exoplanet atmospheres. This type of self-consistent modelling is important for accuracy of atmospheric models and predicting observables [55, 182, 186], enabling more informed comparisons than models unable to capture thermal feedback effects.

Capturing such effects required coupling chemical and radiative transfer models to assess the steady-state chemical and thermal structure of an atmosphere. We describe the models used in this work—*Atmos*, *HELIOS*, and *Exo-Transmit*—in Section 5.2, which together self-consistently model the production and radiative properties of hydrocarbon photochemical hazes. Such a model has not been widely applied to the sub-Neptune mass/radius range before. In order to

predict trends in the diverse population of sub-Neptune-sized planets, we model a large grid with varying physical parameters to capture physical trends in haze production, and the observable consequences they would produce.

\* \* \*

In this study, we aim to create a comprehensive grid of self-consistent, haze forming, sub-Neptune atmospheric models by coupling `Atmos`, `HELIOS`, and `FastChem`. We also generate observational predictions using emission spectra generated by `HELIOS` and models from an updated version of the `Exo_Transmit` transmission spectrum model. Section 5.2 describes the model grid we execute, including how we couple `FastChem`, `HELIOS`, and `Atmos` atmospheric models and updates to `HELIOS`, `Atmos`, and `Exo_Transmit` made for this work. Section 5.3 presents a summary of the results of this study and outlines various trends we found across the modeled parameter space. We finally summarize our work and consider implications for future studies in Section 5.4.

## 5.2 Methods

### 5.2.1 Grid definitions and parameter space

We define a grid covering a wide parameter space shown in Table 5.1, spanning interesting targets for characterization by observatories like *JWST* and important unconstrained physical parameters such as eddy diffusion coefficient  $K_{zz}$ , metallicity  $Z$ , and C/O ratio. That considered, not all planet populations within this space are necessarily feasible to model on a fixed-altitude grid, and recognizing those limitations we focus on warm/hot sub-Neptune atmospheres with

$T_{\text{eq}}$ (K)	$g$ (m/s <sup>2</sup> )	$P_{\text{surf}}$ (bar)	$K_{zz}$	$Z$	C/O
400	5	1	$10^6$	1	0.1
500	10	10	$10^8$	10	0.6
600	25	100	$10^{10}$	100	1.2
800		1000		1000	
1000				10000	
1200					

Table 5.1: Parameter space for our model set. In total, this amounts to 3240 models completed in this work.

**Key:**  $T_{\text{eq}}$ - equilibrium temperature;  $g$  - surface gravity;  $P_{\text{surf}}$  - surface pressure;  $K_{zz}$  - eddy diffusion coefficient;  $Z$  - metallicity; C/O - carbon/oxygen ratio

sufficient surface gravity to maintain an appreciably dense atmosphere. In cases where our atmospheres do not converge due to unforeseen physical limitations, we reject those from our collection of “validated” models.

Specifically, we avoid high- $T_{\text{eq}}$  ( $\geq 1000$  K), low- $g$  ( $< 10$  m/s<sup>2</sup>), high- $P_{\text{surf}}$  atmospheres where the scale height of an H<sub>2</sub>/He-dominated atmosphere becomes physically unreasonable. There are several instances where specific combinations of model parameters result in similar behavior; we discuss these scenarios in Section 5.3 and highlight possible approaches to mitigate them moving forward in Section 5.4.1.

All of our models use a planet with a radius of  $2.7 R_{\oplus}$ , the radius of GJ 1214 b, and use the star GJ 176 as the host star. We use a MUSCLES stellar spectrum, shown in Figure 5.2, and scale it to match the appropriate  $T_{\text{eq}}$  for each model.  $T_{\text{eq}}$  can be calculated using the following equation:

$$T_{\text{eq}} = T_{\text{star}} \sqrt{\frac{R_{\text{star}}}{2a}} \quad (5.1)$$

where  $T_{\text{star}}$  and  $R_{\text{star}}$  are the temperature and radius of the host star, respectively, and  $a$  is the orbital distance of the planet. We assume an albedo of 0, consistent with a perfect blackbody. We

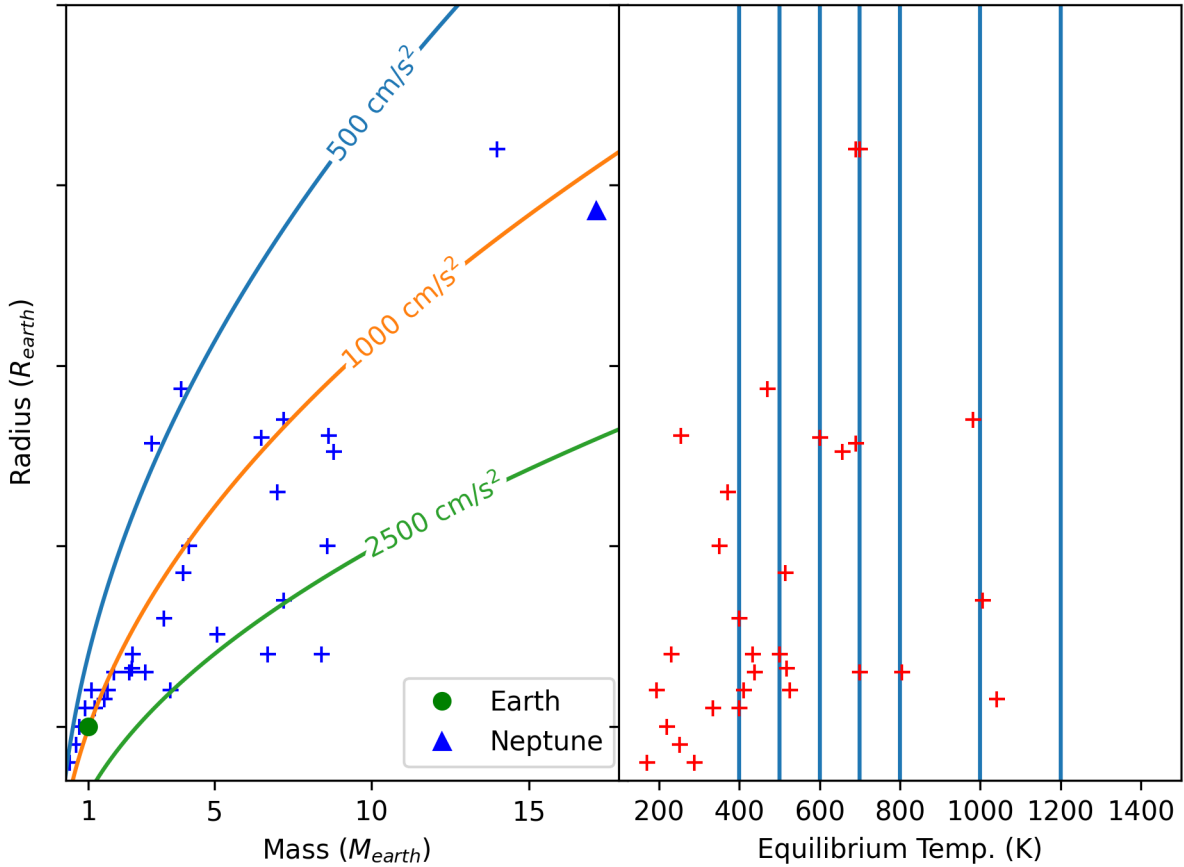


Figure 5.1: Plot of TESS objects with *JWST* follow-up characterization during Cycle 1, focusing on the sub-Neptune mass/radius regime of planets. Earth (green circle) and Neptune (blue triangle) are included for reference. Lines showing our choices of surface gravity (curves in plot (a)) and equilibrium temperature (lines in plot (b)) are included for reference. Data taken from TESS ACWG website (<https://tess.mit.edu/science/tess-acwg/#transiting-exoplanet-observations-jwst>).

also use this to determine  $a$  as an input to HELIOS as described in 5.2.3.

### 5.2.1.1 Host star properties

Planetary instillation is a critical input to both our photochemistry and radiative-convective models. Teal et al. [186] found that small changes to continuum or individual emission line fluxes at optical and UV wavelengths can result in significant changes to the chemical structure of an

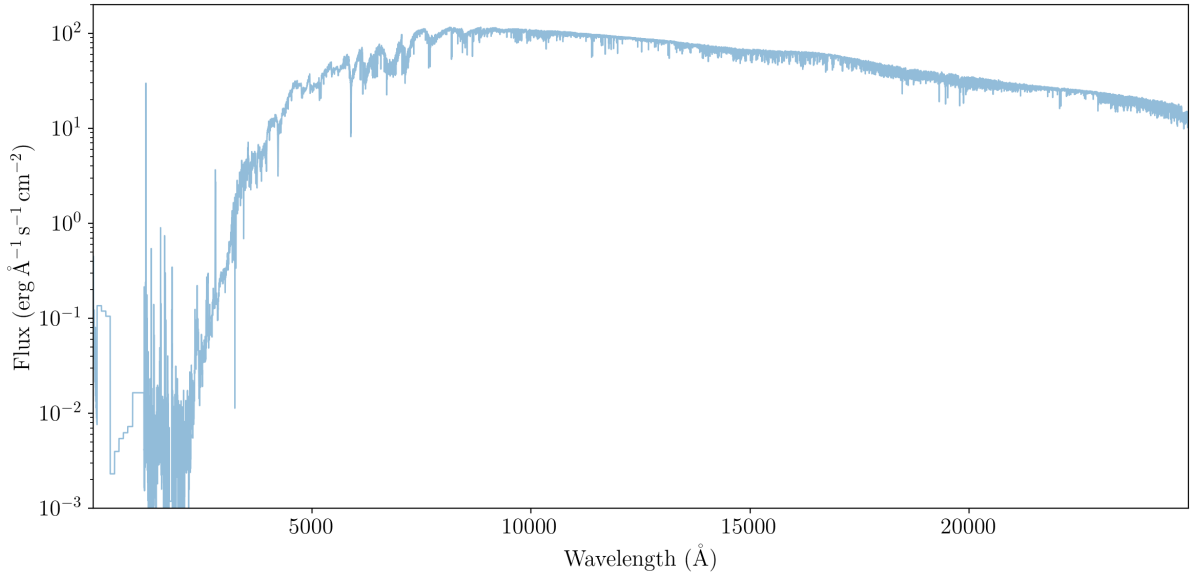


Figure 5.2: The panchromatic spectrum of GJ 176, which we use as input to our photochemical and radiative transfer models. This spectrum is taken from the MUSCLES catalogue, as described in 2.2.2.

Identifier	GJ 176
Type	M2.5 V
Temperature (K)	6667
Distance (pc)	9.456
Radius ( $R_{\oplus}$ )	0.474

Table 5.2: Physical parameters of the host star used in this work. Parameters taken from Marfil et al. [124]

atmosphere with observable consequences for atmospheres producing photochemical hazes. To this end, we select a well-studied input stellar spectrum as our primary host star, shown in Figure 5.2. We note that, for wavelengths  $> 2.5 \mu\text{m}$ , we extrapolate the spectrum flux using a blackbody of temperature 3667 K, consistent with GJ 176’s observed temperature [124].

### 5.2.2 Photochemical modeling

We use a version of the one-dimensional photochemistry model `Atmos` [7, 186] with the recent modifications for sub-Neptune atmospheres by Harman et al. [69], who use a custom C-

H-O photochemical network largely based on Tsai et al. [192]. Here, we expand their reaction network to incorporate nitrogen species, also based on Tsai et al. [192], and include aerosol production pathways discussed in the next subsection.

Our reaction network consists of 51 species and 651 reactions, of which 42 are photolysis reactions. This scheme comprises all species used by Kawashima & Ikoma [89], as well as all species in the reduced reaction scheme developed by Venot et al. [197] with the exception of HOCN. In contrast to this study, Venot et al. [197] chose to not include C<sub>2</sub>H<sub>2</sub> (acetylene) in their reduced scheme due to lack of observational evidence in atmospheres, and note that the absence of C<sub>2</sub>H<sub>2</sub> limits the validity of their reduced scheme to  $C/O < 1$  and temperatures below 1000 K. While we do not perform a completeness analysis, the inclusion of C<sub>2</sub>H<sub>2</sub> and other carbon-bearing species, as well as the work done by Venot et al. [197], suggest that the scheme used here is applicable to  $C/O \geq 1$  ratios and temperatures  $\geq 1000$  K.)

This model incorporated vertical transfer through eddy diffusion, quantified in our grid by the eddy diffusion coefficient  $K_{zz}$ . We keep this value constant throughout the atmosphere in our models.

### 5.2.2.1 Haze chemistry

Contrasting with the classical view of haze formation in a CH<sub>4</sub>-rich, temperate environment such as Titan's upper atmosphere, recent haze generation experiments for warmer H<sub>2</sub>-dominated atmospheres indicate that CH<sub>4</sub> does not constitute a necessary ingredient of the initial gas-mixture to enable the formation of haze. Fleury et al. [40] observed the formation of solid precipitate upon exposing a H<sub>2</sub>/CO gas mixture to Ly $\alpha$  radiation at 1500 K. Similarly, He et al. [76] measured haze

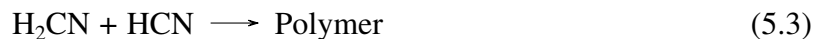
production in  $100\text{-}1000 \times$  solar metallicity  $\text{H}_2$ -rich gas mixtures without initial  $\text{CH}_4$  at 800 K. He et al. [75] identifies several potential haze precursors in the gas phase for cool exoplanet atmospheres such as acetylene  $\text{C}_2\text{H}_2$ , methanimine  $\text{CH}_2\text{NH}$  and hydrogen cyanide  $\text{HCN}$ . Despite extensive experimental evidence for oxygen incorporation in hazes [e.g., 38, 59, 137, 195] and suggestions of formaldehyde  $\text{HCHO}$  acting as a gas-phase precursor [e.g., 75], we do not explicitly consider this possibility as these chemical pathways are even less understood.

It is difficult to model the complex mixtures with high degree of speciation that lead to the formation of monomers. To that end, we assume cut-off reactions that lead to condensate formation without consideration of vapor pressure or specific polymerization pathways. The mechanism underlying the incorporation of nitrogen into hazes are not well understood. Various pathways for nitrogen bearing haze formation have been suggested in the literature [e.g., 208], such as pure nitrile pathways proceeding through CN-insertion. Co-polymerization of hydrocarbon and nitrile mixture forming aliphatic copolymers or aromatic copolymers is another possible production pathway.

We choose two haze formation pathways in this work: a pure hydrocarbon pathway and a nitrogenic pathway. For pure hydrocarbons, we use a pure polyynes pathway proceeding through the polymerization of acetylene ( $\text{C}_2\text{H}_2$ ).



Our nitrogen-bearing particles form via a pure nitrile pathway for which polymerization is achieved by CN-insertion.



Our model tracks the formation of these polymers independently, through we assume the same optical and microphysical properties for each type of haze. We assume that hazes form monomers with 100% efficiency with the rate of formation described by the reaction rates of the above governing reactions. These monomers then grow and eventually agglomerate into large, jagged particles with unique optical properties. The rate of growth and sedimentation of particles is determined by our treatment of haze microphysics.

### 5.2.2.2 Haze microphysics

The `Atmos` aerosol model schema was first developed for spherical particles in  $N_2$ -dominated atmospheres of rocky planets [85, 149] and has been updated by Wolf & Toon [209] to study the impact of fractal aggregate haze particles on Early Earth. Here, we briefly describe the `Atmos` aerosol microphysics scheme and the adjustments made to account for the properties of a  $H_2$ -dominated sub-Neptune atmosphere.

Aerosol particles are assumed to instantly attain their terminal fall velocity  $v_{\text{fall}}$  [158]:

$$v_{\text{fall}} = \frac{2\beta(\rho_p - \rho)gr^2}{9\eta}, \quad (5.4)$$

where  $r$  and  $\rho_p$  are the radius and density of the particle, respectively,  $\rho$  is density of the gas and  $g$  is gravitational acceleration acting on the particle and  $\eta$  is the dynamic viscosity of the surrounding gas. The Cunningham slip correction factor  $\beta$  for drag on small particles is calculated via

$$\beta = 1 + \text{Kn} (A + B \exp(-C/\text{Kn})) \quad (5.5)$$

We use values the values of  $A = 1.257$ ,  $B = 0.4$  and  $C = 1.1$  as suggested by Davies [29]. The Knudsen number  $\text{Kn}$  is given by:

$$\text{Kn} = \frac{\lambda}{r}, \quad (5.6)$$

where  $\lambda$  is the mean free path.

$$\lambda = \frac{k_B T}{\sqrt{2} \pi d^2 p} \quad (5.7)$$

Here,  $k_B$  is the Boltzmann constant,  $d$  is the diameter of the molecules the gas is composed of,  $p$  is the atmospheric pressure and  $T$  is the temperature. In the continuum regime, when  $\text{Kn} \ll 1$ , the Cunningham slip correction factor  $\approx 1$  and Equation 5.4 reduces to the Stokes settling velocity.

We follow Parmentier et al. [146] and the parameterization from Rosner & [169] in calculating the atmospheric dynamic viscosity  $\eta$  for hydrogen gas is given by

$$\eta = \frac{5}{16} \frac{\sqrt{\pi m k_B T} (k_B T / \epsilon)^{0.16}}{\pi d^2 1.22} \quad (5.8)$$

where  $m$  is the molecular mass,  $d$  is the diameter of the particle, and  $\epsilon$  is the Lennard-Jones potential well equal to  $59.7 k_B \text{ K}$

We forgo an explicit description of nucleation and gas-particle phase partitioning and assume that all hydrocarbon material is transformed into solid particles of initial size 1.3 nm after forming through either of our chemical reaction pathways (Equations 5.2 and 5.3). Particle growth then proceeds through coagulation when the coagulation timescale in a given atmospheric layer is shorter than the removal timescales through sedimentation eddy diffusion. Aerosol particles are treated as spherical Mie scatterers until they have grown to reach the monomer radius  $r_{\text{mon}}$  of 50 nm. Larger particles are assumed to be fractal aggregates of uniformly sized spherical

monomers with radius  $r_{\text{mon}}$ .

Note that our choice of  $r_{\text{mon}} = 50$  nm, a value often used for Titan-like tholins, is uncertain to translate directly to other atmospheric environs—aerosol particles produced in H<sub>2</sub>-rich gas mixtures range from 30-110 nm in mean monomer diameter and exhibit high variability with metallicity and temperature [74, 76, 80]. For aerosol particles that have grown larger than the monomer size, the equations discussed above are modified using a fractal radius,  $r_f$ , representing the aggregate optical nature of many haze monomers. Given a fractal aggregate particle consisting of  $n_{\text{mon}}$  monomers with a radius of  $r_{\text{mon}}$ ,  $r_f$  can be expressed with the relation [213]:

$$n_{\text{mon}} = \alpha \left( \frac{r_f}{r_{\text{mon}}} \right)^{D_f}. \quad (5.9)$$

Here,  $\alpha$  is a dimensionless constant set to 1 for this work, and  $d_f$  is the fractal dimension. The fractal dimension represents a measure of the compactness of the aggregate and can assume values between 1 and 3, corresponding to a linear chain of monomers and a compact spherical particle, respectively. The fractal dimension of Titan’s aggregate hazes is thought to be  $\sim 2$  based on geometric albedo [20, 105], and has been suggested to increase in Titan’s troposphere [190]. Restructuring of particles due to phenomena such as Brownian motion and aging processes leads to an increase of  $d_f$  as the particles grow [100]. We use the following the relation applied by Wolf & Toon [209] to describe how particles compact with increasing radius, with  $d_f$  reaching a maximum value of 2.4 as particles grow to be  $\sim 1$   $\mu\text{m}$ :

$$d_f = 2.4 - 0.9 \exp(-n_{\text{mon}}/500). \quad (5.10)$$

The optical properties of the spherical and fractal haze particles were calculated using the mean-field approximation code developed by Rannou et al. [163] and Botet et al. [17]. Sub-Neptune haze generation experiments suggest a strong dependency of haze refractive indices on the metallicity of the initial gas mixture and temperature [74]. However, due to a dearth of complex refractive index data covering the entire wavelength range, we adopt the refractive indices reported by Khare et al. [95] for tholins generated in an  $N_2/CH_4$  mixture.

Combined, the properties of haze particles and gas-phase molecules react to and determine the radiative environment throughout the atmosphere. To capture these feedback mechanisms and accurately model the thermal structure of our atmospheres, we couple our model to an updated version of the HELIOS radiative transfer model.

### 5.2.3 Radiative Transfer

We use the HELIOS GPU-accelerated radiative transfer model to solve for radiative equilibrium in our atmospheres [120, 121, 122]. The version of the code we use has been extended to account for aerosol particles of varying radius with unique optical properties, as described in Section 5.2.2.2. We also include the same haze cross sections used in Atmos [59, 95] for consistency between the two models.

HELIOS is a 1-D radiative-convective model that solves for radiative balance given a host star’s spectrum and the vertical abundance profiles for a planet’s atmosphere. A full description of the model can be found in Malik et al. [122]. We provide HELIOS with vertical profiles for the dominant gas-phase and aerosol species in our atmosphere calculated by either Atmos or FastChem, the host star’s spectrum, and appropriate planetary parameters for each of the grid

points in Table 5.1. Of interest to our work is the eclipse spectra and temperature profiles, which are used to couple the model with `Atmos`.

In order to account for the optical and thermal effects of haze particles in the atmosphere, we have updated `HELIOS` to accept haze particle mixing ratios and the same optical properties used by `Atmos`. Specifically, we take data for the absorption cross section, scattering cross section, and asymmetry parameter to calculate an effective cross section in the same way the most recent version of `HELIOS` (v3.0) treats clouds in the atmosphere.<sup>1</sup> We decouple I/O and interpolation relevant to hazes to a separate object to specifically manage `Atmos` file formats.

#### 5.2.4 Coupling `HELIOS` and `Atmos`

We couple these models by iterating between the two over several iterations for a set of cases spanning the parameter grid defined in Table 5.1 until the models does not appreciably change with subsequent iterations. To initialize these cases, we first run the `FastChem` equilibrium chemistry model—described in Stock et al. [183]—with an isothermal temperature-pressure profile set to the planet’s equilibrium temperature. This is used to generate a more realistic `HELIOS` TP profile. Once done, we run another equilibrium chemistry calculation to initialize `Atmos` before proceeding to iterate between `Atmos` and `HELIOS` 5-10 times, depending on convergence criteria. For most models, we determine convergence to be a fractional change of less than several Kelvin in our TP profiles and no appreciable change in mixing ratios, which we define as a change of less than  $10^{-25}$  throughout the atmosphere. For models that show signs of numerical instability—typically seen as discontinuity in vertical abundance or temperature profiles, or negative abundances—we loosen this requirement and manually iterate the model,

---

<sup>1</sup>See `HELIOS` release notes and documentation about this at <https://github.com/exoclimate/HELIOS>.

eventually trying to reach our standard convergence criterion.

For the remaining grid points, we initialize our models using previous converged solutions. We then perform iterations of HELIOS and Atmos to convergence to determine the change in haze abundance and production. Typically, this consists of 1-2 iterations, though cases requiring further computation times are allowed to iterate further. This reduces the convergence times for most models by 50%.

We consider a model “converged” when it has reached photochemical equilibrium, defined as negligible changes to the chemical state of the atmosphere over a coupled iteration. Models not meeting this criterion due to numerical instability are rejected and discussed in Section 5.3. HELIOS also has convergence criteria described in Malik et al. [122], and are similarly handled in cases where the model does not converge appropriately.

### 5.2.5 Transmission Spectra

We use a modified version of the Exo\_Transmit radiative transfer code, as described in Teal et al. [186] and Corrales et al. [27], to model transmission spectra for our grid. Our version of the code is publicly available on github.<sup>2</sup> This version uses the same opacity tables as previous versions of Exo\_Transmit [48, 49, 117], but includes newly generated haze cross sections as described in Section 5.2.2.2 to be consistent with the Atmos model.

This version of the model also accepts command line arguments for streamlined execution, especially useful for avoiding read/write races when executing a number of Exo\_Transmit models simultaneously.

---

<sup>2</sup>[https://github.com/teald/Exo\\_Transmit](https://github.com/teald/Exo_Transmit)

## 5.3 Results

### 5.3.1 Thermal structure and compositional variations for species of interest

The primary data product of this work is a set of 1-D atmospheric model outputs, of which the vertical distributions of molecular species and the temperature-pressure (TP) profiles are the most important.

Figure 5.3 contains a number of example profiles for each  $T_{\text{eq}}$  value in our grid. Although it is clear that the temperature-pressure (TP) profiles are universally warmer for higher  $T_{\text{eq}}$ , this only weakly correlates with whether haze will be present in the atmosphere or not, with many of our high- $T_{\text{eq}}$ , high- $Z$  models (Figure 5.4) producing appreciable haze.

Some of our lowest- $T_{\text{eq}}$  models and highest- $Z$  models produce sufficient haze to cool the surface by 400-600 K compared to the majority of models. These models tend to have higher mean molecular weights and an under-abundance of  $\text{H}_2\text{O}$  and  $\text{CO}_2$  in these models, shown in their respective panels in Figures 5.3 and 5.4, which is indicative of a reducing atmosphere able to produce appreciable amounts of haze.

$P_{\text{surf}}$  has an inverse relationship with high altitude haze formation, shown in Table 5.3, with lower surface pressures forming orders of magnitude more haze than higher-pressure counterparts. It is unclear if this is a selection effect—higher- $Z$  atmospheres are straightforward to converge for smaller atmospheres—, and further analysis is required to determine the exact mechanism driving this formation.

Although we do not plot them explicitly here, composition was not nearly as sensitive to our other grid parameters.  $g_{\text{surf}}$ , which partly determines the scale height of the atmosphere, do

not appreciably change the presence nor abundance of haze in the upper atmosphere, shown in Table 5.3.  $K_{zz}$  and C/O ratio do not independently cause significantly more haze to form, though coupled with high metallicities these can enhance production rates. Although Table 5.3 shows an increase in haze formation for our highest C/O ratio (1.2), these are dominated by high-metallicity ( $Z \geq 100$ ) models with a better convergence rate than low-metallicity models.

### 5.3.2 Sensitivity of hazes to planetary parameters

As described in Section 5.2.2.1 we consider two haze formation pathways. While our pure polyne pathway (Equation 5.2) shows sensitivity to the planet’s equilibrium temperature, our nitrile pathway (Equation 5.3) is more robust, forming appreciable hazes in our highest-temperature models provided  $C/O > 0.6$  and/or  $Z > 10$ . In the vast majority of models, our nitrile pathway is at least 2-3 times as productive as our pure hydrocarbon haze pathway. Table 5.3 quantifies average high-altitude haze column densities as a function of several grid parameters. These densities correspond to the amount of haze particles accessible to transmission spectroscopy, and serve as a uniform metric across planetary parameters.

Less massive atmospheres—represented in our model as atmospheres with lower surface pressures  $P_{\text{surf}}$ —produce several orders of magnitude more high-altitude pure-hydrocarbon haze compared to our larger atmospheres (as shown in Table 5.3), though nitrile haze production is constant across surface pressures. These atmosphere seem to retain more haze through a lower sedimentation rate (as described in Section 5.2.2.2).

We find that, for nitrile hazes, the formation of HCN and  $\text{H}_2\text{CN}$  through thermochemical reactions are sufficiently productive that these hazes are less sensitive to equilibrium temper-

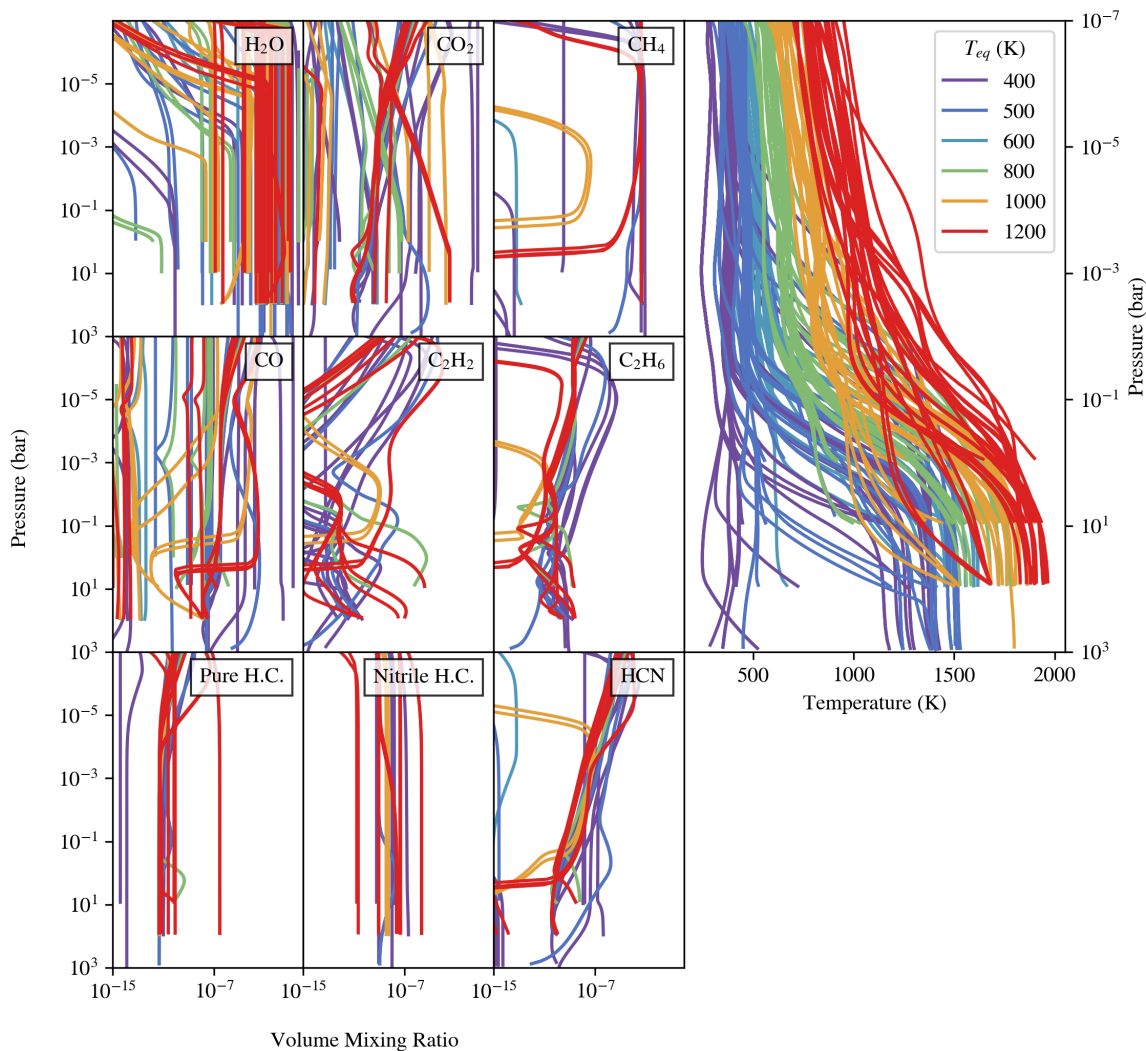


Figure 5.3: A representative selection of temperature and mixing ratio profiles from our model grid, colored based on the value of  $T_{eq}$  used for a given model. “H.C.” stands for hydrocarbon. Of the haze-producing models with mixing ratios greater than  $1e-15$ , our models form on-average  $10^{-4}$  ppm of our pure hydrocarbon hazes and  $10^{-1}$  ppm of our pure nitrile hazes throughout the atmospheres, including at altitudes probed by transmission spectroscopy.

atures. This can result in hydrocarbon-like hazes forming in conditions where, theoretically, pure-hydrocarbon hazes no longer form [55]. As for pure hydrocarbon hazes, further analysis is necessary to disentangle the mechanisms leading to its abundant formation in otherwise unfavor-

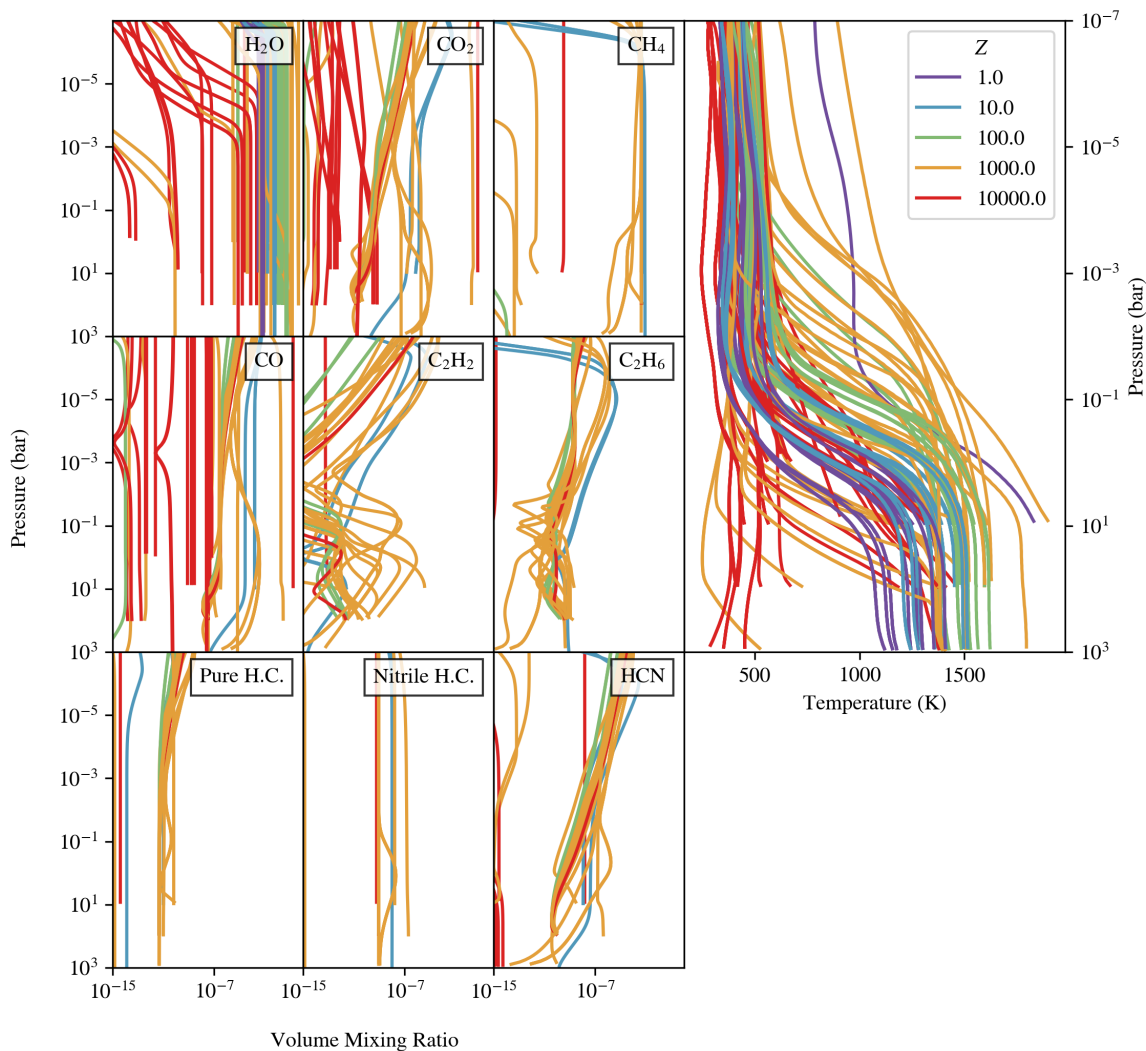


Figure 5.4: A representative selection of profiles from our model grid, colored based on their respective metallicities,  $Z$ .

able environments (see Section 5.4.1).

Atmospheric metallicity  $Z$  peaks in haze production at a  $Z$  of 100 in our grid, though there are significant outliers in each case due to other processes dominating haze formation and sedimentation efficiency. For example, larger values of  $g_{\text{surf}}$  are associated with less abundance high-altitude hazes, as sedimentation of particles is more efficient at depleting aerosol particles.

This, coupled with high- $P_{\text{surf}}$  and high- $T_{\text{eq}}$ , produce the least-hazy atmospheres across our model grid. Our models show no significant correlation between  $K_{zz}$  and haze production for either haze species.

### 5.3.3 Radical production and haze formation rates

Radical production plays a key role in haze formation, as the production rate of hydrocarbon species is directly enhanced by increased abundances of  $\text{CH}_3$  [217]. However, the role that other radicals play is less well understood for exoplanet atmospheres. The photodissociation of  $\text{CO}_2$  and  $\text{H}_2\text{O}$  into  $\text{CO/O}$  and  $\text{OH/H}$  free oxidizing radicals which could dampen or even act as a chemical sink for haze precursor molecules. To explore this relationship, we compare abundances and production rates of  $\text{H}_2\text{O}$ ,  $\text{CO}_2$ , and our two haze species.

We find that atmospheres with higher  $\text{H}_2\text{O}$  abundances have a weak correlation with haze formation rates, except in instances where thermochemistry dominates over photolysis in the formation of nitrile haze particles. Figures 5.5 and 5.6 compare the production rate of  $\text{H}_2\text{O}$  vs that of our polyne and nitrile hazes. Figure 5.6 highlights differences across our metallicities.

$\text{CO}_2$  abundance has a tighter correlation with haze production compared to  $\text{H}_2\text{O}$  for both of our hazes. However, rather than acting as a sink for C in our models, higher  $\text{CO}_2$  abundances are accompanied by significant abundance increases in both our haze species. This is especially evident in Figure 5.7, where the production rates of  $\text{CO}_2$  and each haze species are tightly correlated independent of the planet's C/O ratio.

We also consider the millibar column density for these species in Figures 5.8 and 5.9, which corresponds to the amount of haze in layers of the atmospheres accessible to transmission

spectroscopy. We find a tight, slight correlation between H<sub>2</sub>O column density and haze column density for both pure hydrocarbon and nitrile hazes in atmospheres where these hazes appreciably form. The relationship between CO<sub>2</sub> and hazes from this perspective is more complex; the correlation between CO<sub>2</sub> and our polyynes hazes has more spread for our lower-T atmospheres compared to H<sub>2</sub>O, and nitrile hazes at high temperatures show almost no correlation to CO<sub>2</sub> column density. In both cases, the warmest atmospheres produce the least amount of CO<sub>2</sub>, which may indicate some lower-boundary for CO<sub>2</sub> abundance if haze formation is actively occurring.

### 5.3.4 Trends in transmission and emission spectroscopy

Figure 5.10 shows emission spectra for each of our models grouped by equilibrium temperature. We find no significant observational signatures of haze in these emission spectra; instead, other factors dominate the features in individual spectra such as  $T_{\text{eq}}$  and  $Z$ , highlighted in Figure 5.11. Some high- $Z$ , high  $T_{\text{eq}}$  models exhibit a significant increase in flux at 7.1  $\mu\text{m}$ , which we believe to be a “window” in the opacities of CO<sub>2</sub> and H<sub>2</sub>O, respectively, which dominate the emission spectra at other wavelengths.

Figure 5.13 and 5.12 show similar plots for representative transmission spectra in our grid, grouped into equilibrium temperatures and compared to metallicity on our grid. We find that lower-metallicity atmospheres have less haze present in their model transmission spectra on average (save for our 400 K  $T_{\text{eq}}$  case), though models vary drastically in spectral morphology. Further detailed analysis of individual spectra will be necessary to make assertions about what causes this spread, and if there are specific mechanisms or combinations of grid parameters leading to haze forming at high altitudes or not (discussed in 5.4.1).

### 5.3.5 Numerically unstable regions of parameter space

Of our executed models, 24% experienced numerical instabilities leading to runs that never achieved our convergence criterion. Of this subset, about 400 of them represent physically implausible cases where the atmospheric scale height becomes very large. Specifically, the following regions of parameter space prove difficult to model on a fixed-altitude grid, ignoring other parameters:

- High- $T_{\text{eq}}$ , low- $g_{\text{surf}}$  atmospheres.
- Low- $P_{\text{surf}}$ , low- $g_{\text{surf}}$ , low- $Z$  atmospheres.

In both regions, the problem appears to be that the scale height of these low-mass atmospheres becomes unreasonable large. While this is less of a problem for fixed-pressure models like HELIOS and FastChem, it causes model failure for fixed-altitude models like Atmos, and so they are entirely excluded from this work. We discuss possible treatments and follow up diagnostics in Section 5.4.1.

## 5.4 Conclusions

In this work, we generate a large database of sub-Neptune atmospheric models with self-consistent haze chemistry, which has not been done prior to this work. In analyzing this grid, we find:

- Pure hydrocarbon hazes may form at high- $T_{\text{eq}}$  for metal-rich, high-C/O ratios, proving more robust than previous models have shown.

- Nitrile hazes offer a less temperature-dependent pathway for hydrocarbon haze formation compared to traditional Titan-like tholins.
- Our models display a “shut-off” in the abundance of aerosols, rather than a smooth transition from hazy to haze-less atmospheres.
- Emission spectra feature an emission “window” at  $7.1 \mu\text{m}$  for high-equilibrium temperature, high-metallicity atmospheres, but are otherwise do not vary drastically with haze production and are primarily determined by the equilibrium temperature of the planet.
- Transmission spectra can be generally grouped by metallicity in our models, with high-metallicity models reliably producing significant hazes that mute spectral features in transmission.
- Models with surface gravity less than  $10 \text{ m/s}^2$  and surface pressures greater than 10 bar are numerically unstable regions of our parameter space due to the large scale heights resulting in only the bottom-most layers of the atmosphere being captured by our photochemical models’ altitude grid.

### 5.4.1 Future Work

Although this work already displays unexpected trends in haze production rates in sub-Neptune atmospheres, there remains significant work to be done in analyzing and interpreting the completed model grid, and once that analysis is finished we plan to extend the grid to cover more host star types.

A significant part of our parameter space is inaccessible to the current model configuration.

While we believe this is due to nonphysical scenarios—specifically outlined in Section 5.3.5—further testing is needed to narrow down a more precise diagnosis for these failed model runs. We plan to target specific models that represent the current “boundary models” in the grid, and perturb the grid parameters to isolate what parameters are most sensitive to this region of parameter space.

Furthermore, we’ve highlighted surprising trends in pure hydrocarbon and nitrile haze formation that is contradictory to previous haze formation theory. While this preliminary analysis is exciting, such a result requires significant scrutiny to ensure that human or computational error is not skewing our results. To do this, we will streamline the current coupled-model API in preparation to run further grids with different host stars as described above, and rigorously test points of possible issue. For example, we have recently defined strict quality checks for output HELIOS and FastChem models, and are exploring adjusting the convergence criterion in Atmos, as well as re-implementing the HELIOS-Atmos pipeline to be a single interface rather than the present script-based solution.

In performing these updates, we expect to validate the database described in this work, provide an open-source coupling schema for Atmos and HELIOS, and expand the results described above to new environments for better coverage of JWST targets. While we expect some of the trends in this version of the grid to be consistent across host stars, the bulk properties of individual models, as well as regions of parameter space most amenable to haze formation, are likely to change significantly around a G2V or M8V star.

$T_{\text{eq}}$ (K)	$d_{\text{C}_2\text{H}_2}$ ( $\text{cm}^{-2}$ )	$d_{\text{H}_2\text{CN}}$ ( $\text{cm}^{-2}$ )
400.0	$3.0 \times 10^{18}$	$1.4 \times 10^{21}$
500.0	$4.3 \times 10^{21}$	$2.7 \times 10^{20}$
600.0	$6.0 \times 10^{11}$	$2.3 \times 10^{14}$
800.0	$7.7 \times 10^{13}$	$3.4 \times 10^{15}$
1000.0	$9.2 \times 10^{15}$	$1.1 \times 10^{17}$
1200.0	$1.5 \times 10^{17}$	$1.4 \times 10^{17}$
$P_{\text{surf}}$ (bar)		
1.0	$1.2 \times 10^{21}$	$1.3 \times 10^{19}$
10.0	$1.4 \times 10^{21}$	$1.6 \times 10^{20}$
100.0	$1.7 \times 10^{18}$	$3.1 \times 10^{20}$
1000.0	$1.9 \times 10^{17}$	$7.9 \times 10^{20}$
Z		
1.0	$6.5 \times 10^{14}$	$6.0 \times 10^{15}$
10.0	$3.3 \times 10^{15}$	$1.4 \times 10^{17}$
100.0	$2.9 \times 10^{21}$	$1.5 \times 10^{21}$
1000.0	$6.5 \times 10^{20}$	$7.1 \times 10^{18}$
10000.0	$8.5 \times 10^{15}$	$1.1 \times 10^{16}$
C/O ratio		
0.1	$3.3 \times 10^{16}$	$9.5 \times 10^{17}$
0.6	$5.7 \times 10^{15}$	$5.0 \times 10^{19}$
1.2	$2.1 \times 10^{21}$	$8.8 \times 10^{20}$
$g_{\text{surf}}$ ( $\text{m/s}^{-2}$ )		
5.0	$2.2 \times 10^{22}$	$8.8 \times 10^{21}$
10.0	$3.5 \times 10^{20}$	$2.0 \times 10^{20}$
25.0	$1.4 \times 10^{15}$	$1.9 \times 10^{14}$
$K_{zz}$ ( $\text{s}^{-1}$ )		
1000000.0	$1.3 \times 10^{21}$	$1.1 \times 10^{20}$
100000000.0	$5.2 \times 10^{18}$	$4.2 \times 10^{20}$
10000000000.0	$7.8 \times 10^{20}$	$3.9 \times 10^{20}$

Table 5.3: Average millibar column densities for each of our hazes with respect to individual grid parameters. The millibar column density  $d$  is the integrated number density from 1 mbar to the top of our atmospheric models (which is variable in pressure), representing a metric of haze's impact on transmission spectroscopy regardless of  $P_{\text{surf}}$ .

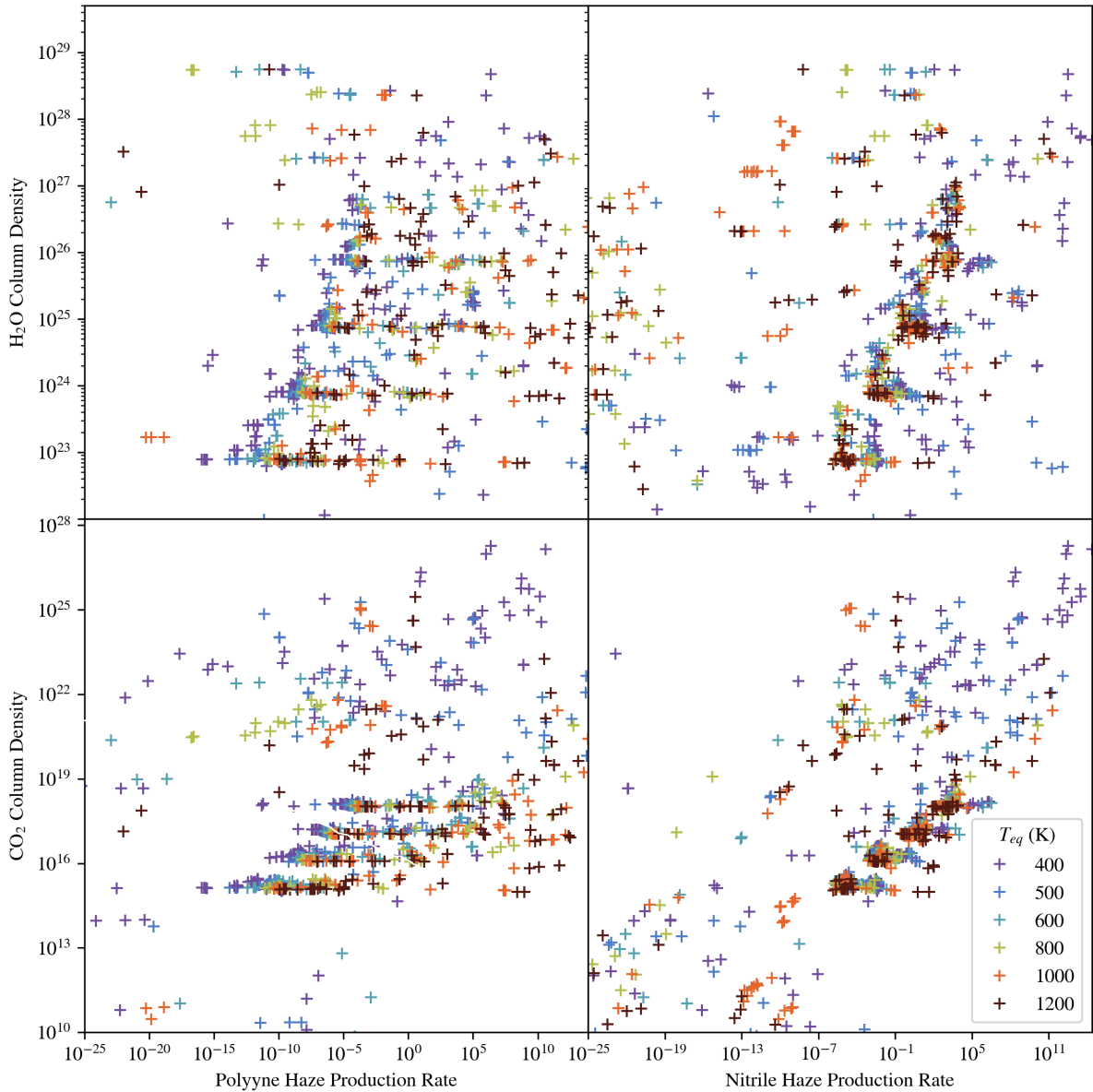


Figure 5.5: Plot of global haze production rate for each of the hazes in our model against the global  $\text{H}_2\text{O}$  and  $\text{CO}_2$  mixing ratios. The color of each point represent the equilibrium temperature  $T_{\text{eq}}$  for each model. **Note:** As these are not normalized column densities and production rates, there is a direct dependence on  $P_{\text{surf}}$  that manifests as “jumps” on this plot’s y-axis and clusters in the data at different global column densities.

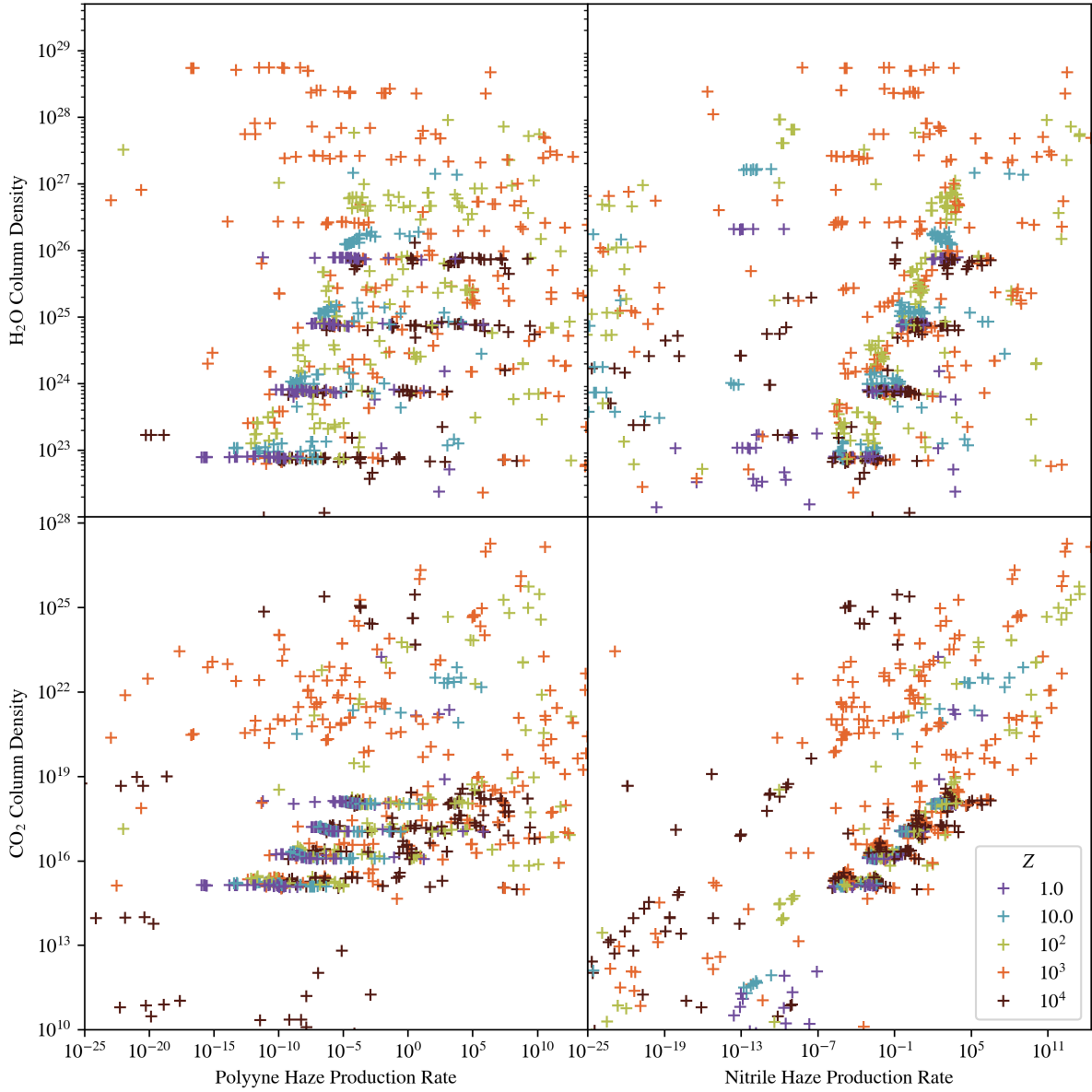


Figure 5.6: Plot of global haze production rate for each of the hazes in our model against the global H<sub>2</sub>O production rate. The color of each point represent the metallicity  $Z$  for each model. See note in Figure 5.5 about pressure clustering.

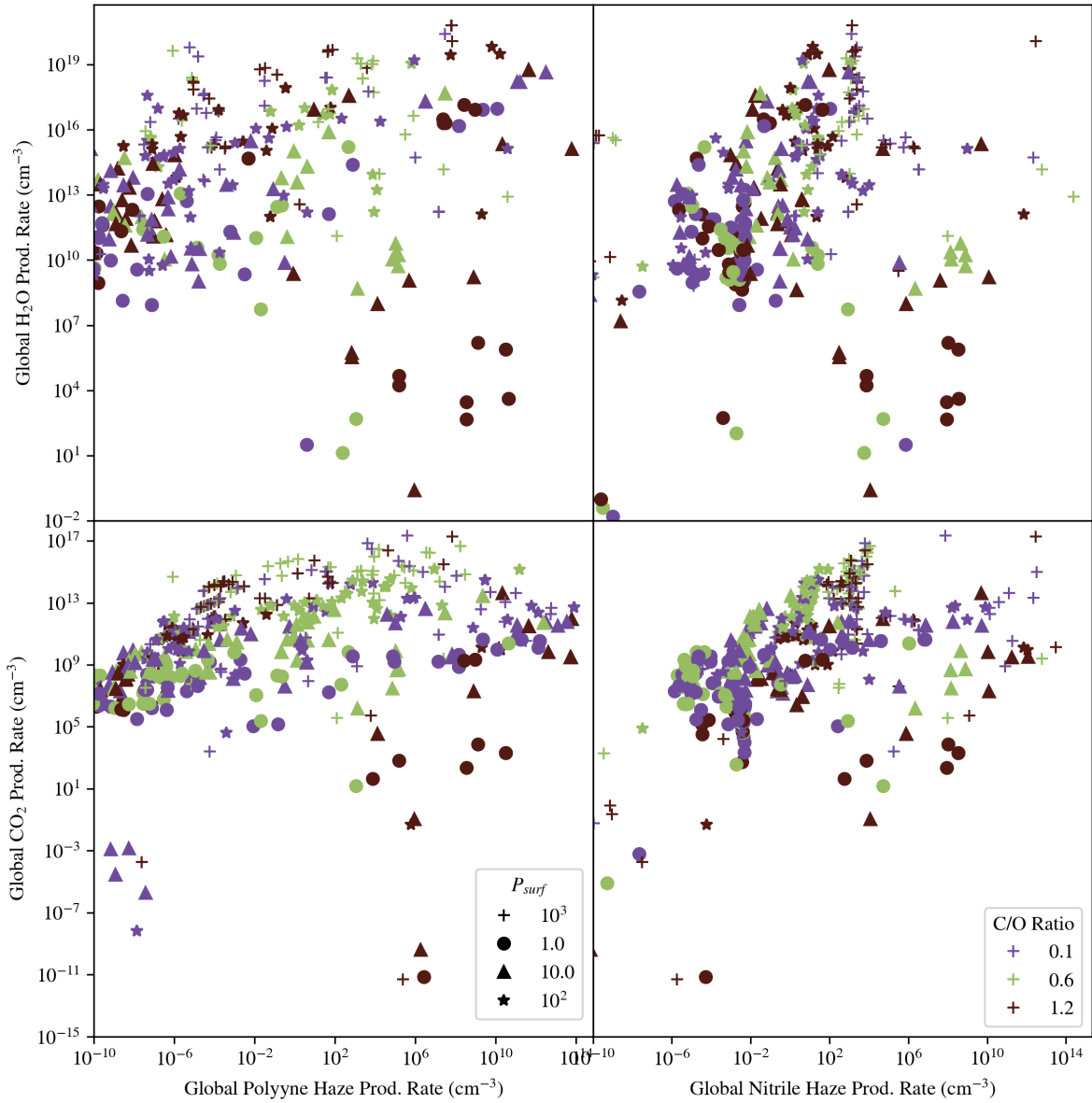


Figure 5.7: Plot of global haze production rate for each of the hazes in our model against the global H<sub>2</sub>O production rate. The color of each point represent the C/O ratio for each model

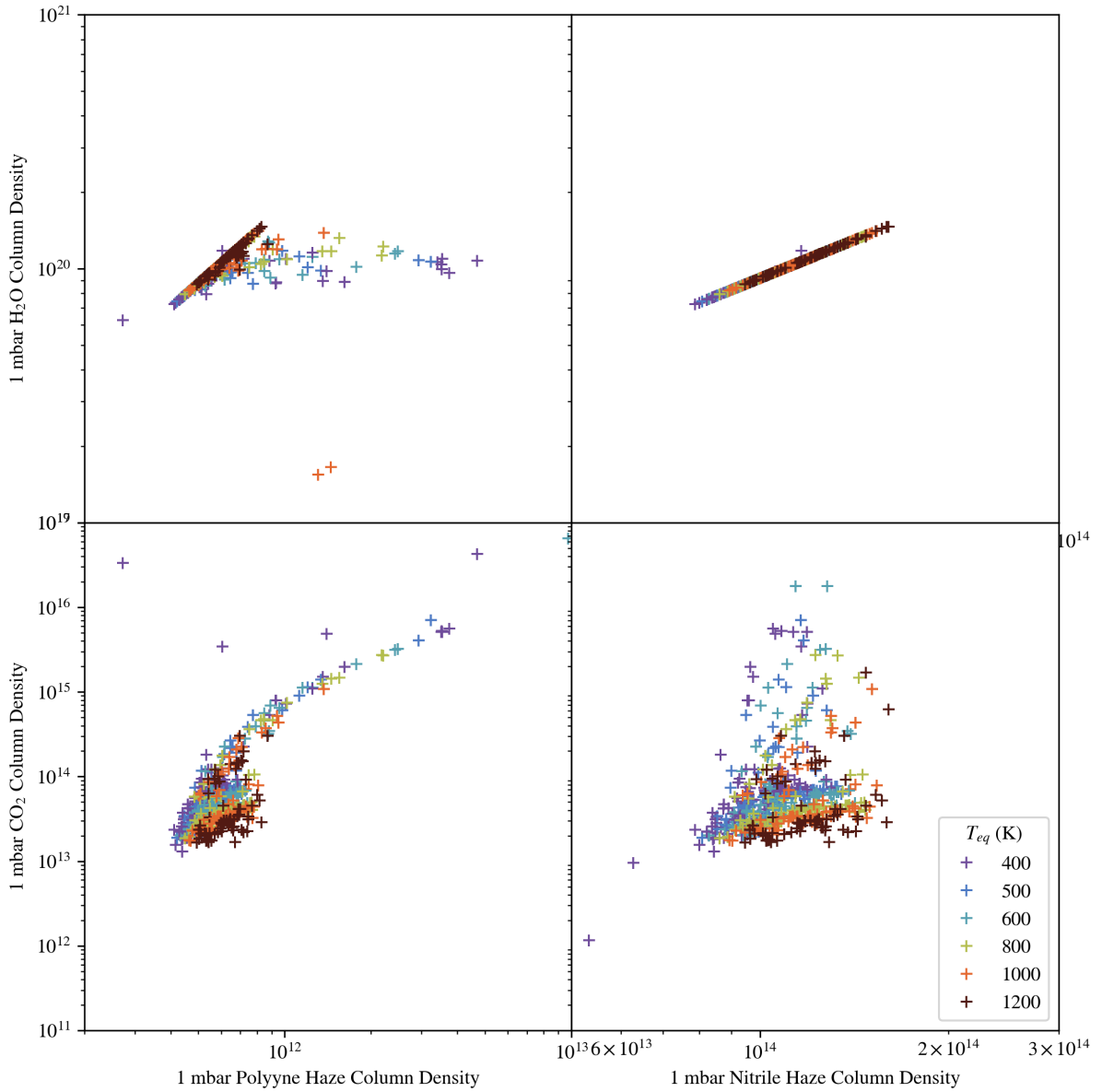


Figure 5.8:  $\text{H}_2\text{O}$  and  $\text{CO}_2$  column densities vs. haze column densities above 1 mbar, colored with respect to each model's value of  $T_{\text{eq}}$ . We note these models are specifically those producing appreciable haze—which we define here as sustaining a mixing ratio of  $10^{-12}$  or greater at some altitude in the atmosphere.

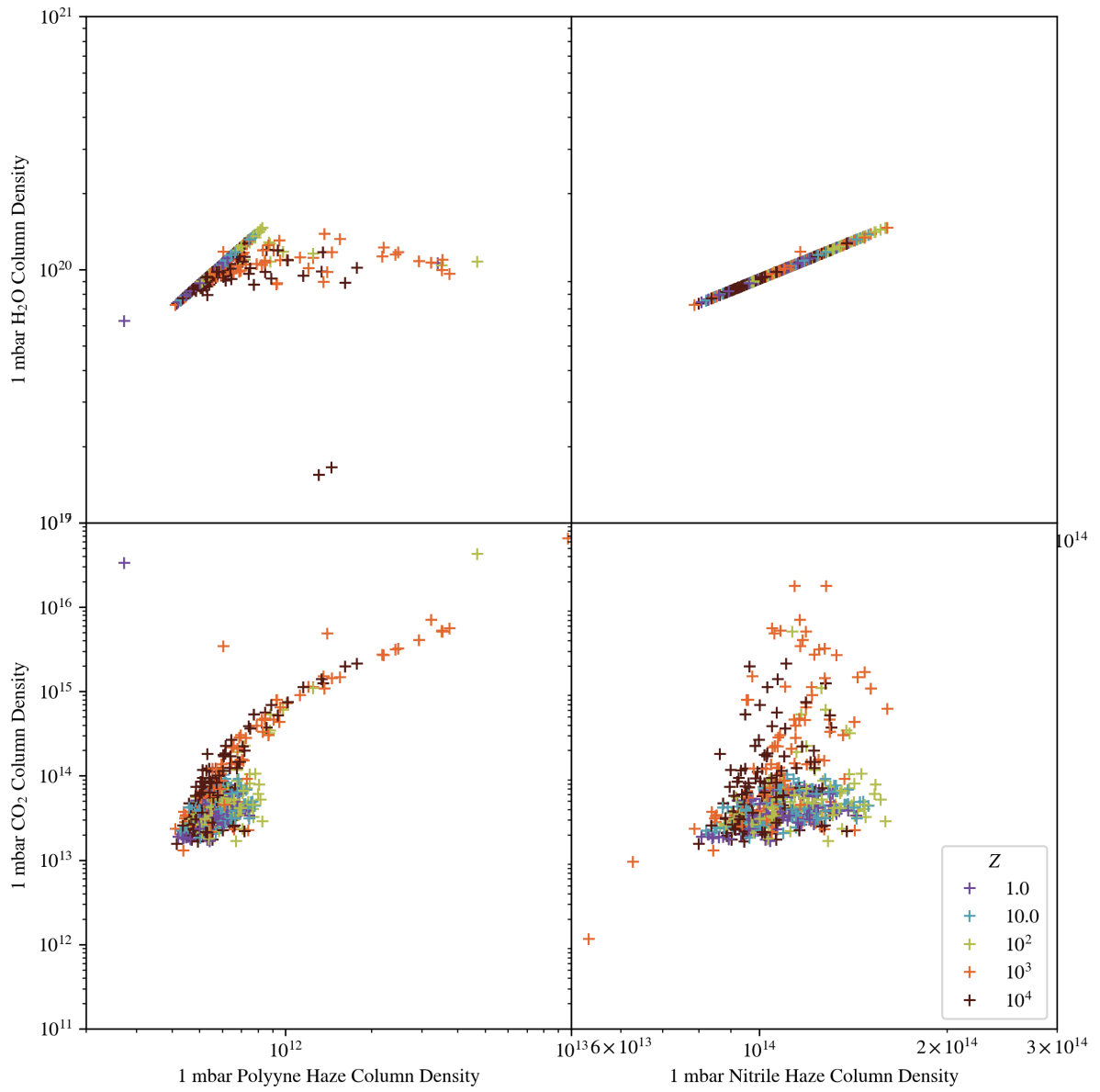


Figure 5.9: Same as Figure 5.8, but colored with respect to metallicity.

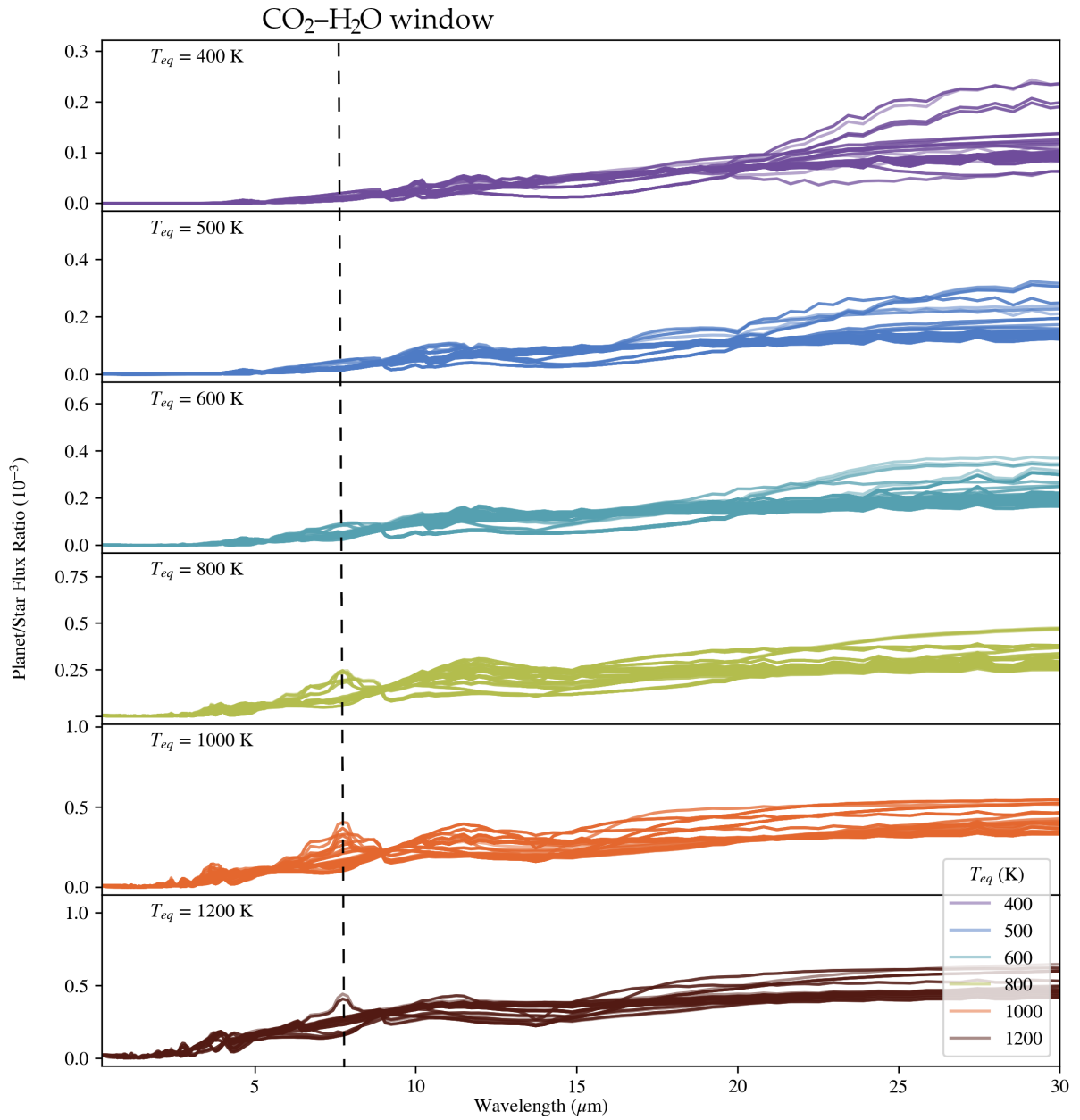


Figure 5.10: Model emission spectra for a selection of models on our grid, sorted by  $T_{eq}$ . Note: as the Planet/star flux ratio varies drastically as a function of equilibrium temperature, we scale the vertical axes independently to best highlight spectra features.

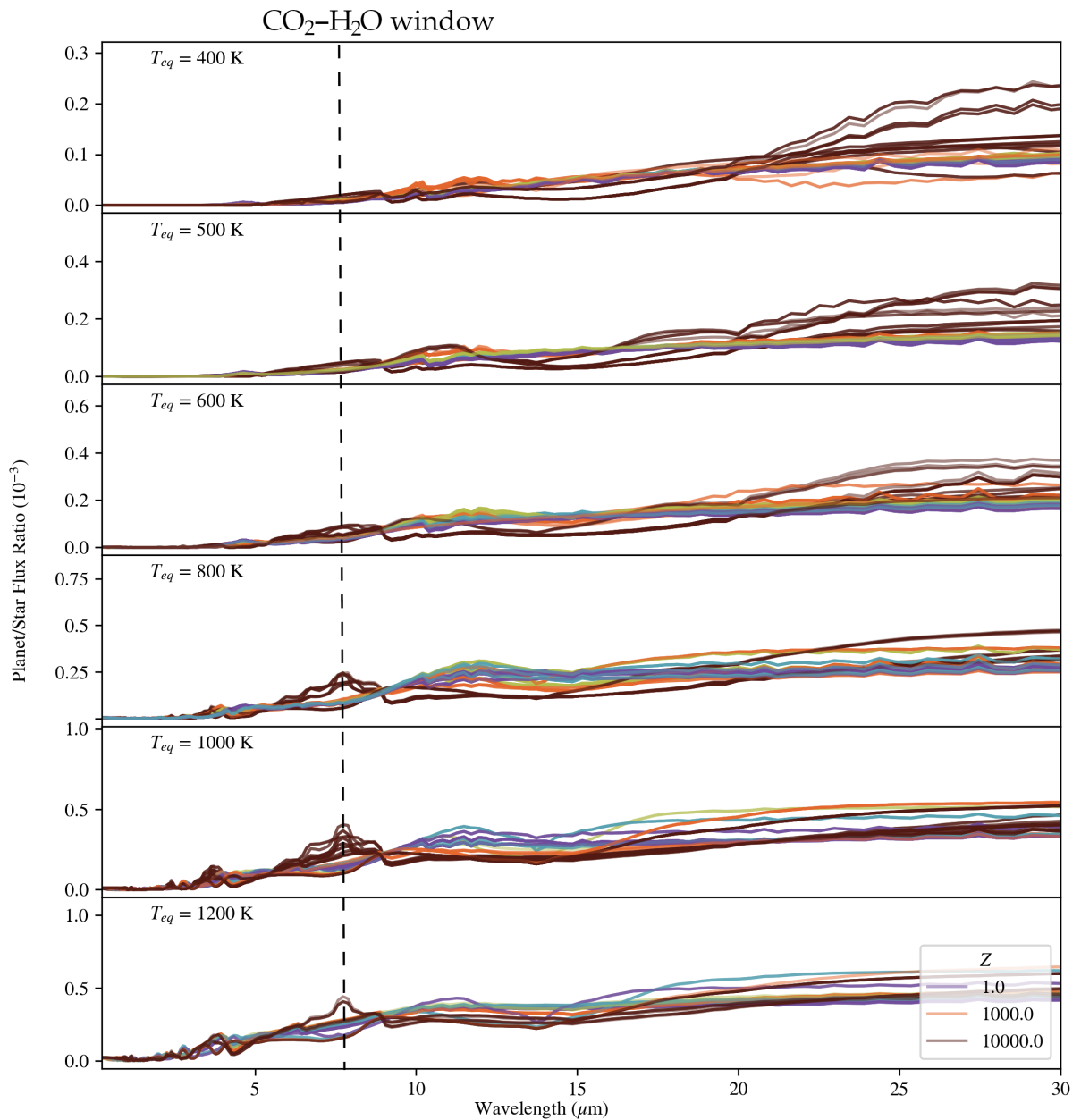


Figure 5.11: Model emission spectra for a selection of models on our grid, colored by their respective metallicities. Higher metallicity atmospheres universally produce more flux long-ward of 20 microns, and for our higher- $T_{\text{eq}}$  atmospheres have a peak in emission flux at  $7.1 \mu\text{m}$ . Lower- $Z$  atmospheres show a peak in flux at  $11 \mu\text{m}$  due to CO<sub>2</sub>.

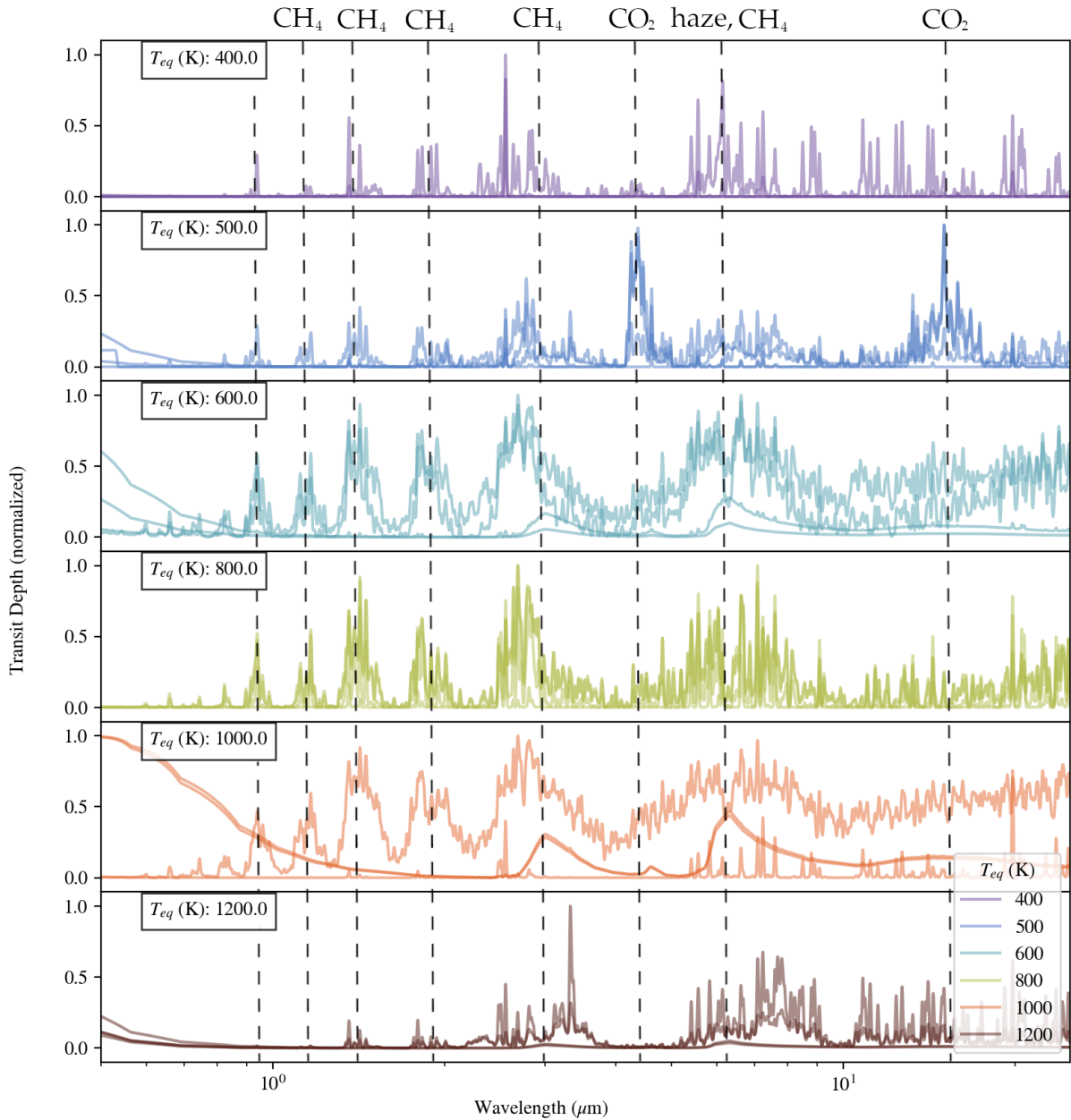


Figure 5.12: Representative model transmission spectra for models with metallicity  $Z > 100$ , grouped by their equilibrium temperatures. Although our lowest ( $T_{eq} < 600$  K) and highest ( $T_{eq} > 1000$  K) models display typical haze features, many warm planets show large molecular features largely unaffected by haze opacity. However, across all of our high- $Z$  models, there were significant outliers that produced a large amount of haze. These atmosphere also have large C/O ratios and consequently more carbon available to form hydrocarbon and nitrile hazes.

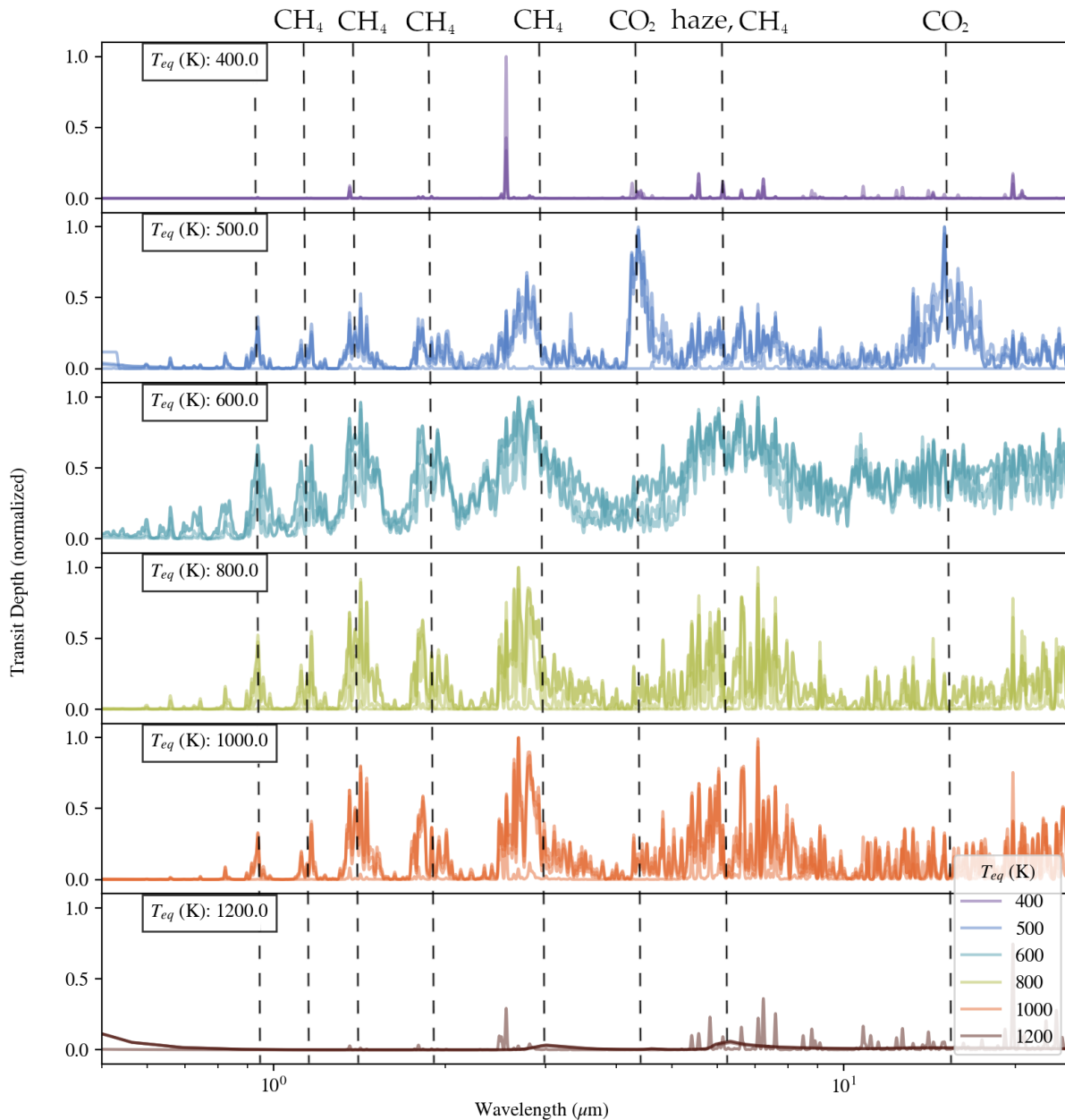


Figure 5.13: Representative model transmission spectra for models with metallicity  $Z \leq 100$ , grouped by their equilibrium temperatures. These transmission spectra show less overall spread in qualitative spectral shape; our highest- and lowest-temperature models have largely featureless transmission spectra, as these two regimes form significant amounts of haze in their atmospheres. Intermediate temperatures show strong molecular absorption features unaffected by haze, having no representative hazy atmosphere as seen for higher metallicity atmospheres in Figure 5.12.

## Chapter 6: Conclusion

In this thesis, I explored the ways in which photochemical models can be applied to pressing issues facing astronomers in the era of *JWST*. These range from our understanding of inputs to these atmospheric models, such as the spectral properties of the host star and assumptions about aerosol composition and chemistry in exoplanet atmospheres, to directly applying established models to make predictions about previously un-explored parameter spaces. The work described here is especially relevant to upcoming studies and observations.

### 6.1 Future Work

Chapter 5 is preliminary work; the full extent of the grid, described in Section 5.4.1, will include several host star types. There is also more analysis needing to be done to better understand the nature of haze formation in different regions of parameter space.

Although M-dwarfs like GJ 176 are abundant in the galaxy and favorable for observing exoplanets, Sun-like stars and other main sequence hosts are becoming more accessible to characterization using modern and next-generation observatories. This will expand our grid from its present state of 3,042 models to 12,168 in total, an unprecedented set of sub-Neptune atmospheric model data available to the public.

The immediate goals for this work are to re-validate the current model by factoring and

reviewing all intermediate steps in the coupling process. Likely, some parts of parameter space are unavailable to our models can be mitigated by changing the procedure in which the model iterates between HELIOS and Atmos. This method of converting between altitude and pressure grids is a relatively new one, and studying how well that process works, and how issues might be mitigated, will widen the parameter space accessible to this model. Since our problems primarily arise from the scale height of the atmosphere varying (see Section 5.3.5), adjusting the respective model grids dynamically could lead to faster convergence for models, as well.

We also introduce a nitrile formation pathway to the model, and more rigorous tests to understand exact mechanisms behind its formation in Atmos are underway. This involves characterizing the entire formation network of nitrile haze precursors HCN and H<sub>2</sub>CN in our model to determine what enables formation at higher temperatures than expected from previous theory. The (relative) lack of sensitivity to radical production rates and the equilibrium temperature of the planet suggest some unknown mechanism driving the production of this haze. While thermochemical production of HCN is a likely culprit, and we believe it plays a role in producing nitrile hazes where pure hydrocarbons may not form, we strive to fully characterize this behavior before publication.

The end goal of this work, an online database containing the entire grid of exoplanet atmospheres, is already designed and ready to implement, with a functional API. Once the above concerns and efforts are addressed, we plan to implement a web page for people to interact with the database, including downloading and interactively plotting the data with Django applications.

Tools like these will be useful as next generation telescopes continue making unprecedented observations and new observatories are deployed.

## 6.2 Upcoming studies and missions

The next several years will bring exciting new results and see the deployment of several observatories expanding our capacity to characterize exoplanet atmospheres. At present, *JWST* has already resulted in groundbreaking advances in characterization [e.g., 185, 194]. Studies have indicated the potential for hazes in a variety of atmospheres, highlighting the need for improved models of haze chemistry and microphysics. Photochemically produced  $\text{SO}_2$  was recently discovered in the atmosphere of the hot jupiter WASP-12b [194].

Next-generation ground based observatories have also produced exciting insights into the atmospheres of giant planets. The Very Large Telescope (*VLT*) found evidence of high-altitude haze formation in the atmosphere of WASP-74b [181]. Another *VLT* observation made with the ESPRESSO instrument constrained the water abundance and cloud-top pressure of the atmosphere of the hot Neptune planet WASP-166b [104]. The work in this dissertation applies directly to characterizing the nature of these aerosols, especially their possible formation mechanisms and predictions for what observations could narrow down bulk aerosol properties notoriously difficult to disentangle. Next generation 30-meter class telescopes, or *ELTs*, will enable characterization of smaller, cooler exoplanets as modelled throughout this work. Understanding the nature of these types of exoplanet atmospheres is a critical part of selecting optimal targets for characterization, and interpreting the results of future spectroscopic characterization efforts.

### 6.3 Summary

In this dissertation, I cover work I performed as part of several collaborations to better understand the nature of planetary atmospheres through modelling. In summary:

- I extensively studied how our understanding of the host star’s UV spectrum can impact our ability to model exoplanet atmospheres with and without aerosols, highlighting the implications for models aiming to make predictions about observable quantities. That study found that careful considerations about how to account for an un-characterized host star is critical for atmospheres with photochemical hazes, justifying further surveys of M-dwarf exoplanet hosts to better characterize their UV spectra.
- I then took the methods discussed in that paper and applied them to two newly-characterized stars, LHS 3844 and AU Mic, modelling planets with atmospheres around them during quiescence and flaring to contrast the radiative environments during and outside of activity.
- I modelled atmospheres and transmission spectra for a set of boundary conditions informed by geochemistry and planetary formation, probing possible connections between planets forming outside a “soot” line in a protoplanetary nebula and hydrocarbon aerosol formation in the early atmospheres of these planets.
- I produced a novel grid of model sub-Neptune atmospheres using `FastChem`, `Atmos`, and `HELIOS`, self-consistently modelling hydrocarbon and nitrile hazes over a wide parameter space of particular interest to *JWST* characterization. I found surprising trends in haze formation contradictory to previous theory; hazes forming in hot, low- $Z$ , and low-C/O atmospheres where previous work has predicted they would be less favorable to form.

This work builds upon a field growing at an incredible rate. Novel studies are planned and underway that will fundamentally change our perspective of planetary atmospheres. Whether these investigations affirm or challenge current theoretical frameworks remains to be revealed. Nevertheless, it is evident that numerical modeling will assume a pivotal role in comprehending this unexplored realm of signal-to-noise and resolution. The findings of this dissertation elucidate the profound significance of forward modeling as an observational tool and provide insights into the prerequisites for effectively harnessing model capabilities. As we anticipate the emergence of next-generation observatories, work such as this will forge a path towards a precise comprehension of exoplanets in coming decade, setting the stage for exciting, novel discoveries in exoplanet science.

## Appendix A: Facilities and Software used in this Thesis

1. `Atmos`, see Sections 2.2.1 and 5.2
2. `HELIOS`, see Section 5.2.3
3. `Exo-Transmit`, see Section 2.2.3
4. `FastChem` [183]
5. `porchlight`
6. `matplotlib` [83]
7. `astropy` [9, 10]
8. `numpy` [71]
9. `scipy` [200]
10. `spectres` [21]
11. `pandas` [145, 204]

## Bibliography

- [1] Afrin Badhan, M., Wolf, E. T., Kopparapu, R. K., et al. 2019, arXiv e-prints, arXiv:1902.04086. <https://arxiv.org/abs/1902.04086>
- [2] Alexander, C. M. O. D., Howard, K. T., Bowden, R., & Fogel, M. L. 2013, *GeoCoA*, 123, 244, doi: [10.1016/j.gca.2013.05.019](https://doi.org/10.1016/j.gca.2013.05.019)
- [3] Alexander, R. 2012, *ApJL*, 757, L29, doi: [10.1088/2041-8205/757/2/L29](https://doi.org/10.1088/2041-8205/757/2/L29)
- [4] Allen, M., Yung, Y. L., & Pinto, J. P. 1980, *ApJL*, 242, L125, doi: [10.1086/183416](https://doi.org/10.1086/183416)
- [5] Ardila, D. R., Shkolnik, E., Scowen, P., et al. 2018, arXiv e-prints, arXiv:1808.09954. <https://arxiv.org/abs/1808.09954>
- [6] Arney, G., Domagal-Goldman, S. D., & Meadows, V. S. 2018, *Astrobiology*, 18, 311, doi: [10.1089/ast.2017.1666](https://doi.org/10.1089/ast.2017.1666)
- [7] Arney, G., Domagal-Goldman, S. D., Meadows, V. S., et al. 2016, *Astrobiology*, 16, 873, doi: [10.1089/ast.2015.1422](https://doi.org/10.1089/ast.2015.1422)
- [8] Arney, G. N., Meadows, V. S., Domagal-Goldman, S. D., et al. 2017, *ApJ*, 836, 49, doi: [10.3847/1538-4357/836/1/49](https://doi.org/10.3847/1538-4357/836/1/49)
- [9] Astropy Collaboration, Robitaille, T. P., Tollerud, E. J., et al. 2013, *A&A*, 558, A33, doi: [10.1051/0004-6361/201322068](https://doi.org/10.1051/0004-6361/201322068)
- [10] Astropy Collaboration, Price-Whelan, A. M., Sipőcz, B. M., et al. 2018, *AJ*, 156, 123, doi: [10.3847/1538-3881/aabc4f](https://doi.org/10.3847/1538-3881/aabc4f)
- [11] Ayres, T. R. 1979, *ApJ*, 228, 509, doi: [10.1086/156873](https://doi.org/10.1086/156873)
- [12] Bergin, E. A., Blake, G. A., Ciesla, F., Hirschmann, M. M., & Li, J. 2015, *Proceedings of the National Academy of Science*, 112, 8965, doi: [10.1073/pnas.1500954112](https://doi.org/10.1073/pnas.1500954112)
- [13] Bergin, E. A., Kempton, E. M. R., Hirschmann, M., et al. 2023, *ApJL*, 949, L17, doi: [10.3847/2041-8213/acd377](https://doi.org/10.3847/2041-8213/acd377)
- [14] Berta-Thompson, Z. 2017, *The M Dwarf UV Spectra Irradiating Nearby Transiting Terrestrial Planets*, HST Proposal
- [15] Berta-Thompson, Z. K., Bourrier, V., Charbonneau, D., et al. 2015, *Hydrogen Escape from an Earth-size Exoplanet: a Reconnaissance Study*, HST Proposal

- [16] Borucki, W. J., Koch, D., Basri, G., et al. 2010, *Science*, 327, 977, doi: [10.1126/science.1185402](https://doi.org/10.1126/science.1185402)
- [17] Botet, R., Rannou, P., & Cabane, M. 1997, *Appl. Opt.*, 36, 8791, doi: [10.1364/AO.36.008791](https://doi.org/10.1364/AO.36.008791)
- [18] Bourrier, V., Lecavelier des Etangs, A., Ehrenreich, D., et al. 2018, *A&A*, 620, A147, doi: [10.1051/0004-6361/201833675](https://doi.org/10.1051/0004-6361/201833675)
- [19] Burkholder, J., Sander, S., Abbatt, J., et al. 2019, *Chemical Kinetics and Photochemical Data for Use in Atmospheric Studies; Evaluation No. 19*. <http://jpldataeval.jpl.nasa.gov>
- [20] Cabane, M., Rannou, P., Chassefière, E., & Israel, G. 1993, *Planetary and Space Science*, 41, 257, doi: [https://doi.org/10.1016/0032-0633\(93\)90021-S](https://doi.org/10.1016/0032-0633(93)90021-S)
- [21] Carnall, A. C. 2017, arXiv e-prints, arXiv:1705.05165. <https://arxiv.org/abs/1705.05165>
- [22] Charbonneau, D., Brown, T. M., Noyes, R. W., & Gilliland, R. L. 2002, *ApJ*, 568, 377, doi: [10.1086/338770](https://doi.org/10.1086/338770)
- [23] Chen, H., Zhan, Z., Youngblood, A., et al. 2021, *Nature Astronomy*, 5, 298, doi: [10.1038/s41550-020-01264-1](https://doi.org/10.1038/s41550-020-01264-1)
- [24] Chen, J., & Kipping, D. 2017, *ApJ*, 834, 17, doi: [10.3847/1538-4357/834/1/17](https://doi.org/10.3847/1538-4357/834/1/17)
- [25] Christiansen, J. L. 2022, *Nature Astronomy*, 6, 516, doi: [10.1038/s41550-022-01661-8](https://doi.org/10.1038/s41550-022-01661-8)
- [26] Claire, M. W., Sheets, J., Cohen, M., et al. 2012, *ApJ*, 757, 95, doi: [10.1088/0004-637X/757/1/95](https://doi.org/10.1088/0004-637X/757/1/95)
- [27] Corrales, L., Gavilan, L., Teal, D. J., & Kempton, E. M. R. 2023, *ApJL*, 943, L26, doi: [10.3847/2041-8213/acaf86](https://doi.org/10.3847/2041-8213/acaf86)
- [28] Crossfield, I. J. M., Barman, T., Hansen, B. M. S., & Howard, A. W. 2013, *A&A*, 559, A33, doi: [10.1051/0004-6361/201322278](https://doi.org/10.1051/0004-6361/201322278)
- [29] Davies, C. N. 1945, *Proceedings of the Physical Society*, 57, 259, doi: [10.1088/0959-5309/57/4/301](https://doi.org/10.1088/0959-5309/57/4/301)
- [30] Deming, D., Seager, S., Winn, J., et al. 2009, *PASP*, 121, 952, doi: [10.1086/605913](https://doi.org/10.1086/605913)
- [31] Diamond-Lowe, H., Charbonneau, D., Malik, M., Kempton, E. M.-R., & Beletsky, Y. 2020, *The Astronomical Journal*, 160, 188, doi: [10.3847/1538-3881/abaf4f](https://doi.org/10.3847/1538-3881/abaf4f)
- [32] Diamond-Lowe, H., Youngblood, A., Charbonneau, D., et al. 2021, *AJ*, 162, 10, doi: [10.3847/1538-3881/abfa1c](https://doi.org/10.3847/1538-3881/abfa1c)

- [33] —. 2021, *AJ*, 162, 10, doi: [10.3847/1538-3881/abfa1c](https://doi.org/10.3847/1538-3881/abfa1c)
- [34] Duvvuri, G. M., Sebastian Pineda, J., Berta-Thompson, Z. K., et al. 2021, *ApJ*, 913, 40, doi: [10.3847/1538-4357/abeaaf](https://doi.org/10.3847/1538-4357/abeaaf)
- [35] Fauchez, T. J., Turbet, M., Villanueva, G. L., et al. 2019, *ApJ*, 887, 194, doi: [10.3847/1538-4357/ab5862](https://doi.org/10.3847/1538-4357/ab5862)
- [36] Feinstein, A. D., France, K., Youngblood, A., et al. 2022, *AJ*, 164, 110, doi: [10.3847/1538-3881/ac8107](https://doi.org/10.3847/1538-3881/ac8107)
- [37] Fleming, B. T., France, K., Nell, N., et al. 2018, *Journal of Astronomical Telescopes, Instruments, and Systems*, 4, 014004, doi: [10.1117/1.JATIS.4.1.014004](https://doi.org/10.1117/1.JATIS.4.1.014004)
- [38] Fleury, B., Carrasco, N., Millan, M., Vettier, L., & Szopa, C. 2017, *Earth and Planetary Science Letters*, 479, 34, doi: <https://doi.org/10.1016/j.epsl.2017.09.026>
- [39] Fleury, B., Gudipati, M. S., Couturier-Tamburelli, I., & Carrasco, N. 2019, *Icarus*, 321, 358, doi: [10.1016/j.icarus.2018.11.030](https://doi.org/10.1016/j.icarus.2018.11.030)
- [40] Fleury, B., Gudipati, M. S., Henderson, B. L., & Swain, M. 2019, *ApJ*, 871, 158, doi: [10.3847/1538-4357/aaf79f](https://doi.org/10.3847/1538-4357/aaf79f)
- [41] Fontenla, J. M., Linsky, J. L., Witbrod, J., et al. 2016, *ApJ*, 830, 154, doi: [10.3847/0004-637X/830/2/154](https://doi.org/10.3847/0004-637X/830/2/154)
- [42] Fortney, J. J., Dawson, R. I., & Komacek, T. D. 2021, *Journal of Geophysical Research (Planets)*, 126, e06629, doi: [10.1029/2020JE006629](https://doi.org/10.1029/2020JE006629)
- [43] Fortney, J. J., Mordasini, C., Nettelmann, N., et al. 2013, *ApJ*, 775, 80, doi: [10.1088/0004-637X/775/1/80](https://doi.org/10.1088/0004-637X/775/1/80)
- [44] France, K. 2016, Measurements of the Ultraviolet Spectral Characteristics of Low-mass Exoplanetary Systems (“MUSCLES”), STScI/MAST, doi: [10.17909/T9DG6F](https://doi.org/10.17909/T9DG6F)
- [45] France, K., Froning, C. S., Linsky, J. L., et al. 2013, *ApJ*, 763, 149, doi: [10.1088/0004-637X/763/2/149](https://doi.org/10.1088/0004-637X/763/2/149)
- [46] France, K., Loyd, R. O. P., Youngblood, A., et al. 2016, *ApJ*, 820, 89, doi: [10.3847/0004-637X/820/2/89](https://doi.org/10.3847/0004-637X/820/2/89)
- [47] France, K., Bean, J. L., Berta-Thompson, Z. K., et al. 2020, MUSCLES Extension for Atmospheric Transmission Spectroscopy: Essential Ultraviolet Stellar Characterization for Guaranteed JWST Transiting Planet Targets, HST Proposal
- [48] Freedman, R. S., Lustig-Yaeger, J., Fortney, J. J., et al. 2014, *ApJS*, 214, 25, doi: [10.1088/0067-0049/214/2/25](https://doi.org/10.1088/0067-0049/214/2/25)
- [49] Freedman, R. S., Marley, M. S., & Lodders, K. 2008, *ApJS*, 174, 504, doi: [10.1086/521793](https://doi.org/10.1086/521793)

- [50] Froning, C. S., Duvvuri, G., France, K., et al. 2019, UV Spectroscopy of LTT1445A: Evaluating the Energetic Irradiance on a Nearby Terrestrial Exoplanet, HST Proposal
- [51] Froning, C. S., Kowalski, A., France, K., et al. 2019, *ApJL*, 871, L26, doi: [10.3847/2041-8213/aaffcd](https://doi.org/10.3847/2041-8213/aaffcd)
- [52] Fulton, B. J., & Petigura, E. A. 2018, *AJ*, 156, 264, doi: [10.3847/1538-3881/aae828](https://doi.org/10.3847/1538-3881/aae828)
- [53] Gaia Collaboration, Brown, A. G. A., Vallenari, A., et al. 2018, *A&A*, 616, A1, doi: [10.1051/0004-6361/201833051](https://doi.org/10.1051/0004-6361/201833051)
- [54] Gao, P., Wakeford, H. R., Moran, S. E., & Parmentier, V. 2021, *Journal of Geophysical Research (Planets)*, 126, e06655, doi: [10.1029/2020JE006655](https://doi.org/10.1029/2020JE006655)
- [55] Gao, P., Thorngren, D. P., Lee, E. K. H., et al. 2020, *Nature Astronomy*, 4, 951, doi: [10.1038/s41550-020-1114-3](https://doi.org/10.1038/s41550-020-1114-3)
- [56] Gao, P., Thorngren, D. P., Lee, G. K. H., et al. 2020, *Nature Astronomy*, 4, 951, doi: [10.1038/s41550-020-1114-3](https://doi.org/10.1038/s41550-020-1114-3)
- [57] Gao, P., Piette, A. A. A., Steinrueck, M. E., et al. 2023, arXiv e-prints, arXiv:2305.05697, doi: [10.48550/arXiv.2305.05697](https://doi.org/10.48550/arXiv.2305.05697)
- [58] Gavilan, L., Broch, L., Carrasco, N., Fleury, B., & Vettier, L. 2017, *ApJL*, 848, L5, doi: [10.3847/2041-8213/aa8cc4](https://doi.org/10.3847/2041-8213/aa8cc4)
- [59] Gavilan, L., Carrasco, N., Vrønning Hoffmann, S., Jones, N. C., & Mason, N. J. 2018, *ApJ*, 861, 110, doi: [10.3847/1538-4357/aac8df](https://doi.org/10.3847/1538-4357/aac8df)
- [60] Gérard, J. C., Dols, V., Grodent, D., et al. 1995, *Geophys. Res. Lett.*, 22, 2685, doi: [10.1029/95GL02645](https://doi.org/10.1029/95GL02645)
- [61] Gibson, N. P., Aigrain, S., Pont, F., et al. 2012, *MNRAS*, 422, 753, doi: [10.1111/j.1365-2966.2012.20655.x](https://doi.org/10.1111/j.1365-2966.2012.20655.x)
- [62] Gladstone, G. R., Stern, S. A., Ennico, K., et al. 2016, *Science*, 351, aad8866, doi: [10.1126/science.aad8866](https://doi.org/10.1126/science.aad8866)
- [63] Gordon, I., Rothman, L., Hill, C., et al. 2017, *JQSRT*, 203, 3, doi: <https://doi.org/10.1016/j.jqsrt.2017.06.038>
- [64] Gordon, I. E., Rothman, L. S., Hill, C., et al. 2017, *JQSRT*, 203, 3, doi: [10.1016/j.jqsrt.2017.06.038](https://doi.org/10.1016/j.jqsrt.2017.06.038)
- [65] Grimm, S. L., & Heng, K. 2015, *ApJ*, 808, 182, doi: [10.1088/0004-637x/808/2/182](https://doi.org/10.1088/0004-637x/808/2/182)
- [66] Grimm, S. L., & Heng, K. 2015, *ApJ*, 808, 182, doi: [10.1088/0004-637x/808/2/182](https://doi.org/10.1088/0004-637x/808/2/182)

- [67] Grimm, S. L., Demory, B.-O., Gillon, M., et al. 2018, *A&A*, 613, A68, doi: [10.1051/0004-6361/201732233](https://doi.org/10.1051/0004-6361/201732233)
- [68] Harman, C. E., Felton, R., Hu, R., et al. 2018, *ApJ*, 866, 56, doi: [10.3847/1538-4357/aadd9b](https://doi.org/10.3847/1538-4357/aadd9b)
- [69] Harman, C. E., Kopparapu, R. K., Stefánsson, G., et al. 2021, arXiv e-prints, arXiv:2109.10838. <https://arxiv.org/abs/2109.10838>
- [70] —. 2022, *Planetary Science Journal*, 3, 45, doi: [10.3847/PSJ/ac38ac](https://doi.org/10.3847/PSJ/ac38ac)
- [71] Harris, C. R., Millman, K. J., van der Walt, S. J., et al. 2020, *Nature*, 585, 357, doi: [10.1038/s41586-020-2649-2](https://doi.org/10.1038/s41586-020-2649-2)
- [72] Hasenkopf, C. A., Beaver, M. R., Trainer, M. G., et al. 2010, *Icarus*, 207, 903, doi: [10.1016/j.icarus.2009.12.015](https://doi.org/10.1016/j.icarus.2009.12.015)
- [73] He, C., Hörst, S. M., Lewis, N. K., et al. 2018, *ApJL*, 856, L3, doi: [10.3847/2041-8213/aab42b](https://doi.org/10.3847/2041-8213/aab42b)
- [74] He, C., Hörst, S. M., Lewis, N. K., et al. 2018, *The Astrophysical Journal*, 856, L3, doi: [10.3847/2041-8213/aab42b](https://doi.org/10.3847/2041-8213/aab42b)
- [75] He, C., Hörst, S. M., Lewis, N. K., et al. 2019, *ACS Earth and Space Chemistry*, 3, 39, doi: [10.1021/acsearthspacechem.8b00133](https://doi.org/10.1021/acsearthspacechem.8b00133)
- [76] He, C., Hörst, S. M., Lewis, N. K., et al. 2020, *The Planetary Science Journal*, 1, 51, doi: [10.3847/psj/abb1a4](https://doi.org/10.3847/psj/abb1a4)
- [77] He, C., Hörst, S. M., Lewis, N. K., et al. 2020, *Planetary Science Journal*, 1, 51, doi: [10.3847/PSJ/abb1a4](https://doi.org/10.3847/PSJ/abb1a4)
- [78] Hébrard, E., Dobrijevic, M., Bénilan, Y., & Raulin, F. 2006, *Journal of Photochemistry and Photobiology C: Photochemistry Reviews*, 7, 211, doi: <https://doi.org/10.1016/j.jphotochemrev.2006.12.004>
- [79] Hirschmann, M. M., Bergin, E. A., Blake, G. A., Ciesla, F. J., & Li, J. 2021, *Proceedings of the National Academy of Science*, 118, e2026779118, doi: [10.1073/pnas.2026779118](https://doi.org/10.1073/pnas.2026779118)
- [80] Hörst, S. M., He, C., Lewis, N. K., et al. 2018, *Nature Astronomy*, 2, 303, doi: [10.1038/s41550-018-0397-0](https://doi.org/10.1038/s41550-018-0397-0)
- [81] Howard, A. W., Marcy, G. W., Bryson, S. T., et al. 2012, *ApJS*, 201, 15, doi: [10.1088/0067-0049/201/2/15](https://doi.org/10.1088/0067-0049/201/2/15)
- [82] Hu, R., Seager, S., & Bains, W. 2012, *ApJ*, 761, 166, doi: [10.1088/0004-637X/761/2/166](https://doi.org/10.1088/0004-637X/761/2/166)
- [83] Hunter, J. D. 2007, *Computing in Science & Engineering*, 9, 90, doi: [10.1109/MCSE.2007.55](https://doi.org/10.1109/MCSE.2007.55)

- [84] Johnstone, C. P., Güdel, M., Stökl, A., et al. 2015, *ApJL*, 815, L12, doi: [10.1088/2041-8205/815/1/L12](https://doi.org/10.1088/2041-8205/815/1/L12)
- [85] Kasting, J., Zahnle, K., Pinto, J., & Young, A. 1989, *Origins of Life and Evolution of Biospheres*, 19, 95, doi: [10.1007/BF01808144](https://doi.org/10.1007/BF01808144)
- [86] Kasting, J. F., & Ackerman, T. P. 1986, *Science*, 234, 1383, doi: [10.1126/science.234.4782.1383](https://doi.org/10.1126/science.234.4782.1383)
- [87] Kasting, J. F., Liu, S. C., & Donahue, T. M. 1979, *J. Geophys. Res.*, 84, 3097, doi: [10.1029/JC084iC06p03097](https://doi.org/10.1029/JC084iC06p03097)
- [88] Kawashima, Y., & Ikoma, M. 2018, *ApJ*, 853, 7, doi: [10.3847/1538-4357/aaa0c5](https://doi.org/10.3847/1538-4357/aaa0c5)
- [89] Kawashima, Y., & Ikoma, M. 2018, *ApJ*, 853, 7, doi: [10.3847/1538-4357/aaa0c5](https://doi.org/10.3847/1538-4357/aaa0c5)
- [90] Kawashima, Y., & Ikoma, M. 2019, *ApJ*, 877, 109, doi: [10.3847/1538-4357/ab1b1d](https://doi.org/10.3847/1538-4357/ab1b1d)
- [91] Keller-Rudek, H., Moortgat, G. K., Sander, R., & Sörensen, R. 2013, *Earth System Science Data*, 5, 365, doi: [10.5194/essd-5-365-2013](https://doi.org/10.5194/essd-5-365-2013)
- [92] Kempton, E. M. R., Lupu, R., Owusu-Asare, A., Slough, P., & Cale, B. 2017, *PASP*, 129, 044402, doi: [10.1088/1538-3873/aa61ef](https://doi.org/10.1088/1538-3873/aa61ef)
- [93] Kempton, E. M. R., Bean, J. L., Louie, D. R., et al. 2018, *PASP*, 130, 114401, doi: [10.1088/1538-3873/aadf6f](https://doi.org/10.1088/1538-3873/aadf6f)
- [94] Kempton, E. M. R., Zhang, M., Bean, J. L., et al. 2023, arXiv e-prints, arXiv:2305.06240, doi: [10.48550/arXiv.2305.06240](https://doi.org/10.48550/arXiv.2305.06240)
- [95] Khare, B. N., Sagan, C., Arakawa, E. T., et al. 1984, *Icarus*, 60, 127, doi: [10.1016/0019-1035\(84\)90142-8](https://doi.org/10.1016/0019-1035(84)90142-8)
- [96] Knutson, H. A., Charbonneau, D., Cowan, N. B., et al. 2009, *ApJ*, 690, 822, doi: [10.1088/0004-637X/690/1/822](https://doi.org/10.1088/0004-637X/690/1/822)
- [97] Kopparapu, R. k., Kasting, J. F., & Zahnle, K. J. 2012, *ApJ*, 745, 77, doi: [10.1088/0004-637X/745/1/77](https://doi.org/10.1088/0004-637X/745/1/77)
- [98] Kopparapu, R. k., Wolf, E. T., Arney, G., et al. 2017, *ApJ*, 845, 5, doi: [10.3847/1538-4357/aa7cf9](https://doi.org/10.3847/1538-4357/aa7cf9)
- [99] Kopparapu, R. K., Ramirez, R., Kasting, J. F., et al. 2013, *ApJ*, 765, 131, doi: [10.1088/0004-637X/765/2/131](https://doi.org/10.1088/0004-637X/765/2/131)
- [100] Kostoglou, M., Konstandopoulos, A., & Friedlander, S. 2006, *Journal of Aerosol Science*, 37, 1102, doi: <https://doi.org/10.1016/j.jaerosci.2005.11.009>
- [101] Krasnopolsky, V. A. 2009, *Icarus*, 201, 226, doi: <https://doi.org/10.1016/j.icarus.2008.12.038>

- [102] Kreidberg, L., Bean, J. L., Désert, J.-M., et al. 2014, *Nature*, 505, 69, doi: [10.1038/nature12888](https://doi.org/10.1038/nature12888)
- [103] Kreidberg, L., Koll, D. D. B., Morley, C., et al. 2019, *Nature*, 573, 87, doi: [10.1038/s41586-019-1497-4](https://doi.org/10.1038/s41586-019-1497-4)
- [104] Lafarga, M., Brogi, M., Gandhi, S., et al. 2023, *MNRAS*, 521, 1233, doi: [10.1093/mnras/stad480](https://doi.org/10.1093/mnras/stad480)
- [105] Larson, E. J., Toon, O. B., West, R. A., & Friedson, A. J. 2015, *Icarus*, 254, 122, doi: <https://doi.org/10.1016/j.icarus.2015.03.010>
- [106] Lavvas, P., & Arfaux, A. 2021, *MNRAS*, 502, 5643, doi: [10.1093/mnras/stab456](https://doi.org/10.1093/mnras/stab456)
- [107] Lavvas, P., Coustenis, A., & Vardavas, I. 2008, *Planetary and Space Science*, 56, 27, doi: <https://doi.org/10.1016/j.pss.2007.05.026>
- [108] Lebonnois, S., & Schubert, G. 2017, *Nature Geoscience*, 10, 473, doi: [10.1038/ngeo2971](https://doi.org/10.1038/ngeo2971)
- [109] Li, J., Bergin, E. A., Blake, G. A., Ciesla, F. J., & Hirschmann, M. M. 2021, *Science Advances*, 7, eabd3632, doi: [10.1126/sciadv.abd3632](https://doi.org/10.1126/sciadv.abd3632)
- [110] Lincowski, A. P., Meadows, V. S., Crisp, D., et al. 2018, *ApJ*, 867, 76, doi: [10.3847/1538-4357/aae36a](https://doi.org/10.3847/1538-4357/aae36a)
- [111] Line, M. R., Liang, M. C., & Yung, Y. L. 2010, *ApJ*, 717, 496, doi: [10.1088/0004-637X/717/1/496](https://doi.org/10.1088/0004-637X/717/1/496)
- [112] Line, M. R., Vasisht, G., Chen, P., Angerhausen, D., & Yung, Y. L. 2011, *ApJ*, 738, 32, doi: [10.1088/0004-637X/738/1/32](https://doi.org/10.1088/0004-637X/738/1/32)
- [113] Loyd, R. O. P., France, K., Youngblood, A., et al. 2016, *ApJ*, 824, 102, doi: [10.3847/0004-637X/824/2/102](https://doi.org/10.3847/0004-637X/824/2/102)
- [114] —. 2018, *ApJ*, 867, 71, doi: [10.3847/1538-4357/aae2bd](https://doi.org/10.3847/1538-4357/aae2bd)
- [115] Loyd, R. O. P., Shkolnik, E. L., Schneider, A. C., et al. 2021, *ApJ*, 907, 91, doi: [10.3847/1538-4357/abd0f0](https://doi.org/10.3847/1538-4357/abd0f0)
- [116] Luger, R., & Barnes, R. 2015, *Astrobiology*, 15, 119, doi: [10.1089/ast.2014.1231](https://doi.org/10.1089/ast.2014.1231)
- [117] Lupu, R. E., Zahnle, K., Marley, M. S., et al. 2014, *ApJ*, 784, 27, doi: [10.1088/0004-637X/784/1/27](https://doi.org/10.1088/0004-637X/784/1/27)
- [118] Mahjoub, A., Carrasco, N., Dahoo, P. R., et al. 2012, *Icarus*, 221, 670, doi: [10.1016/j.icarus.2012.08.015](https://doi.org/10.1016/j.icarus.2012.08.015)
- [119] Maldonado, J., Micela, G., Baratella, M., et al. 2020, *A&A*, 644, A68, doi: [10.1051/0004-6361/202039478](https://doi.org/10.1051/0004-6361/202039478)

- [120] Malik, M., Kempton, E. M.-R., Koll, D. D. B., et al. 2019, *The Astrophysical Journal*, 886, 142, doi: [10.3847/1538-4357/ab4a05](https://doi.org/10.3847/1538-4357/ab4a05)
- [121] Malik, M., Kitzmann, D., Mendonça, J. M., et al. 2019, *The Astronomical Journal*, 157, 170, doi: [10.3847/1538-3881/ab1084](https://doi.org/10.3847/1538-3881/ab1084)
- [122] Malik, M., Grosheintz, L., Mendonça, J. M., et al. 2017, *The Astronomical Journal*, 153, 56, doi: [10.3847/1538-3881/153/2/56](https://doi.org/10.3847/1538-3881/153/2/56)
- [123] Manabe, S., & Wetherald, R. T. 1967, *Journal of Atmospheric Sciences*, 24, 241, doi: [10.1175/1520-0469\(1967\)024<0241:TEOTAW>2.0.CO;2](https://doi.org/10.1175/1520-0469(1967)024<0241:TEOTAW>2.0.CO;2)
- [124] Marfil, E., Taberner, H. M., Montes, D., et al. 2021, *A&A*, 656, A162, doi: [10.1051/0004-6361/202141980](https://doi.org/10.1051/0004-6361/202141980)
- [125] Martioli, E., Hébrard, G., Correia, A. C. M., Laskar, J., & Lecavelier des Etangs, A. 2021, *A&A*, 649, A177, doi: [10.1051/0004-6361/202040235](https://doi.org/10.1051/0004-6361/202040235)
- [126] Matsuo, T., Greene, T. P., Johnson, R. R., et al. 2019, *PASP*, 131, 124502, doi: [10.1088/1538-3873/ab42f1](https://doi.org/10.1088/1538-3873/ab42f1)
- [127] Mauas, P. J. D., Falchi, A., Pasquini, L., & Pallavicini, R. 1997, *A&A*, 326, 249
- [128] Mayor, M., & Queloz, D. 1995, *Nature*, 378, 355, doi: [10.1038/378355a0](https://doi.org/10.1038/378355a0)
- [129] Mazeh, T., Holczer, T., & Faigler, S. 2016, *A&A*, 589, A75, doi: [10.1051/0004-6361/201528065](https://doi.org/10.1051/0004-6361/201528065)
- [130] Mbarek, R., & Kempton, E. M. R. 2016, *ApJ*, 827, 121, doi: [10.3847/0004-637X/827/2/121](https://doi.org/10.3847/0004-637X/827/2/121)
- [131] Meadows, V. S., Arney, G. N., Schwieterman, E. W., et al. 2018, *Astrobiology*, 18, 133, doi: [10.1089/ast.2016.1589](https://doi.org/10.1089/ast.2016.1589)
- [132] Melbourne, K., Youngblood, A., France, K., et al. 2020, *AJ*, 160, 269, doi: [10.3847/1538-3881/abbf5c](https://doi.org/10.3847/1538-3881/abbf5c)
- [133] Miller-Ricci Kempton, E., Zahnle, K., & Fortney, J. J. 2012, *ApJ*, 745, 3, doi: [10.1088/0004-637X/745/1/3](https://doi.org/10.1088/0004-637X/745/1/3)
- [134] Mischna, M. A., Kasting, J. F., Pavlov, A., & Freedman, R. 2000, *Icarus*, 145, 546, doi: [10.1006/icar.2000.6380](https://doi.org/10.1006/icar.2000.6380)
- [135] Mishra, A., & Li, A. 2015, *ApJ*, 809, 120, doi: [10.1088/0004-637X/809/2/120](https://doi.org/10.1088/0004-637X/809/2/120)
- [136] Mollière, P., van Boekel, R., Bouwman, J., et al. 2017, *A&A*, 600, A10, doi: [10.1051/0004-6361/201629800](https://doi.org/10.1051/0004-6361/201629800)
- [137] Moran, S. E., Hörst, S. M., Vuitton, V., et al. 2020, *The Planetary Science Journal*, 1, 17, doi: [10.3847/psj/ab8eae](https://doi.org/10.3847/psj/ab8eae)

- [138] Moran, S. E., Hörst, S. M., Vuitton, V., et al. 2020, *Planetary Science Journal*, 1, 17, doi: [10.3847/PSJ/ab8eae](https://doi.org/10.3847/PSJ/ab8eae)
- [139] Morley, C. V., Fortney, J. J., Marley, M. S., et al. 2015, *ApJ*, 815, 110, doi: [10.1088/0004-637X/815/2/110](https://doi.org/10.1088/0004-637X/815/2/110)
- [140] Moses, J. I., Madhusudhan, N., Visscher, C., & Freedman, R. S. 2013, *ApJ*, 763, 25, doi: [10.1088/0004-637X/763/1/25](https://doi.org/10.1088/0004-637X/763/1/25)
- [141] Moses, J. I., Visscher, C., Fortney, J. J., et al. 2011, *ApJ*, 737, 15, doi: [10.1088/0004-637X/737/1/15](https://doi.org/10.1088/0004-637X/737/1/15)
- [142] Moses, J. I., Line, M. R., Visscher, C., et al. 2013, *ApJ*, 777, 34, doi: [10.1088/0004-637X/777/1/34](https://doi.org/10.1088/0004-637X/777/1/34)
- [143] National Academies of Science, Engineering, and Medicine. 2021, *Pathways to Discovery in Astronomy and Astrophysics for the 2020s* (Washington, DC: The National Academies Press), doi: [10.17226/26141](https://doi.org/10.17226/26141)
- [144] Öberg, K. I., Murray-Clay, R., & Bergin, E. A. 2011, *ApJL*, 743, L16, doi: [10.1088/2041-8205/743/1/L16](https://doi.org/10.1088/2041-8205/743/1/L16)
- [145] pandas development team, T. 2020, pandas-dev/pandas: Pandas, latest, Zenodo, doi: [10.5281/zenodo.3509134](https://doi.org/10.5281/zenodo.3509134)
- [146] Parmentier, V., Showman, A. P., & Lian, Y. 2013, *A&A*, 558, A91, doi: [10.1051/0004-6361/201321132](https://doi.org/10.1051/0004-6361/201321132)
- [147] Parmentier, V., Showman, A. P., & Lian, Y. 2013, *A&A*, 558, A91, doi: [10.1051/0004-6361/201321132](https://doi.org/10.1051/0004-6361/201321132)
- [148] Pavlov, A. A., Brown, L. L., & Kasting, J. F. 2001, *J. Geophys. Res.*, 106, 23267, doi: [10.1029/2000JE001448](https://doi.org/10.1029/2000JE001448)
- [149] Pavlov, A. A., Brown, L. L., & Kasting, J. F. 2001, *Journal of Geophysical Research: Planets*, 106, 23267, doi: [10.1029/2000JE001448](https://doi.org/10.1029/2000JE001448)
- [150] Peacock, S., Barman, T., Shkolnik, E. L., Hauschildt, P. H., & Baron, E. 2019, *ApJ*, 871, 235, doi: [10.3847/1538-4357/aaf891](https://doi.org/10.3847/1538-4357/aaf891)
- [151] Peacock, S., Barman, T., Shkolnik, E. L., et al. 2019, *ApJ*, 886, 77, doi: [10.3847/1538-4357/ab4f6f](https://doi.org/10.3847/1538-4357/ab4f6f)
- [152] —. 2020, *ApJ*, 895, 5, doi: [10.3847/1538-4357/ab893a](https://doi.org/10.3847/1538-4357/ab893a)
- [153] Perrin, M., & Hartmann, J. 1989, *Journal of Quantitative Spectroscopy and Radiative Transfer*, 42, 311, doi: [https://doi.org/10.1016/0022-4073\(89\)90077-0](https://doi.org/https://doi.org/10.1016/0022-4073(89)90077-0)
- [154] Pineda, J. S., Youngblood, A., & France, K. 2021, *ApJ*, 911, 111, doi: [10.3847/1538-4357/abe8d7](https://doi.org/10.3847/1538-4357/abe8d7)

- [155] Plavchan, P., Werner, M. W., Chen, C. H., et al. 2009, *ApJ*, 698, 1068, doi: [10.1088/0004-637X/698/2/1068](https://doi.org/10.1088/0004-637X/698/2/1068)
- [156] Plavchan, P., Barclay, T., Gagné, J., et al. 2020, *Nature*, 582, 497, doi: [10.1038/s41586-020-2400-z](https://doi.org/10.1038/s41586-020-2400-z)
- [157] Pont, F., Knutson, H., Gilliland, R. L., Moutou, C., & Charbonneau, D. 2008, *MNRAS*, 385, 109, doi: [10.1111/j.1365-2966.2008.12852.x](https://doi.org/10.1111/j.1365-2966.2008.12852.x)
- [158] Pruppacher, H. R., & Klett, J. D. 1979, *D. &nbsp;*
- [159] Pryor, W. R., & Hord, C. W. 1991, *Icarus*, 91, 161, doi: [10.1016/0019-1035\(91\)90135-G](https://doi.org/10.1016/0019-1035(91)90135-G)
- [160] Rackham, B. V., Apai, D., & Giampapa, M. S. 2018, *ApJ*, 853, 122, doi: [10.3847/1538-4357/aaa08c](https://doi.org/10.3847/1538-4357/aaa08c)
- [161] Ranjan, S., Schwieterman, E. W., Harman, C., et al. 2020, *ApJ*, 896, 148, doi: [10.3847/1538-4357/ab9363](https://doi.org/10.3847/1538-4357/ab9363)
- [162] Ranjan, S., Wordsworth, R., & Sasselov, D. D. 2017, *ApJ*, 843, 110, doi: [10.3847/1538-4357/aa773e](https://doi.org/10.3847/1538-4357/aa773e)
- [163] Rannou, P., Cabane, M., Botet, R., & Chassefière, E. 1997, *J. Geophys. Res.*, 102, 10997, doi: [10.1029/97JE00719](https://doi.org/10.1029/97JE00719)
- [164] Rannou, P., McKay, C., Botet, R., & Cabane, M. 1999, *Planetary and Space Science*, 47, 385, doi: [https://doi.org/10.1016/S0032-0633\(99\)00007-0](https://doi.org/10.1016/S0032-0633(99)00007-0)
- [165] Rice, W. K. M., Veljanoski, J., & Collier Cameron, A. 2012, *MNRAS*, 425, 2567, doi: [10.1111/j.1365-2966.2012.21728.x](https://doi.org/10.1111/j.1365-2966.2012.21728.x)
- [166] Ricker, G. R., Winn, J. N., Vanderspek, R., et al. 2015, *Journal of Astronomical Telescopes, Instruments, and Systems*, 1, 014003, doi: [10.1117/1.JATIS.1.1.014003](https://doi.org/10.1117/1.JATIS.1.1.014003)
- [167] Rimmer, P. B., & Helling, C. 2016, *ApJS*, 224, 9, doi: [10.3847/0067-0049/224/1/9](https://doi.org/10.3847/0067-0049/224/1/9)
- [168] Rimmer, P. B., Xu, J., Thompson, S. J., et al. 2018, *Science Advances*, 4, eaar3302, doi: [10.1126/sciadv.aar3302](https://doi.org/10.1126/sciadv.aar3302)
- [169] Rosner, D. E., & (Auth.), H. B. 1986, *Transport Processes in Chemically Reacting Flow Systems*, 0th edn. (Butterworths). <http://gen.lib.rus.ec/book/index.php?md5=e366f7c7d85c1028ad36410b408879d7>
- [170] Rugheimer, S., & Kaltenegger, L. 2018, *ApJ*, 854, 19, doi: [10.3847/1538-4357/aaa47a](https://doi.org/10.3847/1538-4357/aaa47a)
- [171] Rutten, R. G. M. 1984, *A&A*, 130, 353

- [172] Schlawin, E., Leisenring, J., Misselt, K., et al. 2020, *AJ*, 160, 231, doi: [10.3847/1538-3881/abb811](https://doi.org/10.3847/1538-3881/abb811)
- [173] Schlawin, E., Leisenring, J., McElwain, M. W., et al. 2021, *AJ*, 161, 115, doi: [10.3847/1538-3881/abd8d4](https://doi.org/10.3847/1538-3881/abd8d4)
- [174] Schwieterman, E. W., Kiang, N. Y., Parenteau, M. N., et al. 2018, *Astrobiology*, 18, 663, doi: [10.1089/ast.2017.1729](https://doi.org/10.1089/ast.2017.1729)
- [175] Segura, A., Kasting, J. F., Meadows, V., et al. 2005, *Astrobiology*, 5, 706, doi: [10.1089/ast.2005.5.706](https://doi.org/10.1089/ast.2005.5.706)
- [176] Segura, A., Walkowicz, L. M., Meadows, V., Kasting, J., & Hawley, S. 2010, *Astrobiology*, 10, 751, doi: [10.1089/ast.2009.0376](https://doi.org/10.1089/ast.2009.0376)
- [177] Seligman, D. Z., Becker, J., Adams, F. C., Feinstein, A. D., & Rogers, L. A. 2022, *ApJL*, 933, L7, doi: [10.3847/2041-8213/ac786e](https://doi.org/10.3847/2041-8213/ac786e)
- [178] Shkolnik, E. L., & Barman, T. S. 2014, *AJ*, 148, 64, doi: [10.1088/0004-6256/148/4/64](https://doi.org/10.1088/0004-6256/148/4/64)
- [179] Sing, D. K., Pont, F., Aigrain, S., et al. 2011, *MNRAS*, 416, 1443, doi: [10.1111/j.1365-2966.2011.19142.x](https://doi.org/10.1111/j.1365-2966.2011.19142.x)
- [180] Sing, D. K., Fortney, J. J., Nikolov, N., et al. 2016, *Nature*, 529, 59, doi: [10.1038/nature16068](https://doi.org/10.1038/nature16068)
- [181] Spyros, P., Nikolov, N. K., Constantinou, S., et al. 2023, *MNRAS*, 521, 2163, doi: [10.1093/mnras/stad637](https://doi.org/10.1093/mnras/stad637)
- [182] Steinrueck, M. E., Koskinen, T., Lavvas, P., et al. 2023, arXiv e-prints, arXiv:2305.09654, doi: [10.48550/arXiv.2305.09654](https://doi.org/10.48550/arXiv.2305.09654)
- [183] Stock, J. W., Kitzmann, D., Patzer, A. B. C., & Sedlmayr, E. 2018, *MNRAS*, 479, 865, doi: [10.1093/mnras/sty1531](https://doi.org/10.1093/mnras/sty1531)
- [184] Swain, M. R., Vasisht, G., & Tinetti, G. 2008, *Nature*, 452, 329, doi: [10.1038/nature06823](https://doi.org/10.1038/nature06823)
- [185] Taylor, J., Radica, M., Welbanks, L., et al. 2023, *MNRAS*, doi: [10.1093/mnras/stad1547](https://doi.org/10.1093/mnras/stad1547)
- [186] Teal, D. J., Kempton, E. M. R., Bastelberger, S., Youngblood, A., & Arney, G. 2022, *ApJ*, 927, 90, doi: [10.3847/1538-4357/ac4d99](https://doi.org/10.3847/1538-4357/ac4d99)
- [187] Tian, F., Kasting, J. F., Liu, H.-L., & Roble, R. G. 2008, *Journal of Geophysical Research (Planets)*, 113, E05008, doi: [10.1029/2007JE002946](https://doi.org/10.1029/2007JE002946)
- [188] Tilipman, D., Vieytes, M., Linsky, J. L., Buccino, A. P., & France, K. 2021, *ApJ*, 909, 61, doi: [10.3847/1538-4357/abd62f](https://doi.org/10.3847/1538-4357/abd62f)

- [189] Tilley, M. A., Segura, A., Meadows, V., Hawley, S., & Davenport, J. 2019, *Astrobiology*, 19, 64, doi: [10.1089/ast.2017.1794](https://doi.org/10.1089/ast.2017.1794)
- [190] Tomasko, M., Doose, L., Engel, S., et al. 2008, *Planetary and Space Science*, 56, 669, doi: <https://doi.org/10.1016/j.pss.2007.11.019>
- [191] Tsai, S.-M., Lyons, J. R., Grosheintz, L., et al. 2017, *ApJS*, 228, 20, doi: [10.3847/1538-4365/228/2/20](https://doi.org/10.3847/1538-4365/228/2/20)
- [192] Tsai, S.-M., Lyons, J. R., Grosheintz, L., et al. 2017, *The Astrophysical Journal Supplement Series*, 228, 20, doi: [10.3847/1538-4365/228/2/20](https://doi.org/10.3847/1538-4365/228/2/20)
- [193] Tsai, S.-M., Malik, M., Kitzmann, D., et al. 2021, *The Astrophysical Journal*, 923, 264, doi: [10.3847/1538-4357/ac29bc](https://doi.org/10.3847/1538-4357/ac29bc)
- [194] Tsai, S.-M., Lee, E. K. H., Powell, D., et al. 2023, *Nature*, 617, 483, doi: [10.1038/s41586-023-05902-2](https://doi.org/10.1038/s41586-023-05902-2)
- [195] Ugelow, M. S., Haan, D. O. D., Hörst, S. M., & Tolbert, M. A. 2018, *ApJL*, 859, L2, doi: [10.3847/2041-8213/aac2c7](https://doi.org/10.3847/2041-8213/aac2c7)
- [196] Vanderspek, R., Huang, C. X., Vanderburg, A., et al. 2019, *ApJL*, 871, L24, doi: [10.3847/2041-8213/aafb7a](https://doi.org/10.3847/2041-8213/aafb7a)
- [197] Venot, O., Bounaceur, R., Dobrijevic, M., et al. 2019, *A&A*, 624, A58, doi: [10.1051/0004-6361/201834861](https://doi.org/10.1051/0004-6361/201834861)
- [198] Venot, O., Hébrard, E., Agúndez, M., et al. 2012, *A&A*, 546, A43, doi: [10.1051/0004-6361/201219310](https://doi.org/10.1051/0004-6361/201219310)
- [199] Venot, O., Rocchetto, M., Carl, S., Roshni Hashim, A., & Decin, L. 2016, *ApJ*, 830, 77, doi: [10.3847/0004-637X/830/2/77](https://doi.org/10.3847/0004-637X/830/2/77)
- [200] Virtanen, P., Gommers, R., Oliphant, T. E., et al. 2020, *Nature Methods*, 17, 261, doi: [10.1038/s41592-019-0686-2](https://doi.org/10.1038/s41592-019-0686-2)
- [201] Volkamer, R., Jimenez, J. L., San Martini, F., et al. 2006, *Geophys. Res. Lett.*, 33, L17811, doi: [10.1029/2006GL026899](https://doi.org/10.1029/2006GL026899)
- [202] Waalkes, W. C., Berta-Thompson, Z., Bourrier, V., et al. 2019, *AJ*, 158, 50, doi: [10.3847/1538-3881/ab24c2](https://doi.org/10.3847/1538-3881/ab24c2)
- [203] Welbanks, L., & Madhusudhan, N. 2022, *ApJ*, 933, 79, doi: [10.3847/1538-4357/ac6df1](https://doi.org/10.3847/1538-4357/ac6df1)
- [204] Wes McKinney. 2010, in *Proceedings of the 9th Python in Science Conference*, ed. Stéfan van der Walt & Jarrod Millman, 56 – 61, doi: [10.25080/Majora-92bf1922-00a](https://doi.org/10.25080/Majora-92bf1922-00a)
- [205] White, R. J., Schaefer, G., Ten Brummelaar, T., et al. 2015, in *American Astronomical Society Meeting Abstracts*, Vol. 225, American Astronomical Society Meeting Abstracts #225, 348.12

- [206] White, W. B., Johnson, S. M., & Dantzig, G. B. 1958, *The Journal of Chemical Physics*, 28, 751
- [207] Wilson, D. J., Froning, C. S., Duvvuri, G. M., et al. 2021, *ApJ*, 911, 18, doi: [10.3847/1538-4357/abe771](https://doi.org/10.3847/1538-4357/abe771)
- [208] Wilson, E., & Atreya, S. 2003, *Planetary and Space Science*, 51, 1017, doi: <https://doi.org/10.1016/j.pss.2003.06.003>
- [209] Wolf, E. T., & Toon, O. B. 2010, *Science*, 328, 1266, doi: [10.1126/science.1183260](https://doi.org/10.1126/science.1183260)
- [210] Wolszczan, A., & Frail, D. A. 1992, *Nature*, 355, 145, doi: [10.1038/355145a0](https://doi.org/10.1038/355145a0)
- [211] Wong, A.-S., Yung, Y. L., & Friedson, A. J. 2003, *Geophys. Res. Lett.*, 30, 1447, doi: [10.1029/2002GL016661](https://doi.org/10.1029/2002GL016661)
- [212] Wunderlich, F., Godolt, M., Grenfell, J. L., et al. 2019, *A&A*, 624, A49, doi: [10.1051/0004-6361/201834504](https://doi.org/10.1051/0004-6361/201834504)
- [213] Xiong, C., & Friedlander, S. K. 2001, *Proceedings of the National Academy of Sciences*, 98, 11851, doi: [10.1073/pnas.211376098](https://doi.org/10.1073/pnas.211376098)
- [214] Youngblood, A., France, K., Loyd, R. O. P., et al. 2016, *ApJ*, 824, 101, doi: [10.3847/0004-637X/824/2/101](https://doi.org/10.3847/0004-637X/824/2/101)
- [215] —. 2017, *ApJ*, 843, 31, doi: [10.3847/1538-4357/aa76dd](https://doi.org/10.3847/1538-4357/aa76dd)
- [216] Zahnle, K., Marley, M. S., Freedman, R. S., Lodders, K., & Fortney, J. J. 2009, *ApJL*, 701, L20, doi: [10.1088/0004-637X/701/1/L20](https://doi.org/10.1088/0004-637X/701/1/L20)
- [217] Zahnle, K., Marley, M. S., Morley, C. V., & Moses, J. I. 2016, *ApJ*, 824, 137, doi: [10.3847/0004-637X/824/2/137](https://doi.org/10.3847/0004-637X/824/2/137)
- [218] Zellem, R. T., Swain, M. R., Roudier, G., et al. 2017, *ApJ*, 844, 27, doi: [10.3847/1538-4357/aa79f5](https://doi.org/10.3847/1538-4357/aa79f5)
- [219] Zerkle, A. L., Yin, R., Chen, C., et al. 2020, *Nature Communications*, 11, 1709, doi: [10.1038/s41467-020-15495-3](https://doi.org/10.1038/s41467-020-15495-3)
- [220] Zhang, X., Liang, M. C., Mills, F. P., Belyaev, D. A., & Yung, Y. L. 2012, *Icarus*, 217, 714, doi: [10.1016/j.icarus.2011.06.016](https://doi.org/10.1016/j.icarus.2011.06.016)